NEUROPATHOLOGY

Improved immunostaining of nanostructures and cells in human brain specimens through expansion-mediated protein decrowding

Pablo A. Valdes[1,2,3], Chih-Chieh (Jay) Yu[3,4,5,6]†, Jenna Aronson[3,5,6]†, Debarati Ghosh[5,7], Yongxin Zhao[3,8], Bobae An[3,5], Joshua D. Bernstock[2,9], Deepak Bhere[2,10,11], Michelle M. Felicella[12], Mariano S. Viapiano[13], Khalid Shah[2,11], E. Antonio Chiocca[2]*‡, Edward S. Boyden[3,4,5,7,9,14,15]*‡

Proteins are densely packed in cells and tissues, where they form complex nanostructures. Expansion microscopy (ExM) variants have been used to separate proteins from each other in preserved biospecimens, improving antibody access to epitopes. Here, we present an ExM variant, decrowding expansion pathology (dExPath), that can expand proteins away from each other in human brain pathology specimens, including formalin-fixed paraffin-embedded (FFPE) clinical specimens. Immunostaining of dExPath-expanded specimens reveals, with nanoscale precision, previously unobserved cellular structures, as well as more continuous patterns of staining. This enhanced molecular staining results in observation of previously invisible disease marker–positive cell populations in human glioma specimens, with potential implications for tumor aggressiveness. dExPath results in improved fluorescence signals even as it eliminates lipofuscin-associated autofluorescence. Thus, this form of expansion-mediated protein decrowding may, through improved epitope access for antibodies, render immunohistochemistry more powerful in clinical science and, perhaps, diagnosis.

INTRODUCTION

Immunohistochemistry uses antibodies to identify accessible epitopes on proteins embedded in intact cells and tissues. Target epitopes in fixed tissues are often physically inaccessible to conventional antibodies (1–12), such as the commonly used class of immunoglobulin G (13, 14).

Expansion microscopy (ExM) enables physical expansion of biological specimens, thereby permitting nanoscale resolution imaging on diffraction-limited microscopes (15, 16). Briefly, ExM starts by covalently anchoring biomolecules, or labels against biomolecules, to a swellable hydrogel densely and evenly synthesized throughout a preserved biological specimen. Then, an enzymatic or protein-denaturing treatment softens the mechanical properties of the specimen. Water then causes the polymer network to expand and thus the anchored molecules to be pulled uniformly away from one another. Given the difficulty of labeling many epitopes in their natural, densely packed state, we asked whether, in human tissues,

conventional antibodies introduced in the post-expansion, decrowded state could access previously undetectable epitopes.

Some expansion protocols preserve protein antigens throughout the expansion process (table S1) (17–25) and are thus compatible with postexpansion immunostaining. However, most of these existing postexpansion staining protocols either require specialized fixative compositions (17, 18, 21, 22, 25) and thus are incompatible with archival clinical samples, cause tissue cracks and anisotropy due to incomplete tissue softening (19), or had uncharacterized nanoscale isotropy (20). In addition, none of these studies underwent quantitative comparison of structures or cells in the same specimen of human tissue with pre- versus postexpansion staining, which is key to understanding whether the decrowding of proteins contributed to visualization of previously invisible structures.

We previously developed expansion pathology (ExPath), a form of ExM that prepares human specimens for ExM, using preexpansion antibody staining (4). Here, we present decrowding ExPath (dExPath), an ExPath variant that preserves protein epitopes for postexpansion staining. dExPath can be applied to formalin-fixed paraffin-embedded (FFPE) human tissues, as well as other standard formats of interest in basic and applied biology, such as 4% paraformaldehyde (PFA)–fixed mouse brain tissue. We validated dExPath systematically, comparing, within the same specimen of human brain tissue, immunostaining intensity and continuity between pre- and postexpansion staining, showing improvements in both intensity and continuity and revealing new features, including disease marker–bearing cell populations (in human glioma specimens) that were previously invisible. Furthermore, dExPath eliminates autofluorescence associated with lipofuscin, an aggregated product commonly found in brain tissue, in addition to autofluorescence reduction resulting from the loss of autofluorescent molecules shown in prior expansion protocols (4). dExPath supports multiround immunostaining, enabling highly multiplexed imaging of protein targets within the same human brain specimen.

[1]Department of Neurosurgery, University of Texas Medical Branch, Galveston, TX 77555, USA. [2]Department of Neurosurgery, Brigham and Women's Hospital, Harvard Medical School, Boston, MA 02115, USA. [3]Media Arts and Sciences, MIT, Cambridge, MA 02115, USA. [4]Department of Biological Engineering, MIT, MA 02139, USA. [5]McGovern Institute for Brain Research, MIT, Cambridge, MA 02139, USA. [6]RIKEN Center for Brain Science, Saitama, 351-0198, Japan. [7]Department of Brain and Cognitive Sciences, MIT, Cambridge, MA 02139, USA. [8]Department of Biological Sciences, Carnegie Mellon University, Pittsburgh, PA 15213, USA. [9]Koch Institute, MIT, Cambridge, MA 02139, USA. [10]Department of Pathology, Microbiology and Immunology, School of Medicine Columbia, University of South Carolina, Columbia, SC 29209, USA. [11]Center for Stem Cell and Translational Immunotherapy, Harvard Medical School/Brigham and Women's Hospital, Boston, MA 02115, USA. [12]Department of Pathology, University of Texas Medical Branch, Galveston, TX 77555, USA. [13]Department of Neuroscience and Physiology, SUNY Upstate Medical University, Syracuse, NY 13210, USA. [14]MIT Center for Neurobiological Engineering and K. Lisa Yang Center for Bionics, MIT, Cambridge, MA 02139, USA. [15]Howard Hughes Medical Institute, Cambridge, MA 02139, USA.
*Corresponding author. Email: eachiocca@bwh.harvard.edu (E.A.C.); edboyden@mit.edu (E.S.B.)
†These authors contributed equally to this work.
‡These authors contributed equally to this work.

RESULTS

Rationale for dExPath technology

We first prepared tissue to enter the expansion pipeline (Fig. 1A; involving tissue deparaffinization and rehydration for FFPE samples) (*4*), followed by protein anchoring and gel formation (Fig. 1B). In contrast to the original ExPath protocol, which uses protease digestion to soften the specimen (feasible because fluorescent antibodies, which are partly protease resistant, are applied preexpansion and anchored to the polymer network for later imaging), we used a buffer to maximally enable protein separation for post-expansion staining. We used higher concentrations of SDS [20% (w/v)] than in earlier protein-preserving protocols (table S1) (*17–23*, *26*), reasoning that this could better denature proteins and minimize noncovalent intra- and interprotein interactions (*27*, *28*). We included a new ingredient, the reducing agent β-mercaptoethanol (100 mM), which we reasoned could cleave intermolecular disulfide bridges between proteins (*24*, *27–31*). We used the same high concentration of EDTA (25 mM) as in original ExPath, which proved to be useful for isotropic tissue

expansion (*4*), possibly through destabilization of metal-mediated protein interactions (*28–30*). We used a higher temperature than in original ExPath, adapted from a form of proExM that uses autoclaving to expose samples to 121°C (Fig. 1C) to strongly denature and loosen bonds between proteins in the sample, allowing them to separate during washes (which drives partial tissue expansion, ~2.3×; Fig. 1D). Antibodies were applied at this post-decrowding state (Fig. 1E; see table S2 for antibodies used in this work) instead of the fully expanded (~4x) state, because full expansion requires sample immersion in water, which can hinder antibody binding (*17–22*). Multiplexing is possible because these antibodies can be stripped using the same buffer, and then new antibodies can be applied (fig. S1), a strategy previously demonstrated by other postexpansion staining protocols but not on human tissues (*18*, *20*, *32*).

High-grade glioma tissues are known to undergo abnormal endothelial proliferation, leading to some areas of tissue with abnormally large amounts of vascularity and extracellular matrix (ECM). These areas can be identified under conventional clinical microscopy
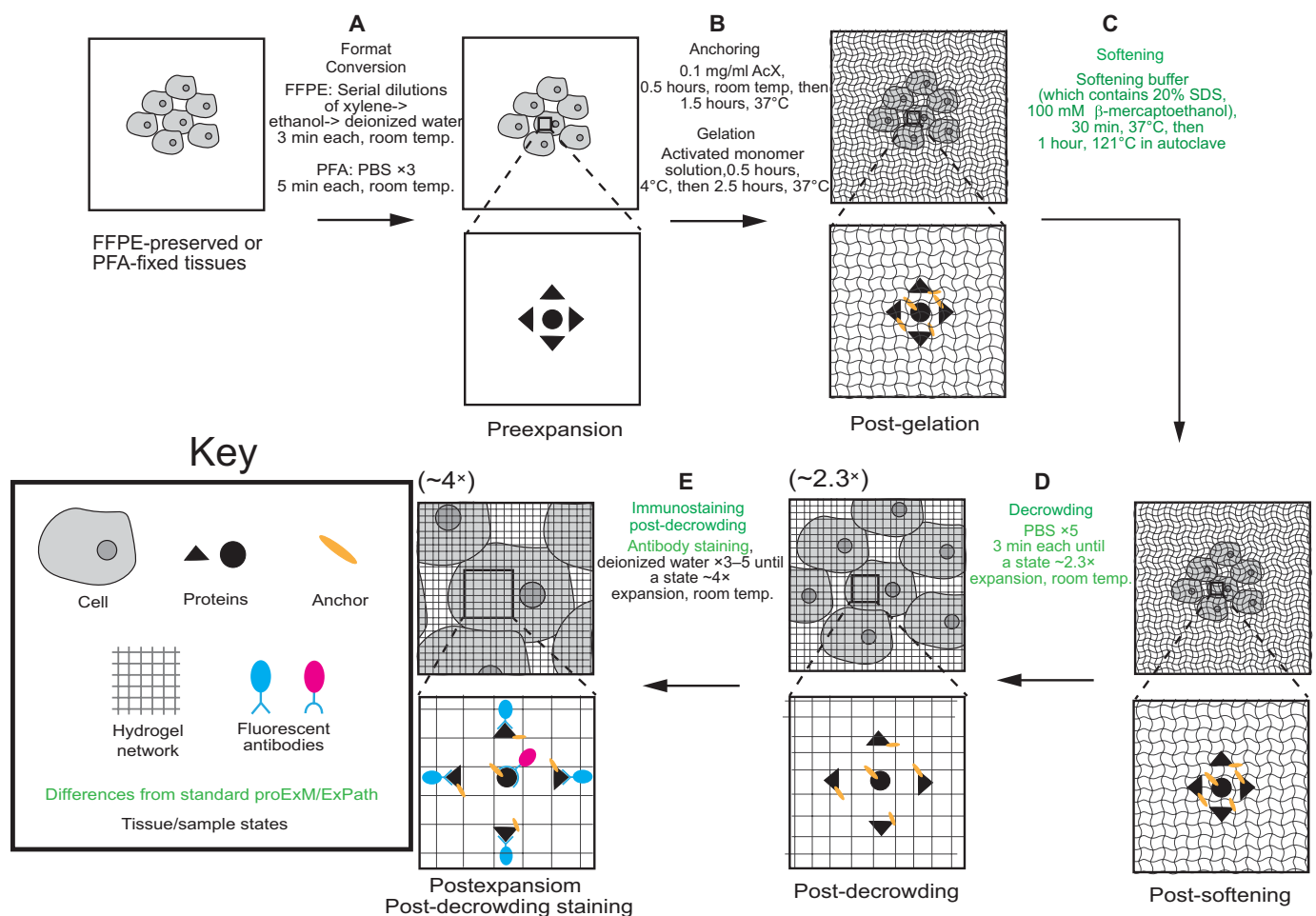
Fig. 1. dExPath for postexpansion immunostaining of human tissue and other formaldehyde-fixed specimens. (**A** to **E**) Workflow for expanding FFPE or formaldehyde-fixed human or mouse brain specimens. Key modifications of proExM/ExPath protocols are highlighted in green. RT, room temperature. (A) Tissue samples undergo conversion into a state compatible with expansion. (B) Tissue samples are treated so that gel-anchorable groups are attached to proteins, and then the sample is permeated with an expandable polyacrylate hydrogel. (C) Samples are incubated in a softening buffer to denature and loosen disulfide bonds and fixation crosslinks between proteins. (D) Softened samples are washed in a buffer to partially expand them. Linear expansion factor is shown in parentheses. (E) Samples are stained and then expanded fully by immersion in water.

(*33*) but present a challenge to isotropic expansion of tissue (*4*). To circumvent this problem, we devised a modified form of dExPath using collagenase treatment before softening (fig. S2). Thus, dExPath was designed to provide a methodology for isotropic tissue expansion, enabling preservation, postexpansion, and multiplexed staining, of decrowded proteins in both normal and pathologic human and rodent brain tissues.

Validation of dExPath expansion isotropy in brain tissue

We validated the isotropy of dExPath on normal and diseased 5-μm-thick FFPE human brain tissues (standard for clinical samples), using the pre- versus postdistortion analysis used to validate earlier expansion protocols (*4*, *15*, *18*, *19*, *34*, *35*). We performed antigen retrieval followed by preexpansion immunostaining against microtubule-associated protein 2 (MAP2; a neuronal dendritic marker) (*36*), and the intermediate filament protein vimentin (*37*–*39*), on normal human hippocampus (Fig. 2A) and on high-grade glioma tissues (located in the human cortex or white matter) (Fig. 2B), respectively. We performed standard immunostaining (*4*, *40*–*42*) and obtained pre-expansion images using a super-resolution structured illumination microscope (SR-SIM) (Fig. 2, A and B). Next, we

performed dExPath (modified to use preexpansion staining before anchoring and gelation, to facilitate distortion comparison between pre- and postexpansion images of the same sample, outlined in fig. S3), obtaining postexpansion images of the same fields of view (Fig. 2, C and D) using a confocal microscope. We observed low distortion between pre- and postexpansion images, similar to previous versions of ExM applied to mouse brain tissue (Fig. 2, E and F) (*4*, *15*, *19*). Our modified form of dExPath using collagenase treatment before softening was used to compare pre- and postexpansion images of the same specimen, as outlined in fig. S4; low distortion was obtained on high-grade glioma tissues with a high degree of ECM (fig. S5). Thus, dExPath isotropically expands archival clinical samples of FFPE normal brain and brain tumor tissues by ~4× without the need for enzymatic epitope destruction (*4*, *19*) or specialized fixatives (*17*, *18*, *21*, *22*).

dExPath removes lipofuscin autofluorescence, improving visualization of intracellular structures

Fluorescence microscopy of clinical tissues is often hindered by lipofuscin (*43*–*50*), an autofluorescent (throughout the visible optical spectrum) material that is composed of aggregates of oxidized
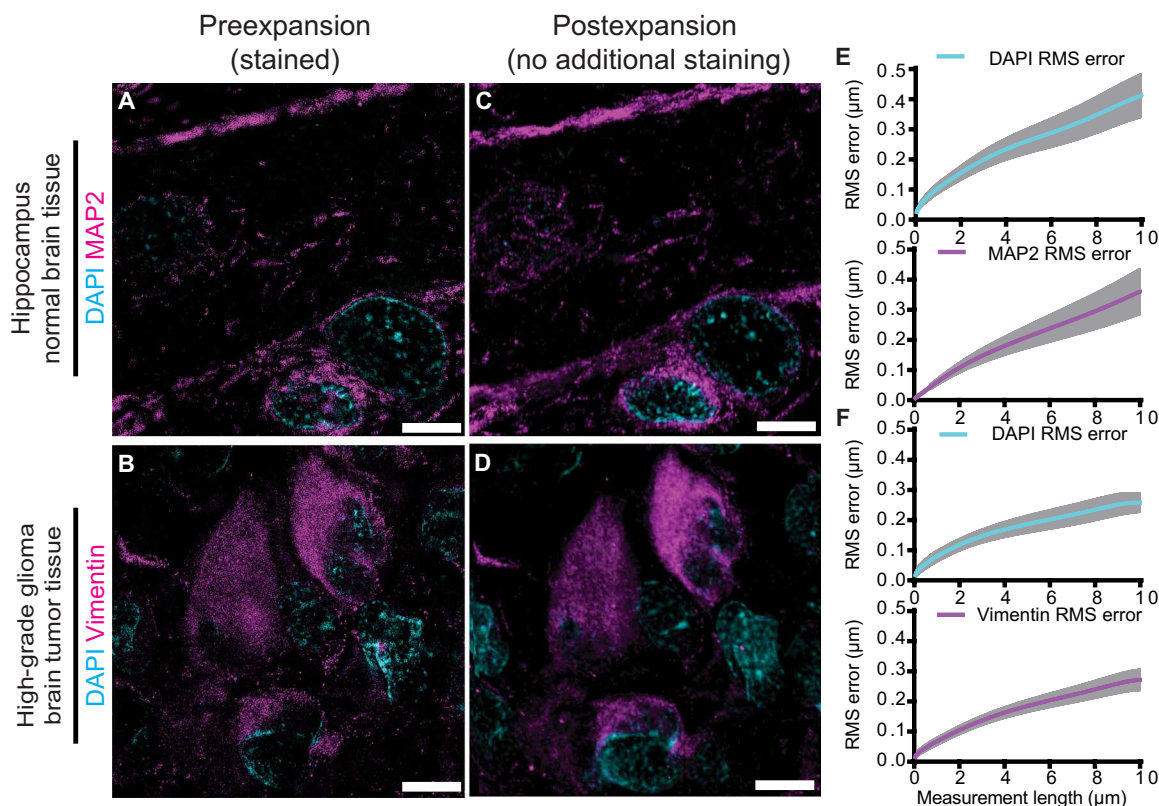
Fig. 2. Isotropy of dExPath. (**A** and **B**) Representative preexpansion super-resolution structured illumination microscopy (SR-SIM) images of healthy human hippocampus (A) and human cerebrum high-grade glioma brain tumor tissue (B) that underwent processing as in fig. S3A with staining for MAP2 and DAPI (A) or for vimentin and DAPI (B). (**C** and **D**) Postexpansion images of the same fields of view as in (A) and (B), respectively. Samples underwent anchoring, gelation, and softening [as in fig. S3 (B and C)]; another round of DAPI staining; ~4× linear expansion (as in fig. S3D); and imaging with confocal microscopy. (**E** and **F**) Root mean square (RMS) length measurement errors obtained by comparing pre- and postexpansion images such as in (A) to (D) (*n* = 4 samples, each from a different patient, E; *n* = 3 samples, each from a different patient, F). Line, mean; shaded area, SD. Images are sum intensity z-projections, either of SR-SIM (A and B) or confocal (C and D) image stacks, both covering an equivalent tissue depth in biological units. Brightness and contrast settings: first set by the ImageJ auto-scaling function and then manually adjusted to improve contrast for the stained structures of interest; quantitative analysis in (E) and (F) was conducted on raw image data. Scale bars (in biological units: physical sizes of expanded samples divided by their expansion factors, used throughout this manuscript, unless otherwise noted), 5 μm (A to D). Linear expansion factors, 4.0× (C and D).

proteins, lipids, and metal cations and that accumulates in many cell and tissue types (*51–54*). We imaged regions with lipofuscin in normal human cortex (ages 19 to 45 years old), in the preexpansion state (Fig. 3, A to D) and in the postexpansion state (Fig. 3, E to H), under three common fluorescent channel settings [488-nm excitation (ex)/525-nm emission (em); 561ex/607em; 640ex/685em], finding that lipofuscin fluorescence was at least an order of magnitude higher than background fluorescence (Fig. 3D; lipofuscin versus background: 488ex/525em, $P = 0.00001$; 561ex/607em, $P = 0.00002$; 640ex/685em, $P = 0.00002$; two-tailed paired t test; all t tests were non-Bonferroni corrected). After dExPath, lipofuscin autofluorescence was reduced to background brightness (Fig. 3H; lipofuscin versus background: 488ex/525em, $P = 0.11$; 561ex/607em, $P = 0.07$; 640ex/685em, $P = 0.29$; two-tailed paired t test). dExPath removed lipofuscin autofluorescence in brain tissue specimens from patients with Alzheimer's disease (AD) (fig. S6). Classical ExPath showed some lipofuscin autofluorescence postexpansion (fig. S7). Using dExPath, structures masked by lipofuscin became detectable. Comparing the same location in the same specimen pre- and postexpansion, with stains against MAP2 (*36*), giantin (a Golgi-apparatus marker) (*55*, *56*), and synaptophysin (a presynaptic marker) (*57*) (Fig. 3, I to K), some giantin staining overlapped with lipofuscin (compare Fig. 3, B versus J; note that images were obtained with the same microscope settings). As another example, human hippocampal tissues that underwent preexpansion immunostaining against MAP2 (488ex/525em) and glial fibrillary acidic protein [GFAP, a marker of astrocytes (*37*, *58*, *59*); 640ex/685em] showed false-positive fluorescence in the GFAP channel in somata of MAP2-positive cells (Fig. 3L). In contrast, post-decrowding, such false-positive GFAP staining, no longer appeared in the somata (Fig. 3M). Thus, dExPath-mediated lipofuscin removal has the potential to improve detection of fluorescent signals in human tissues.

dExPath enables visualization of decrowded proteins revealing previously invisible cells and structures

To investigate whether postexpansion immunostaining could enable detection of previously inaccessible protein epitopes, we compared pre- versus postexpansion staining of normal human hippocampus (Fig. 4, A to F), supratentorial high-grade glioma tumor specimens (Fig. 4, G to R), and low-grade glioma tumor specimens (Fig. 4, S to X). Tissue samples were imaged preexpansion, after antigen retrieval and antibody staining (Fig. 4, A, G, M, and S), after expansion without restaining (Fig. 4, B, H, N, and T), and after expansion and restaining with the same antibodies (Fig. 4, C, I, O, and U; experimental pipeline in fig. S3). All tissue states were imaged using identical confocal imaging settings.

In one experiment (Fig. 4, A to C), we used antibodies against the somato-dendritic marker, MAP2 (*36*, *60*), and the astrocytic marker, GFAP (*37*, *58*, *59*, *61*, *62*). MAP2 staining yielded putative cell bodies and dendrites as well as sparser discontinuous dendrite-like regions (Fig. 4A). The latter regions remained discontinuous after 4× expansion (Fig. 4B). However, after postexpansion restaining, new filaments appeared in areas previously MAP2 negative (Fig. 4C). We found similar improvements for GFAP, with preexpansion staining showing discontinuous signals (Fig. 4A). Postexpansion, resolution improved (Fig. 4B), and after restaining, those regions appeared more continuous and new GFAP fibers became visible (Fig. 4C).

To quantify the improvement in labeling postexpansion versus preexpansion, we constructed a binary image "signal" mask, for

each stain, that corresponded to pixels that were positive (above a manually selected threshold) for a given stain in both preexpansion and postexpansion staining images. We also created a second "background" mask, for each stain, that corresponded to pixels that were negative (below the threshold mentioned before) in both pre- and postexpansion staining images; a "double-negative" background mask corresponded to the pixels that were negative in both of these background masks. Next, we constructed regions of interest (ROIs) that were small enough (0.2 μm) to fit entirely within the signal mask for a given stain but that were at least an ROI-width away from the signal mask for the other stain; we also constructed ROIs that were fully contained within the double-negative mask and similarly far from pixels that were positive in either signal mask. Last, we calculated intensities averaged across the ROIs for the same locations in the expanded (Fig. 4B) versus expanded-and-restained (Fig. 4C) images. In regions positive in the MAP2 and GFAP signal masks [Fig. 4, D (left) and E (right)], we saw increases of both signals in their respective ROIs (MAP2, $P = 0.0003$, two-tailed paired t test; $n = 3$ tissue samples from different patients; GFAP, $P = 0.0007$, two-tailed paired t test; $n = 3$ tissue samples from different patients). Of course, we would not expect MAP2 to occur in GFAP-positive regions nor GFAP in MAP2 regions. Thus, these two proteins give us the opportunity to assess whether postexpansion antibody application suffers from nonspecific staining. GFAP was consistently low in both preexpansion and postexpansion images ($P = 0.0004$, two-tailed paired t test; $n = 3$ tissue samples from different patients) in locations within the MAP2 signal mask. Similarly, MAP2, imaged in the GFAP signal mask, was consistently low in pre- and postexpansion images ($P = 0.003$, two-tailed paired t test).

In the double-negative regions, MAP2 intensities were consistently low in pre-decrowding and post-decrowding states (Fig. 4F, left), as were GFAP intensities (Fig. 4F, right). Thus, staining in the double-negative regions was similar to that in the single-negative regions, supporting the idea that the nonspecific staining is extremely low.

We performed a similar analysis in high-grade glioma tissue from a human patient (Fig. 4, G to I), staining for GFAP, which, in glioma patients, marks both astrocytes and glioma cells (*58*, *63–65*) and α–smooth muscle actin (α-SMA), a marker of pericytes (*66–68*), which envelope blood vessels (Fig. 4G). As with MAP2 versus GFAP, α-SMA and GFAP would not be expected to overlap, except perhaps at sites where astrocytes and glioma cells touch pericytes (*68*, *69*); accordingly, we chose GFAP-positive and α-SMA–positive ROIs that were far apart from α-SMA and GFAP staining, respectively, as well as double-negative ROIs that exhibited neither. As before, GFAP became more continuous with postexpansion staining (Fig. 4, G to I), showing new filaments and an overall increase in intensity in GFAP-positive ROIs (Fig. 4J, left; $P = 0.0006$, two-tailed paired t test; $n = 3$ tissue samples from different patients). α-SMA intensity also went up in α-SMA–positive regions (Fig. 4K, right; $P = 0.0006$ two-tailed paired t test; $n = 3$ tissue samples from different patients). In contrast, α-SMA was consistently low in pre- and postexpansion states, in GFAP-positive ROIs (Fig. 4J, right; $P = 0.004$, two-tailed paired t test; $n = 3$ tissue samples from different patients); GFAP was consistently low in pre- and postexpansion states, in α-SMA–positive ROIs ($P = 0.004$; two-tailed paired t test; $n = 3$ tissue samples from different patients). Also, GFAP and α-SMA values in the double-negative ROIs were comparably low (Fig. 4L).

Next, we examined vimentin and α-SMA in high-grade glioma tissue. Vimentin is expressed in some tumor cells (*70*), some
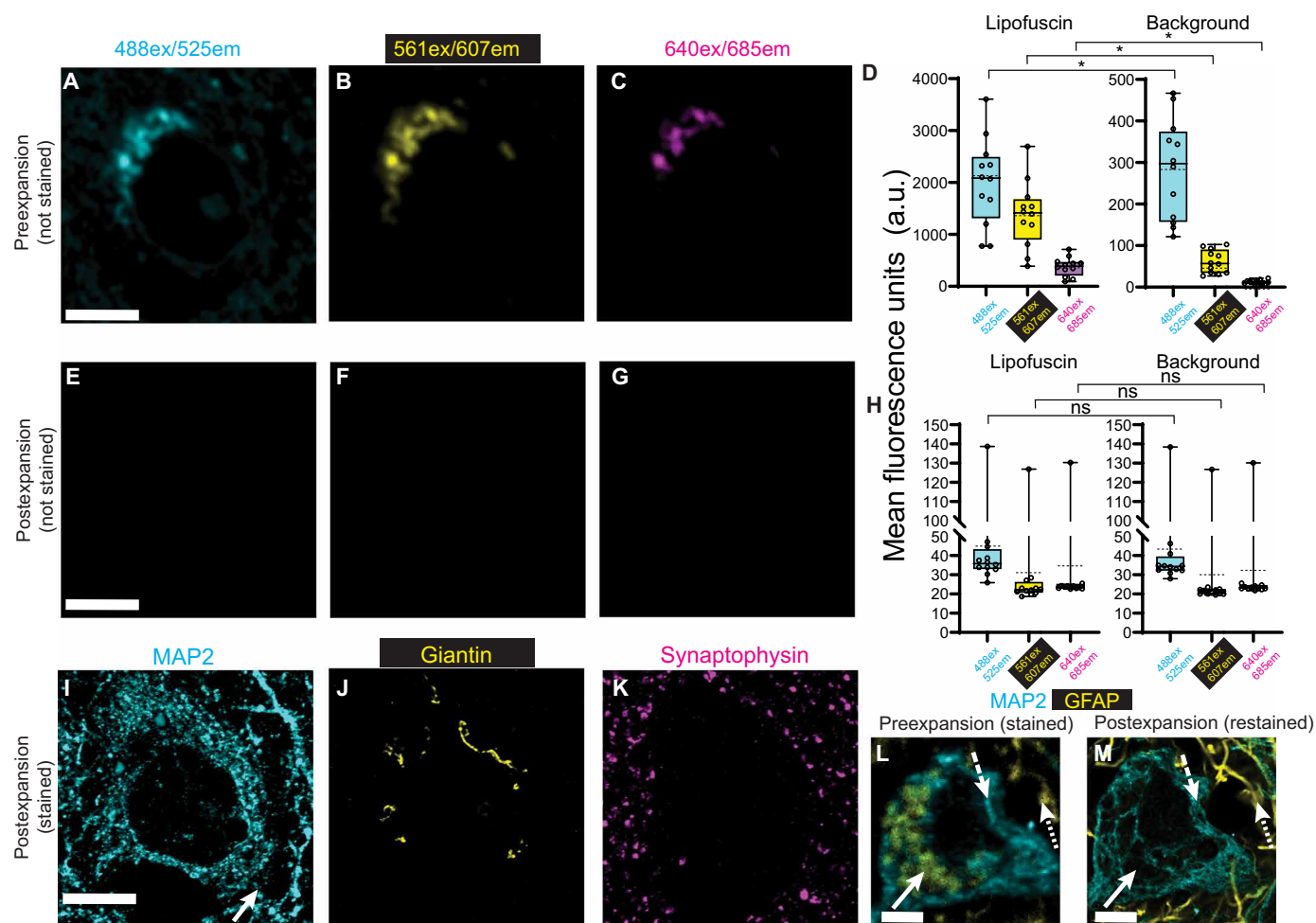
Fig. 3. dExPath removal of lipofuscin autofluorescence. (**A** to **C**) Preexpansion confocal images (single *z* slices) of a neuron in a 5-μm-thick normal human cortex sample (format conversion as in Fig. 1A). Images were acquired for three fluorescent channel settings: (A) 488ex/ 525em; (B) 561ex/607em; and (C) 640ex/685em. (**D**) Mean fluorescence intensities from preexpansion images, averaged across ROIs that exhibited prominent lipofuscin (left bar graph), as well as across background ROIs (right bar graph); (*n* = 4 tissue samples, each from a different patient). Brightness and contrast settings: first set by the ImageJ autoscaling function and then manually adjusted to improve contrast for lipofuscin; quantitative analysis was conducted on raw image data. Box plot: individual values (open circles; three measurements were acquired from each patient), median (middle line), mean (dotted line), first and third quartiles (lower and upper box boundaries), lower and upper raw values (whiskers). Statistical testing: two-tailed paired *t* test (non-Bonferroni corrected) was applied to lipofuscin versus background for preexpansion mean fluorescence intensities for each spectral channel. *$P < 0.05$; ns, not significant. (**E** to **G**) Shown are postexpansion confocal images after the sample from (A) to (C) was treated with anchoring, gelation, softening, and decrowding [as in Fig. 1 (B to D)]; DAPI staining; and ~4× linear expansion, without post-decrowding immunostaining. Sum intensity z-projections of image stacks corresponding to the biological thickness of the original slice, taken under identical settings and of the same field of view as (A) to (C) and displayed under the same settings. (**H**) Mean fluorescence intensities, from postexpansion images, averaged across the same lipofuscin (left) and background (right) ROIs used in (D). Plots and statistics as in (D). (**I** to **K**) Confocal images as in (E) to (G), after post-decrowding immunostaining for MAP2 (microtubule-associated protein 2), giantin, and synaptophysin (labeled with antibodies in the same spectral ranges as indicated above (A to C), as well as stained for DAPI (not shown; used for alignment), and then reexpanded to ~4× linear expansion. (**L**) Representative preexpansion confocal image of a tissue sample of 5-μm-thick FFPE normal human hippocampus processed as in fig S3A. Preexpansion immunostaining for MAP2 (488ex/525em) and GFAP (glial fibrillary acidic protein) (640ex/685em). Solid arrow indicates a region with lipofuscin aggregates (GFAP-like staining but found in a neuron); dashed arrow indicates MAP2 staining without lipofuscin; dotted arrow indicates GFAP staining. (**M**) Confocal image of the same field of view as (L). Tissues underwent softening and ~4× expansion, followed by decrowding, post-decrowding staining for MAP2 and GFAP, and expansion to ~4× [as in fig. S3 (B to F)]. Arrows, as in (L). Scale bars (in biological units), 7 μm (A, E, and I) and 5 μm (L and M). Linear expansion factors, 4.3× (E to G and I to K) and 4.1× (M). a.u., arbitrary units.

activated microglia (*71*), all endothelial cells (*38*), and some pericytes (*72*). Thus, vimentin would be expected to sometimes be near, or even overlapping, with α-SMA (in pericytes) and sometimes to be well-isolated from α-SMA (in other cell types) (*68, 69, 73*). We observed vimentin and α-SMA signals in the blood vessel wall and surrounding the vessel lumen (Fig. 4M). Vimentin signals were also observed in cells (putative tumor cells or activated microglia)

outside of blood vessels (Fig. 4M); with similar observations after 4× expansion (Fig. 4N). However, after postexpansion restaining (Fig. 4O), new vimentin positivity appeared in cells, far from blood vessels, that were previously vimentin negative (Fig. 4, M to O). We analyzed vimentin ROIs far away from α-SMA and found the vimentin staining to go up in these ROIs (Fig. 4P, left; $P = 0.0008$, two-tailed paired *t* test; *n* = 3 tissue samples from different patients); in
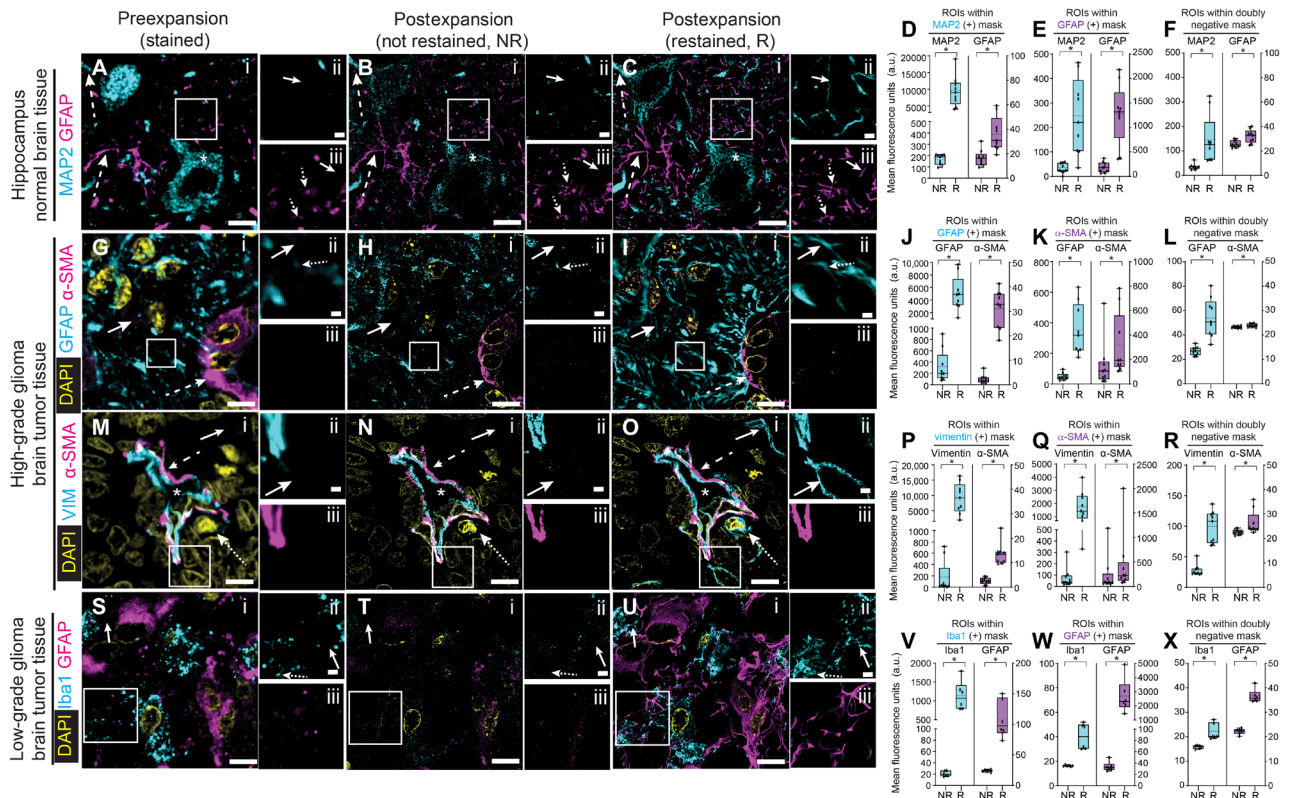
Fig. 4. dExPath-mediated protein decrowding reveals cells and structure not detected in preexpansion staining forms of expansion microscopy. (**A**) Representative preexpansion confocal image (single *z* slice) of 5-μm-thick FFPE normal human hippocampal tissue. (Sample underwent processing as in fig. S3A and immunostaining for MAP2 and GFAP.) White box in (i) marks a region with sparse and discontinuous signals that is shown magnified and in separate channels at the right [MAP2 in (ii) and GFAP in (iii)]. MAP2 staining of a putative cell body [asterisk in (i)] and dendrite [upper dashed arrow in (i)]. GFAP staining of a putative astrocytic process [lower dashed arrow in (i)] and discontinuous GFAP regions [dotted arrows in (iii)]. Solid arrows show regions that were MAP2 negative (ii) or GFAP negative (iii) in preexpansion images (A) for comparison to postexpansion staining panels later in this figure. (**B**) Shown is a postexpansion confocal image after processing as in fig. S3 (B to D) and imaging at ~4× linear expansion. Sum intensity z-projection of an image stack covering the biological thickness of the original slice (used for all expanded images throughout this figure); images were of the same fields of view as in (A), using identical hardware settings. Asterisks and arrows as in (A). (**C**) Post-decrowding stained confocal images of the same fields of view as in (A) and (B) after decrowding and additional immunostaining for MAP2 and GFAP and reexpansion to ~4× (fig. S3, E and F), using identical hardware settings. Asterisks and arrows as in (A). (**D**) Quantification of fluorescence intensities for raw data of images postexpansion such as those of (B) (NR, "not restained") and (C) (R, "restained"), averaged across MAP2-positive ROIs, for the MAP2 channel (cyan) and the GFAP channel (magenta). Box plot: individual values (open circles; three measurements were acquired from each patient), median (middle line), mean (dotted line), first and third quartiles (lower and upper box boundaries), and lower and upper raw values (whiskers). Statistical testing: two-tailed paired *t* test (non-Bonferroni corrected) *$P < 0.05$. (**E**) As in (D), but for GFAP-positive ROIs, for the MAP2 channel (cyan) and the GFAP channel (magenta). (**F**) As in (D), but for double-negative ROIs, for the MAP2 channel (cyan) and the GFAP channel (magenta). (**G**) Representative preexpansion confocal image (single *z* slice) of 5-μm-thick FFPE human high-grade glioma. Sample underwent format conversion, antigen retrieval, and immunostaining for GFAP and α-SMA and DAPI staining (fig. S3A). White box in (i) marks a region with sparse and discontinuous signals that is shown magnified and in separate channels at the right [GFAP in (ii) and α-SMA in (iii)]. α-SMA staining of pericytes that are enveloping blood vessels [dashed arrow in (i)]. Discontinuous GFAP regions [dotted arrow in (ii)]. Solid arrows in (i) and (ii) show regions that were GFAP-negative preexpansion (G), for comparisons to postexpansion staining panels later in this figure. (**H**) As in (B), but for (G). (**I**) As in (C), but for (G). (**J**) As in (D), but for the GFAP (cyan) and α-SMA (magenta) channels, in GFAP-positive ROIs. (**K**) As in (D), but for the GFAP (cyan) and α-SMA (magenta) channels in α-SMA–positive ROIs. (**L**) As in (D), but for the GFAP (cyan) and α-SMA (magenta) channels in double-negative ROIs. (**M**) Representative (preexpansion confocal image (single *z* slice) of 5-μm-thick human high-grade glioma tissue (cortex or white matter). Sample underwent format conversion, antigen retrieval, and immunostaining for vimentin and α-SMA and DAPI staining (fig. S3A). White box in (i) marks a region including part of a blood vessel that is shown magnified and in separate channels to the right [vimentin in (ii) and α-SMA in (iii)]. Vimentin and α-SMA staining of the blood vessel wall [dashed arrow in (i)] that surrounds the vessel lumen [asterisk in (i)]. A vimentin-positive cell outside the blood vessel [dotted arrow in (i)]. Solid arrows in (i) and (ii) show regions that were vimentin-negative preexpansion (M) for comparison to postexpansion staining panels later in this figure. (**N**) As in (B), but for (M). (**O**) As in (C), but for (M). (**P**) As in (D), but for the vimentin channel (cyan) and the α-SMA channel (magenta), in vimentin-positive ROIs. (**Q**) As in (D), but for the vimentin channel (cyan) and the α-SMA channel (magenta), in α-SMA–positive ROIs. (**R**) As in (D), but for the vimentin channel (cyan) and the α-SMA channel (magenta), in double-negative ROIs. (**S**) Representative preexpansion confocal image (single *z* slice) of 5-μm-thick human low-grade glioma tissue (cortex or white matter). Sample underwent format conversion, antigen retrieval, and immunostaining for ionized calcium binding adapter molecule 1 (Iba1) and GFAP and DAPI staining (fig. S3A). White box in (i) marks a region with sparse and discontinuous signals that is shown magnified and in separate channels to the right [Iba1 in (ii) and GFAP in (iii)]. Iba1 staining of discontinuous regions [dotted arrow in (ii)]. Solid arrows in (i) and (ii) show regions that were Iba1-negative preexpansion (S) for comparison to postexpansion staining panels later in this figure. (**T**) As in (B), but for (S). (**U**) As in (C), but for (S). (**V**) As in (D), but for the Iba1 channel (cyan) and the GFAP channel (magenta), in the Iba1-positive ROIs. (**W**) As in (D), but for the Iba1 channel (cyan) and the GFAP channel (magenta), in GFAP-positive ROIs. (**X**) As in (D), but for the Iba1 channel (cyan) and the GFAP channel (magenta), in the double-negative ROIs. Scale bars, 9 μm (i) and 1.7 μm (ii) (A to C), 7 μm (i) and 0.7 μm (ii) (G to I), 8 μm (i) and 0.8 μm (ii) (M to O), and 8 μm (i) and 0.8 μm (ii) (S to U). Linear expansion factors, 4.1× (B and C), 4.0× (H and I), 4.3× (N and O), and 4.2× (T and U).

α-SMA ROIs, vimentin also went up significantly (Fig. 4Q, left; $P = 0.0001$, two-tailed paired t test; $n = 3$ tissue samples from different patients), as expected. In contrast, α-SMA was located very little in the vimentin ROIs (Fig. 4P, right; $P = 0.0001$, two-tailed paired t test; $n = 3$ tissue samples from different patients) and went up in α-SMA ROIs (Fig. 4Q, right; $P = 0.04$, two-tailed paired t test; $n = 3$ tissue samples from different patients) to some extent; not all proteins are equally crowded in all cells; perhaps α-SMA is relatively uncrowded to begin with. As before, double-negative staining was consistently low (Fig. 4R).

Last, we examined ionized calcium binding adapter molecule 1 (Iba1) and GFAP in low-grade glioma tissue, again from cortex or white matter. Iba1 is expressed in macrophages and microglia (74). The places we would expect colocalization of these two markers are at sites where an Iba1-positive cell (macrophage and microglia) (74) and a GFAP-positive cell (astrocyte and glioma) touch (75), where microglia have phagocytosed GFAP-containing fragments (75), or possibly where there is a cell type with a dual astrocytic and macrophage/microglia molecular phenotype (76–79). Accordingly, we chose ROIs that were Iba1 positive or GFAP positive that were far apart from GFAP and Iba1 staining, respectively, as well as double-negative ROIs that exhibited neither. We observed GFAP and Iba1 signals in distinct cells before (Fig. 4S) and after expansion (Fig. 4T). However, after postexpansion restaining (Fig. 4U), new Iba1 positivity appeared in regions that were previously Iba1 negative (Fig. 4, S to U) and appeared more continuous (Fig. 4, S to U). Iba1 increased in intensity in Iba1-positive ROIs (Fig. 4V, left; $P = 0.0009$, two-tailed paired t test; $n = 3$ tissue samples from different patients). GFAP also went up in GFAP-positive regions (Fig. 4W, right; $P = 0.003$ two-tailed paired t test; $n = 3$ tissue samples from different patients). In contrast, GFAP was consistently low in pre- and postexpansion states in Iba1-positive ROIs (Fig. 4V, right; $P = 0.0009$, two-tailed paired t test; $n = 3$ tissue samples from different patients); Iba1 was consistently low, pre- and postexpansion, in GFAP-positive ROIs (Fig. 4W, left; $P = 0.002$; two-tailed paired t test; $n = 3$ tissue samples from different patients). In addition, as before, the Iba1 and GFAP values in the double-negative ROIs were comparably low (Fig. 4X).

Having validated the decrowding aspect of dExPath, we next examined whether the improved immunostaining facilitated by dExPath improved images in comparison with those obtained by a similar-resolution super-resolution method that does not decrowd epitopes, SR-SIM. We first performed antigen retrieval and stained high-grade glioma and normal hippocampus with anti-vimentin or anti-MAP/anti-GFAP. Samples were imaged by SR-SIM (Fig. 5, A and B), followed by the first part of the dExPath protocol (chemical softening and expansion) (fig. S3, A to D) to acquire confocal images postexpansion with pre-decrowding staining (Fig. 5, C and D). Next, we performed the last part of the dExPath protocol to acquire confocal images postexpansion with post-decrowding staining (Fig. 5, E and F, and fig. S3, E and F). Both SR-SIM and postexpansion confocal images of pre-decrowding–stained tissue revealed punctate patterns for vimentin (Fig. 5, A and C), MAP2, and GFAP (Fig. 5, B and D). In contrast, these stains revealed continuous structures after post-decrowding staining (Fig. 5, E and F), as well as structures that had not been observed previously (compare Fig. 5, A, C, and E versus B, D, and F). Thus, dExPath may provide a general solution to the problem of punctate staining appearance in brain tissues, for continuous signals, in super-resolution microscopy (7, 9, 11, 14, 80).

dExPath retains proteins with improved visualization of targets in normal, glioma, AD, and PD human brains

We next investigated whether post-decrowding immunostaining improved visualization of protein targets using validated, commercial antibodies useful for pathological analysis. We observed improved visualization compared with standard histopathological chromogenic analysis in immediately adjacent tissue sections of normal human cortex, AD human cortex, and Parkinson's disease (PD) human cortex (fig. S8). For chromogenic analysis, tissues were imaged preexpansion, after antigen retrieval, with primary antibody staining followed by biotinylated secondary antibody staining and use of 3,3′-diaminobenzidine (DAB). For dExPath, immediately adjacent tissue sections underwent post-decrowding staining with the same primary antibodies and fluorescent secondaries under the same conditions (experimental pipeline in fig. S1). dExPath images yielded expected biological targets such as putative neurons (via anti-MAP2 antibody), neurofilaments [via anti–neurofilament light chain (NF-L)], AD plaques (via anti–amyloid-β), and PD aggregates (via anti–α-synuclein) but demonstrated better resolution, especially for densely packed filamentous structures such as MAP2 and NF-L, and more structural detail with amyloid plaques and α-synuclein aggregates versus standard DAB analysis.

Next, we examined AD brain tissue preexpansion (Fig. 6) and found that amyloid-β plaque autofluorescence (imaged with the fluorescence channel 488ex/525em) was more than one order of magnitude greater than background (Fig. 6A; amyloid-β plaque versus background: 488ex/525em, $P = 0.002$; two-tailed paired t test; $n = 3$ tissue samples, each from a different patient). After dExPath, amyloid-β plaque autofluorescence decreased to background (Fig. 6B; amyloid-β plaque versus background: 488ex/525em, $P = 0.07$; two-tailed paired t test; $n = 3$ tissue samples, each from a different patient; images were obtained with the same microscope settings).

Both methoxy-x04 and aβ(1–42) antibody staining overlapped with preexpansion amyloid-β plaque autofluorescence (compare Fig. 6, A versus C). We performed additional post-decrowding costaining for amyloid-β, phospho-tau, and GFAP (Fig. 6D). In this image, plaques with ~20- to 30-μm diameters were visualized by aβ(1–42) antibody, and they were associated with smaller structures consistent with putative neurofibrillary tangles (81–84) that were positively stained by phospho-tau antibody and surrounded by GFAP-bearing structures, consistent with astrocytes (85).

We surveyed a panel of antibodies commonly used by clinical pathology labs and found that dExPath could produce high-quality images, enabling detection of protein targets across glioma, normal, AD, and PD human tissues (fig. S9). We also observed that dExPath does not lead to protein loss (fig. S10). We demonstrated that dExPath enables multiple rounds of staining and imaging on the same tissue sample, allowing multiplexed imaging with nanoscale resolution of human brain tissues (figs. S11 and S12). dExPath worked well on mouse brain tissue fixed with standard PFA (fig. S13). dExPath could be applied to tissue sections thicker than used in standard pathology preparations (50 to 100 μm) (fig. S14 and movies S1 and S2).

dExPath reveals cell populations exhibiting combinations of disease-state markers in human glioma tissue

Our prior experiments using glioma tissues (Figs. 4 and 5) demonstrated that postexpansion staining increases the intensity, continuity, and number of structures stained for vimentin, Iba1, and GFAP
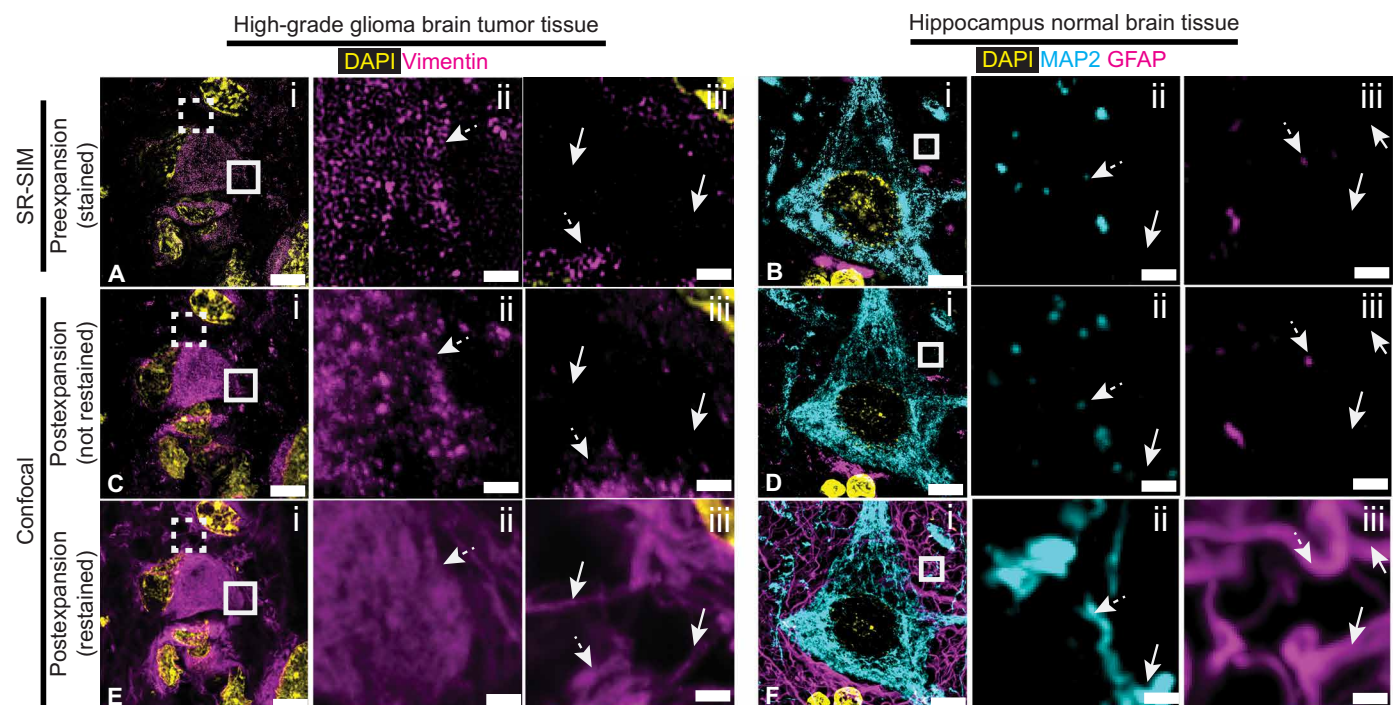
Fig. 5. dExPath-mediated protein decrowding reveals cells and structures not detected by SR-SIM imaging of unexpanded tissues. (**A** and **B**) Representative preexpansion SR-SIM images of 5-μm-thick FFPE human tissue (processed as in fig. S3A). (A) High-grade glioma tissue stained for vimentin and DAPI. Solid and dashed white boxes in (i) mark two separate regions shown magnified in (ii) (solid box) and (iii) (dashed box), respectively. Dotted arrows mark regions that appear as punctate and discontinuous in preexpansion SR-SIM images for vimentin in (ii) and (iii), and solid arrows mark regions that were negative for vimentin in (iii), for comparison to postexpansion staining panels later in this figure. (B) Normal human hippocampus tissue stained for MAP2, GFAP, and DAPI. (A) Solid white box in (i) shown magnified in (ii) for MAP2 and in (iii) for GFAP. Arrows as in (A) but for MAP2 and GFAP, in their respective images. (**C** and **D**) Shown are representative samples used for (A) and (B) after processing for postexpansion imaging (fig. S3, B to D) and not restained. Sum intensity z-projection of an image stack covering the biological thickness of the original slice (used for all expanded images throughout this figure); images were of the same fields of view as in (A) and (B). Arrows as in (A) and (B). (**E** and **F**) Images of the same fields of view as in (A) and (B) after decrowding and additional restaining for vimentin (E) or MAP2 and GFAP (F), followed by DAPI staining and reexpansion to ~4× (fig. S3, E and F), imaged using identical hardware settings as in (C) and (D). Arrows as in (A) and (B). Brightness and contrast settings in images (A to F): first set by the ImageJ autoscaling function and then manually adjusted to improve contrast for stained structures. Scale bars (in biological units), 8.3 μm (left column) and 840 nm (middle and right columns) (A, C, and E) and 6.0 μm (left column) and 500 nm (middle and right columns) (B, D, and F). Linear expansion factors, 4.1× (C), 4.3× (D), 4.1× (E), and 4.2× (F).
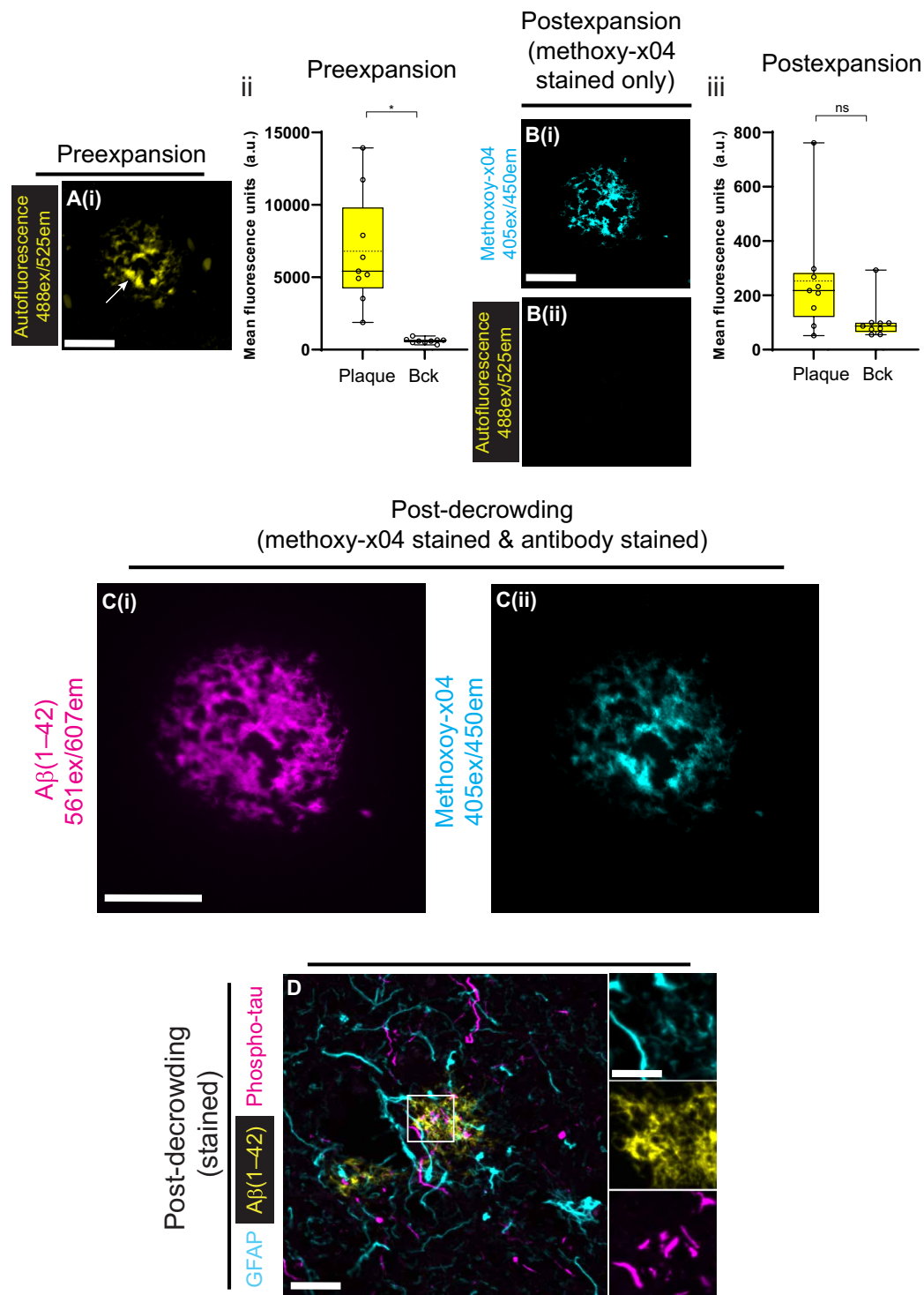
versus preexpansion staining. We next asked whether this could lead to detecting more cells carrying specific antigen combinations, which might alter interpretation of clinical biopsies as well as basic understanding of brain tumor biology. For example, cells with both GFAP and vimentin have been reported to be more aggressive than vimentin-negative/GFAP-positive tumor cells (*86–89*).

For identification of cells, one may want the enhanced staining afforded by postexpansion staining, without incurring the time cost of imaging an expanded specimen. Thus, we compared the initial pre-decrowded immunostained state with the post-decrowded immunostained state after tissues were shrunk back down to almost their native size (~1.3×) by adding salt. We imaged low-grade glioma tissue sections serially (i) after antigen retrieval and pre-decrowding immunostaining (Fig. 7A); (ii) after dExPath softening, washing with phosphate-buffered saline (PBS) (which results in an expansion factor of ~2.3×) and tissue shrinkage (via adding salt to attain expansion factor of 1.3×; Fig. 7B); (iii) after ~4× expansion (~4×; Fig. 7C); (iv) after post-decrowding immunostaining, washing (~2.3×) and shrinkage (~1.3×) (Fig. 7D); and (v) after a final expansion step back to ~4× (Fig. 7E). In this way, we could decouple the effects of improved resolution from those of improved staining in the same specimen.
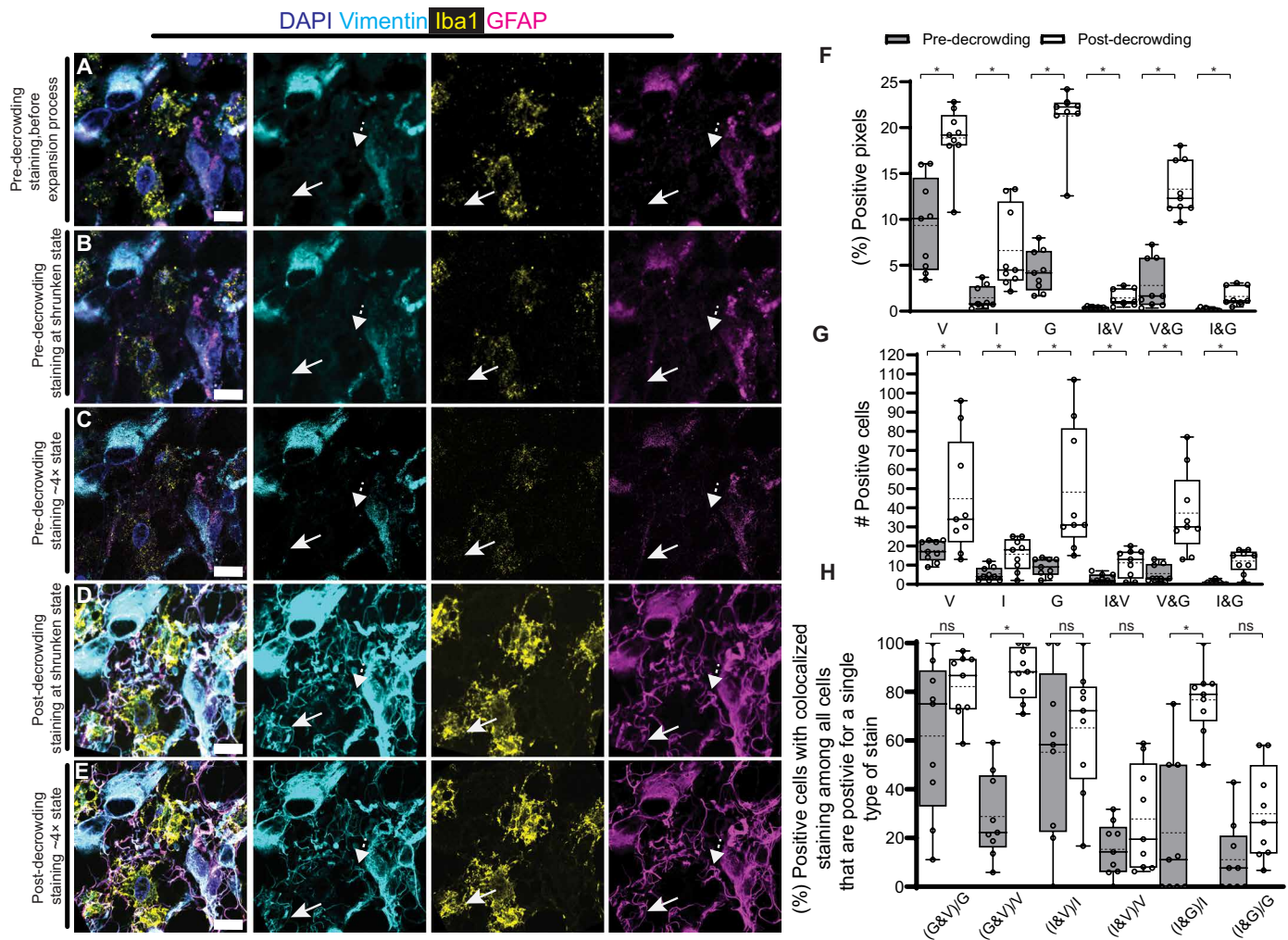
By comparing samples at pre-decrowding versus post-decrowding staining stages, both in the shrunken ~1.3× state (Fig. 7, A, B, and D), we observed that post-decrowding immunostaining (Fig. 7D) was able to reveal additional vimentin-, GFAP-, and Iba1-positive staining not detected in the preexpansion (Fig. 7A) or pre-decrowding staining (Fig. 7B) states, despite the lack of physical magnification in all three cases. Some regions showed increased signal after post-decrowding immunostaining. For example, some regions showed new structures that were GFAP and vimentin positive (compare Fig. 7, D and E versus A to C), or Iba1, GFAP, and vimentin positive (compare Fig. 7, D and E versus A to C). When we examined the fraction of pixels that were positive for one or more stains in single z-slices of preexpansion (Fig. 7A) and post-decrowding (Fig. 7D) images, they increased significantly (Fig. 7F; $P < 0.05$).

These increases in stain-positive pixels translated into increases in the number of cells identified with a label (Fig. 7G; vimentin, $P = 0.032$, two-tailed paired t test, $n = 3$ tissue samples from different patients; GFAP, $P = 0.0071$, two-tailed paired t test, $n = 3$ tissue samples from different patients; Iba1, $P = 0.0011$, two-tailed paired t test, $n = 3$ tissue samples from different patients). Thus, the number of cells corresponding to some tumor cells, some activated microglia, as well as all endothelial cells, and some pericytes of mesenchymal

Valdes *et al.*, *Sci. Transl. Med.* **16**, eabo0049 (2024)   31 January 2024

8 of 17

Fig. 6. dExPath removes autofluorescence from amyloid plaques and preserves detection of disease markers in AD. (**A**) Representative preexpansion confocal image (single z slice) of an amyloid-β plaque within a 5-μm-thick FFPE sample of AD human cortex. The samples underwent processing as in Fig. 1A. (i) Images were acquired for the fluorescent channel setting of 488ex/525em. Solid arrow points to an amyloid-β plaque. (ii) Mean fluorescence intensities from preexpansion images, averaged across ROIs taken at an amyloid-β plaque (plaque, left bar) and background ROIs (Bck, right bar); brightness and contrast settings were first set by the ImageJ autoscaling function and then manually adjusted to improve contrast for the amyloid-β plaque; quantitative analysis in (ii) was conducted on raw image data. Box plot: individual values (open circles; three plaque measurements were acquired from each patient), median (middle line), mean (dotted line), first and third quartiles (lower and upper box boundaries), and lower and upper raw values (whiskers). Statistical testing: Two-tailed paired t test was applied to amyloid-β plaque versus background for preexpansion mean fluorescence intensities. *$P < 0.05$. (**B**) Postexpansion confocal images after the sample from (A) was processed as in Fig. 1 (B to D), post-decrowding methoxy-x04 stained, and ~4× linear expansion. Images were acquired for two common fluorescent channel settings: (i) a 405ex/450em channel to detect methoxy-x04 and (ii) a 488ex/525em channel to detect plaque autofluorescence as in (A). Sum intensity z-projections of image stacks corresponding to the biological thickness of the original slice, taken under identical settings and of the same field of view as in (A) and displayed under the same settings. (iii) Mean fluorescence intensities, from postexpansion images, averaged across the same amyloid-β plaque (left bar) and background (right bar) ROIs used in (A). Plots and statistics as in (A). (**C**) Images of the same field of view as in (A) and (B), but the sample was additionally immunostained post-decrowding (as in Fig. 1E), with a (i) Aβ(1–42) (amyloid-β protein) monoclonal antibody, and images were acquired for the channel settings 561ex/607em channel and (ii) methoxy-x04 using the same spectral ranges as indicated in (B) at ~2.2× linear expansion; brightness and contrast settings adjusted as in (A) to improve contrast for stained structures. (**D**) Confocal image of a 5-μm-thick FFPE sample of AD human cortex. Sample was processed as in Fig. 1 (A to D), post-decrowding immunostained, and imaged at ~2.3× linear expansion (Fig. 1E). The tissue sample was stained for Aβ(1–42) (an amyloid-β plaque marker) and phospho-tau (a neurofibrillary tangle marker), and GFAP (an astrocyte marker). White box marks regions shown magnified in insets on the right. All images are sum intensity z-projections of a confocal image stack. Brightness and contrast settings determined as in (C). Scale bars (in biological units), 25 μm (A to C). Linear expansion factors, 4.1× (B) and 2.2× (C). Scale bars (in physical units), 25 μm (D, left) and 10 μm (inset). Linear expansion factor, 2.3× (D).

Valdes *et al.*, *Sci. Transl. Med.* **16**, eabo0049 (2024)   31 January 2024

9 of 17

Fig. 7. dExPath reveals previously undetected cells defined by single and multiple markers of importance to glioma biology. (**A**) Representative preexpansion confocal image (single *z* slice) of a 5-μm-thick FFPE human low-grade glioma specimen. Sample was immunostained for vimentin, Iba1 and GFAP, and DAPI staining (fig. S3A). Left: Overlay of all four channels. Right three: Individual channels (not including DAPI). Dotted arrows show regions that were vimentin and GFAP negative in preexpansion images, and solid arrows show regions that were Iba1, GFAP, and vimentin negative in preexpansion images, for comparison to post-decrowding staining panels later in this figure. (**B**) Sample used for (A) after anchoring, gelation, and softening (fig. S3, B and C); washing with PBS (which results in an expansion factor of ~2.3×); tissue shrinkage (via adding salt) to ~1.3× of the original size; and imaging. Single *z* slice image centered at the same midpoint of the original slice; images were of the same field of view as in (A) using identical hardware and software settings. Arrows as in (A). (**C**) Sample used for (B) after expansion (fig. S3D) for imaging at ~4× linear expansion. Sum intensity z-projection of an image stack covering the biological thickness of the original slice; images were of the same field of view as in (A) using identical hardware and software settings. Arrows as in (A). (**D**) Post-decrowding stained confocal images of the same field of view as in (A) after decrowding and additional immunostaining for vimentin, Iba1, and GFAP; tissue shrinkage (fig. S3, E and F); and imaging at shrunken state. Arrows as in (A). (**E**) Sample used for (D) after expansion (fig. S3D) for imaging at ~4× linear expansion. Arrows as in (A). (**F**) Pixel level analysis of the percent of single- or double-positive stained pixels, from preexpansion (gray boxes) and post-decrowding at shrunken state (white boxes) images, for vimentin (V), Iba1 (I), GFAP (G), Iba1 and vimentin (I&V), vimentin and GFAP (V&G), and Iba1 and GFAP (I&G). Values represent the percentage of positive pixels among all pixels in the field of view with three different values per sample each corresponding to a different field of view. Box plot: individual values (open circles; three measurements were acquired from each patient), median (middle line), mean (dotted line), first and third quartiles (lower and upper box boundaries), and lower and upper raw values (whiskers), used throughout the graphs of this figure. (**G**) Cell-level analysis of single- or double-positive labeled cells from preexpansion and post-decrowding at shrunken state images. Values represent the total number of labeled cells in the field of view. (**H**) Cell-level analysis of the percentage of double-positive labeled cells divided by all single-positive cells for a stain in the preexpansion and post-decrowding at shrunken state images. Values represent the percentage (%) of double-positive cells relative to the total number of single-positive cells for a stain. Brightness and contrast settings in images (A to E): first set by the ImageJ auto-scaling function and then manually adjusted (by raising the minimum intensity threshold and lowering the maximum intensity threshold) to improve contrast for stained structures, but quantitative analysis in (F) to (H) was conducted on raw image data. Statistical testing: Two-tailed paired *t* test (non-Bonferroni corrected) was applied on preexpansion and post-decrowding values. *$P < 0.05$. Scale bars, 11 μm (A to E). Linear expansion factors, 1.3× (B and D) and 4.4× (C and E).

origin (vimentin), astrocytes and glioma cells (GFAP), or macrophages and microglia (Iba1) increased markedly, suggesting that many cell types important for glioma pathology and response may be quantitatively underestimated by conventional immunostaining.

We next examined the counts of cell types defined by multiple labels. As mentioned earlier, a cell with both GFAP and vimentin is an aggressive tumor cell (86–90), a cell with Iba1 and vimentin is an activated macrophage or microglial cell (71, 74, 91), and a cell with Iba1 and GFAP is either a macrophage or microglial cell that phagocytosed a GFAP-expressing cell (astrocyte or tumor cell) or a cell type with a dual astrocytic and macrophage/microglia molecular phenotype (75–77, 79, 92). In each case, the double-labeled cell is qualitatively different from a singly labeled one. Cells positive both for GFAP and vimentin, identified as aggressive/invasive tumor cells, increased in number by about sixfold with postexpansion versus preexpansion staining, suggesting that more aggressive/invasive tumor cells are present than previously thought (Fig. 7G, $P = 0.0035$, two-tailed paired t test, $n = 3$ tissue samples from different patients). Among GFAP-expressing cells, we observed a ~30% increase in the fraction that were vimentin positive (Fig. 7H, $P = 0.036$, two-tailed paired t test, $n = 3$ tissue samples from different patients), suggesting that even in low-grade gliomas, a vast majority of tumor cells may be aggressive. Cells double-labeled with Iba1 and vimentin increased by about fourfold using post-decrowding versus pre-decrowding staining (Fig. 7G, $P = 0.0030$, two-tailed paired t test, $n = 3$ tissue samples from different patients), suggesting that a majority of activated macrophages and microglia might now be overlooked.

Similarly, cells double-labeled with Iba1 and GFAP increased by about 10-fold with post-decrowding versus pre-decrowding staining (Fig. 7G, $P = 0.00043$, two-tailed paired t test, $n = 3$ tissue samples from different patients). These double-labeled cells are indicative of two cell populations. One population is that of macrophages or microglia, which have phagocytosed GFAP-expressing cells or debris in the tumor tissue sample from astrocytes or tumor cells (75–77, 79, 92). Macrophage or microglial phagocytosis of GFAP-expressing cells and their debris may support tumor growth via removing of debris such as apoptotic corpses from the tumor microenvironment (75). The second cell population might be a cell population found in diseased states such as stroke and neurodegenerative states (76, 77, 92) and recently found to be present in glioblastoma (79), in which cells share the molecular signatures of both Iba1-expressing cells (macrophages or microglia) and GFAP-expressing cells (astrocytes or tumor cells) (75, 79). We show a substantial increase of these Iba1-GFAP dually labeled cells, which can have a protumorigenic role in low-grade gliomas (75, 79). Approximately 80% of Iba1-expressing cells also exhibited GFAP postexpansion versus only 20% preexpansion ($P = 0.000094$, two-tailed paired t test, $n = 3$ tissue samples from different patients; Fig. 7H). In summary, we observed an increase in the percentage of immune cells with phenotypes of importance for the growth of low-grade gliomas.

DISCUSSION

We describe here a form of ExM, dExPath, that enables immunostaining of decrowded proteins for nanoscale visualization of previously unseen biological structures and cell populations in human clinical tissue specimens. By isotropic magnification of human tissues together with antigen preservation, we achieved protein decrowding, improving the accessibility of target epitopes by antibodies (1–3, 7–10, 93). dExPath works across both normal and diseased brain tissue (low- and high-grade gliomas) types, improving immunostaining for many molecular targets. dExPath enables immunostaining of previously inaccessible cells or subcellular features in normal brain and tumor tissues. Postexpansion staining not only improved the continuity of staining for known structures but also revealed previously invisible structures of appropriate morphology, as has been noted before in mouse brain tissue (26) but now shown for human brain tissue. It also increased cell counts, including cell types involved with tumor aggression and immune response. These results suggest that post-decrowding staining could, potentially, uncover cell populations that may contribute to early tumor progression but remain undetected with common histological methods. Further studies correlating the presence of these cell populations with clinical outcomes will be necessary to quantify and apply increased clinico-pathological accuracy.

Although the clinical applications of these findings need to be explored further, in the context of patient outcomes, treatment regimens, and other relevant factors beyond the scope of this technology paper, to be relevant for any potential future diagnostic or prognostic use, our results show potential for dExPath as a research tool for clinicians and researchers to uncover immunostaining patterns previously unseen in diseased tissues, with further potential, when validated in clinical contexts, for improved diagnostics.

Post-decrowding staining may increase the number of spatially accessible epitopes on a target protein, increasing labeling density of the antibodies and their associated fluorescent signals. Previous studies demonstrated improvement in immunostaining by using small-sized probes (~3 nm) (1, 2, 7, 11, 12, 80). dExPath supports the use of conventional off-the-shelf antibodies and can therefore be applied immediately in research settings.

dExPath removed the autofluorescence from lipofuscin found in senescent brain tissues (43–50), improving immunohistochemistry-mediated detection of intracellular structures. Although other methods exist for the masking or quenching of lipofuscin autofluorescence, such as with Sudan Black B (51), they have been associated with limitations, including interruption of antibody binding and reduction of on-target fluorescence (44, 46, 49, 50).

dExPath provides for highly multiplexed immunostaining of decrowded proteins by retaining protein antigenicity across sequential rounds of antibody stripping and restaining. These capabilities could be useful for mapping cellular and molecular types and states in normal and diseased tissue microenvironments.

This study examined several antigen targets that have been commonly used as molecular markers to identify specific cell types or states important in normal or diseased brains. For example, dExPath revealed abundant, clearly resolved GFAP-positive filaments in nondiseased human brain tissue, via its decrowding capability. GFAP is involved in physiological and injury-induced functions in which the precise role of this protein remains unknown, but its spatial localization appears critical for function [for example, formation of glial scars (94, 95), maintenance of myelinated sites (96), lining of the blood-brain barrier (97), etc.]. Visualizing GFAP-positive filaments will facilitate studies of cellular responses to brain injury in clinically relevant human contexts.

Our triple staining experiment (vimentin, Iba1, and GFAP) of low-grade glioma tissues showed that dExPath can reveal substantially increased colocalization between these cell type markers, with

implications for the analysis of cell populations in glioma biology. For example, our detection of an increased number of previously undetected double-labeled GFAP- and vimentin-positive cells in low-grade glioma tissue may represent a malignant cell subpopulation in these tumors (*98–102*), usually not detected histologically. Similarly, cells double-labeled with Iba1 and vimentin [interpreted as activated macrophages or microglial cells (*71, 74, 91*)] may represent a smoldering status of immune activation that could have clinical relevance in these tumors, and cells double-labeled with Iba1 and GFAP may represent an increase in the number of phagocytic macrophages/microglia or possibly an increase in tumor cells with phagocytic properties with increased invasive ability (*74, 78, 79, 103–105*). Although we have primarily focused on glioma tissues for this study, dExPath could be applied to other malignancies and/or neuropathologies (AD and PD).

Our study has limitations. Here, we optimized dExPath for normal and pathologic brain tissues. However, its application in other tissue types may require additional optimization; for example, a preliminary application of standard dExPath to lymph node tissue did not yield the same low distortion seen for the brain (fig. S15), suggesting that additional softening would be useful for tissues more fibrous than the soft brain; lymph node studies are beyond the scope of our clinical expertise. dExPath uses low-cost, commercially available reagents and instruments (confocal microscopes) found in a conventional basic science laboratory. However, confocal microscopes and some of the reagents, all of which are commercially available, are not standard in clinical laboratories, which might limit the immediate use of dExPath in a standard clinical setting.

dExPath requires multiple manual steps that could benefit from automation to become more efficient for routine use. dExPath may be amenable for automation, given the low amount of tissue deformation present (Fig. 2); the excellent protein preservation evidenced (Figs. 4 to 7 and figs. S9 and S13), even after multiple rounds of immunostaining and stripping (figs. S11 and S12); and the previously published compatibility of gel-embedded tissues for automated multiple rounds of staining and imaging in an RNA context (*106*). Image analysis would benefit from software that supports accurate quantification and automated registration, now not part of routine clinical laboratory workflows. Lightsheet microscopy could accelerate imaging of expanded samples (*35, 107*) but again is not routinely used in the clinic. Studies demonstrating the clinical benefit of dExPath in prognosis or personalized medicine would be required for ultimate clinical adoption. All of these limitations represent urgent opportunities for our field.

In conclusion, dExPath achieves protein decrowding and highly multiplexed immunostaining of archival clinical samples while enabling nanoscale resolution imaging on conventional microscopes, all accomplished using low-cost, commercially available reagents and instruments found in conventional basic science or pathology laboratories. We anticipate broad utility of dExPath in many scientific and clinical contexts to advance our understanding of molecular relationships in pathological states and improve diagnostic capabilities.

MATERIALS AND METHODS
Study design
The aim of this study was to optimize and characterize dExPath for use in normal and pathologic human brain tissues. The goal of this technology is to preserve protein epitopes for post-decrowding

staining using commercially available antibodies while expanding tissues isotropically so that nanoscale resolution can be achieved on conventional microscopes. We characterized the ability of dExPath to eliminate tissue autofluorescence associated with lipofuscin and other molecular phenomena (amyloid-β plaques). We characterized the ability of dExPath to support multiround postexpansion immunostaining. For this, we used human tissue microarrays with specific numbers of samples and experimental replicates as indicated in the figures and main text. No blinding, randomization, or prior power calculations were performed.

Statistical analysis
For sample sizes $n < 20$, individual-level data in tabular format can be found in table S3. Two-tailed paired Student's *t* test was used when comparing two groups. Statistically significant results were marked with asterisks in figures, with specific *P* values noted in the text. Statistical analyses were performed using GraphPad Prism software.

Human and animal samples
The normal brain, low- and high-grade glioma human samples used in this study were all 5-μm-thick FFPE tissue microarrays obtained from US Biomax or GeneTex. The use of excess deidentified archival specimens does not require informed consent from the donors.

All procedures involving animals were conducted in accordance with the US National Institutes of Health Guide for the Care and Use of Laboratory Animals and approved by the Massachusetts Institute of Technology Committee on Animal Care. Male and female 12- to 16-week-old, wild-type (Swiss Webster) mice were used in this study. Mice were anesthetized with isoflurane and perfused transcardially with ice-cold PBS followed by ice-cold 4% PFA in PBS. Brains were harvested and postfixed in the same fixative solution at 4°C overnight. Fixed brains were incubated in 100 mM glycine for 1 to 2 hours at 4°C and sectioned to 10- or 100-μm-thick slices.

Tissue processing methods
Format conversion, antigen retrieval, preexpansion NHS ester staining, and preexpansion immunostaining
For 5-μm-thick FFPE samples of normal human hippocampus or cortex, human low- or high-grade glioma brain tumor tissues and human AD or PD cortex format conversion (Fig. 1A and fig. S1A) entail deparaffinization and rehydration, which includes two washes in 100% xylene for 3 min each and then serial incubation in the following solutions, for 3 min each at room temperature (RT): (i) 50% xylene + 50% ethanol, (ii) 100% ethanol, (iii) 95% ethanol (in deionized water, as for all the following ethanol dilution solutions), (iv) 80% ethanol, (v) 50% ethanol, (vi) deionized water, and (vii) 1× PBS. For 4% PFA 10-μm-thick samples of normal mouse brains, format conversion entails three washes in 1× PBS at RT for 5 min each.

After format conversion, tissue samples were designated for (i) preexpansion immunostaining (figs. S3A and S4A); (ii) no preexpansion immunostaining and only preexpansion 4′,6-diamidino-2-phenylindole (DAPI) staining at 2 μg/ml in 1× PBS at RT for 15 min (Fig. 1A); or (iii) directly to the next steps in our protocol (Fig. 1, B to E, and fig. S2, B to F) without any pre-expansion staining.

For tissue samples that were designated for preexpansion immunostaining, after format conversion we applied antigen retrieval to enhance immunostaining (*4, 41, 42*). Antigen retrieval was performed by incubating tissues in either the softening buffer [20% (w/v) SDS, 100 mM β-mercaptoethanol, 25 mM EDTA, and 0.5%

Valdes *et al.*, *Sci. Transl. Med.* **16**, eabo0049 (2024)   31 January 2024

12 of 17

Triton X-100 in 50 mM tris at pH 8 at RT for 1 hour; Fig. 1A] or by microwave heating for 1 min in 5 mM citric acid buffer, 0.5% Triton X-100 (pH 6), because it provided improved collagen staining (fig. S4A). Antigen retrieval was then followed by three washes in 1× PBS for 5 min each and blocking at 37°C for 30 min with MAXblock blocking buffer (Active Motif, #15252) (4). Immunostaining was performed by diluting primary antibody in MAXbind Staining buffer (Active Motif, #15253) and incubating tissue samples in the antibody solution at 37°C for 1 hour, at RT for 2.5 hours, or at 4°C overnight. The same procedure conditions were applied for secondary antibodies. Primary and secondary antibodies used in this work are listed in table S2. All preexpansion stained tissues were immersed in VECTASHIELD mounting media (Vector Laboratories, #H-1000-10) and covered with a no. 1 coverslip before imaging.

Anchoring and gelation

Anchoring and gelation were performed according to previously published protocols (4, 19) and briefly summarized below. Acryloyl-X [also known as 6-((acryloyl)amino)hexanoic acid, succinimidyl ester, here abbreviated AcX; Thermo Fisher Scientific, #A20770] powder was dissolved in anhydrous dimethyl sulfoxide at a concentration of 10 mg/ml and stored in aliquots in a desiccated environment at −20°C. Tissues underwent anchoring by incubation with AcX at a concentration of 0.1 mg/ml in 1× PBS with 0.5% Triton X-100, at 4°C for 30 min, followed by 1.5 hours at 37°C, and then three washes with 1× PBS at RT for 5 min each. Next, a monomer solution composed of 1× PBS, 2 M sodium chloride (NaCl), 8.625% (w/v) sodium acrylate, 2.5% (w/v) acrylamide, and 0.10% (w/v) N,N'-methylenebisacrylamide (Sigma-Aldrich) was prepared, aliquoted, and stored at −20°C. Gelling solution was prepared by mixing the monomer solution with the following chemicals, in the order shown: (i) 4-hydroxy-2,2,6,6-tetramethylpiperidin-1-oxyl [abbreviated as 4-HT; final concentration, 0.01% (w/v)] as an inhibitor of gelation, (ii) tetramethylethylenediamine [abbreviated as TEMED; final concentration, 0.2% (w/v)] as an accelerator of gelation, and (iii) ammonium persulfate [abbreviated as APS; final concentration, 0.2% (w/v)] as an initiator of gelation. Tissue sections on glass slides were covered with gelling solution, and then a gel chamber was constructed by first placing two no. 1.5 square coverslips (22 mm by 22 mm) as spacers, one at each end of the glass slide and flanking the tissue section in the middle; then, a rectangular coverslip was placed on top of spacers to enclose the gel chamber in which the tissue sample was fully immersed in the gelling solution and sandwiched by the glass slide and the top coverslip. Samples were first incubated in a humidified atmosphere at 4°C for 30 min, which slows down gelation rate and enables diffusion of solution into tissues and subsequently incubated in a humidified atmosphere at 37°C for 2.5 hours to complete gelation (Fig. 1B and figs. S1B, S2B, S3B, and S4B).

Softening

After gelation, all coverslips were gently removed from the glass slide that carries the gelled tissue. Excessive gel around the tissue sample was trimmed away using a razor blade. Then, tissues were incubated in the softening buffer, which consists of 20% (w/v) SDS, 100 mM β-mercaptoethanol, 25 mM EDTA, 0.5% Triton X-100, and 50 mM tris at pH 8, at 37°C for 30 min followed by 1 hour in an autoclave at 121°C, followed by cooling to RT for 30 min (Fig. 1C and figs. S1C, S2D, S3C, and S4D). Tissues were observed to detach from the glass slides during softening or during subsequent washes with gentle shaking.

Expansion with post-decrowding methoxy-xO4 or NHS ester staining

After softening, tissue underwent either decrowding (Fig. 1D and fig. S1D), expansion with postexpansion methoxy-O4 staining and expansion without postexpansion immunostaining (fig. S3D), or decrowding with NHS ester postexpansion staining (fig. S9). After softening, the gelled tissue detached from the slide and was floating freely in the softening buffer. The tissue was transferred into a clear polystyrene petri dish plate by slowly decanting the buffer solution that contained the gelled tissue into the plate. Then, using a pipette, the excess buffer was removed and discarded. Then, 1× PBS was added to the well plate to fully cover the tissue, and the petri dish plate was gently shaken at RT to remove excess softening buffer. Then, while the gelled tissue was free floating in 1× PBS, we used a flat, wide mini paintbrush that we then placed underneath the gelled tissue, ensuring that the paint brush was covering most of the gelled tissue undersurface area, and transferred it into a clear six-well plate (Clearstar) that contained 1× PBS to completely submerge the tissue. Then, the well plate was gently shaken at RT for 3 min. Then, the excess 1× PBS was removed using a pipette, new 1× PBS was added to cover the tissue, and the well plate was gently shaken at RT for 3 min. This process was repeated a total of five times, which results in tissues reaching an expansion factor of ~2.3× (Fig. 1D and figs. S1D, S2E, and S3E). For decrowding, tissues were washed five times with 1× PBS at RT for 3 min each. At this stage, tissues were at a partially expanded state, with ~2.3× linear expansion factor. For expansion with methoxy-x04 (Biotechne, #4920), tissues were stained with methoxy-x04 at a concentration of 0.01 mg/ml in 1× PBS for 2 hours at RT and then additionally washed in deionized water three to five times at RT for 3 min each, expanding the hydrogel-embedded tissue to an expansion factor of ~4× (4, 15, 19). For decrowding with NHS ester post-decrowding staining, we used Alexa Fluor 647 succinimidyl ester at the same concentration and conditions as for preexpansion staining. For expansion without postexpansion immunostaining, tissues were then additionally washed in deionized water three to five times at RT for 3 min each to expand the hydrogel-embedded tissue to an expansion factor of ~4× (fig. S3D) (4, 15, 19). A subset of tissue samples was imaged by confocal microscopy at this state, with methods described in the "Image acquisition" section, to obtain the postexpansion and pre-decrowding staining images.

Post-decrowding immunostaining

Tissues underwent decrowding by washing five times with 1× PBS at RT for 3 min, which resulted in an expansion factor of ~2.3× (Fig. 1D and figs. S1D, S2E, and S3E). Then, while the gelled tissue was free floating in 1× PBS, we used a flat, wide mini paintbrush placed underneath the gelled tissue, ensuring that the paint brush was covering most of the gelled tissue undersurface area, and transferred it into a new six-well plate (CellVis) that was subsequently used for imaging containing 1× PBS. We prepared antibody solutions by diluting primary antibody in MAXbind Staining buffer (Active Motif, #15253) and performed post-decrowding immunostaining (Fig. 1E and figs. S1E, S2F, and S3F) by incubating tissue samples in the antibody solution at 37°C for 1 hour, at RT for 2.5 hours, or at 4°C overnight. Next, excess antibody solution was removed with a pipette, and the tissues were washed three times with MAXwash buffer (Active Motif, #15254) at RT for 3 min, each time removing excess MAXwash buffer with a pipette. The same procedure conditions were applied for secondary antibodies. For

tissues that underwent both preexpansion and post-decrowding staining, antibody concentrations and incubation conditions were identical to ensure quantitative comparisons pre- and postexpansion. Immunostained tissues were imaged at ~2.3× linear expansion or further expanded by washing with deionized water at RT for three to five times for 3 min each to ~4× linear expansion (Fig. 1E and fig. S3F). Then, excess deionized water was removed from the well plate, and the gelled tissue was ready for imaging with a confocal microscope by imaging through the clear glass of the well plate. We performed confocal microscopy at the ~4× state, adhering to the protocol described in the "Image acquisition" section, to obtain post-decrowding staining images. Once imaged, tissue can be stored by adding 1× PBS to completely cover tissue and ensuring the container is covered so tissue does not dry out. Fully ~4× expanded gelled tissues are friable and can easily break if the user tries to lift them up and out of the well plate with a paint brush. To transfer gels between containers, we did so in the ~2.3× state by washing ~4× expanded gelled tissues in 1× PBS five times at RT. A step-by-step protocol is found in the Supplementary Materials.

Tissue shrinking

We shrunk tissues to a ~ 1.3× linear expansion factor by treating with a high–ionic strength buffer (1 M NaCl + 60 mM MgCl$_2$) (*19*) after the softening (fig. S3C) and washing with PBS (which results in an expansion factor of ~2.3×) or after post-decrowding staining and washing with PBS (which results in an expansion factor of ~2.3×). Specifically, we washed the tissues three to five times with this buffer at RT for 3 min each, until no more tissue shrinkage was observed. We then performed confocal microscopy at this stage, with methods described in the "Image acquisition" section, to obtain pre-decrowding or post-decrowding staining at shrunken state images.

Imaging processing methods

Image acquisition

For confocal imaging, we used a spinning disk confocal system (CSU-W1, Yokogawa) on a Nikon Ti-E microscope. The objective lenses that we used include a 40× 1.15 numerical aperture (NA) water immersion objective or 10× 0.20 NA air objective. The excitation lasers and emission filters that we used to image each fluorescent dye are the following: 405-nm excitation, 450/50-nm emission filter; 488-nm excitation, 525/40-nm emission filter; 561-nm excitation, 607/36-nm emission filter; 640-nm excitation, 685/40-nm emission filter. The following acquisition and display settings apply to all images shown in this study, unless otherwise specified: (i) Within the same experiment (as grouped by figures and described in Results and figure legends), all images were obtained with the same laser power, camera settings, and objective lens. (ii) For all image display in all figures except Fig. 4, brightness and contrast settings were first individually set by the automated adjustment function in ImageJ and then manually adjusted (raising the minimum intensity threshold and lowering the maximum intensity threshold) to improve contrast for features of interest. For the image display of Fig. 4, brightness and contrast settings of images were adjusted so that 1% of the pixels was saturated. None of these changes in the brightness and contrast settings, throughout the entire study, affected the downstream quantitative analysis of fluorescent intensities, which were always applied on raw images, as specified in Results and captions.

For SR-SIM of samples in the preexpansion state, for isotropy analyses (Fig. 2, A and B) and comparative analyses (Fig. 5, A and B), we used a Deltavision OMX Blaze (GE Healthcare) SR-SIM microscope with a 100× 1.40 NA (Olympus) oil objective to acquire the images. Please see the Supplementary Materials for details on image processing methods for (i) distortion quantification; (ii) image registration between preexpansion and postexpansion images; (iii) image registration between post-expansion images and post-decrowding ~4× expanded Images; (iv) image registration between preexpansion, pre-decrowding, post-decrowding 1× state and ~4× expanded images; (v) quantification of lipofuscin autofluorescence removal; (vi) fluorescence quantification for protein decrowding; (vii) quantification of β amyloid plaque autofluorescence removal; and (viii) quantification of fluorescence colocalization of vimentin, Iba1, and GFAP in low-grade gliomas.

Supplementary Materials

This PDF file includes:
Materials and Methods
Step-by-step protocol
Figs. S1 to S15
Tables S1 and S2
References (*108–144*)

Other Supplementary Material for this manuscript includes the following:
Movies S1 to S2
Data file S1
MDAR Reproducibility Checklist

REFERENCES AND NOTES

1. M. Maidorn, S. O. Rizzoli, F. Opazo, Tools and limitations to study the molecular composition of synapses by fluorescence microscopy. *Biochem. J.* **473**, 3385–3399 (2016).
2. S. P. Kent, K. H. Ryan, A. L. Siegel, Steric hindrance as a factor in the reaction of labeled antibody with cell surface antigenic determinants. *J. Histochem. Cytochem.* **26**, 618–621 (1978).
3. F. E. Zilly, N. D. Halemani, D. Walrafen, L. Spitta, A. Schreiber, R. Jahn, T. Lang, Ca2+ induces clustering of membrane proteins in the plasma membrane via electrostatic interactions. *EMBO J.* **30**, 1209–1220 (2011).
4. Y. Zhao, O. Bucur, H. Irshad, F. Chen, A. Weins, A. L. Stancu, E. Y. Oh, M. DiStasio, V. Torous, B. Glass, I. E. Stillman, S. J. Schnitt, A. H. Beck, E. S. Boyden, Nanoscale imaging of clinical specimens using pathology-optimized expansion microscopy. *Nat. Biotechnol.* **35**, 757–764 (2017).
5. S. J. Sahl, S. W. Hell, S. Jakobs, Fluorescence nanoscopy in cell biology. *Nat. Rev. Mol. Cell Biol.* **18**, 685–701 (2017).
6. J. Ries, C. Kaplan, E. Platonova, H. Eghlidi, H. Ewers, A simple, versatile method for GFP-based super-resolution microscopy via nanobodies. *Nat. Methods* **9**, 582–584 (2012).
7. E. F. Fornasiero, F. Opazo, Super-resolution imaging for cell biologists. *Bioessays* **37**, 436–451 (2015).
8. T. Lang, S. O. Rizzoli, Membrane protein clusters at nanoscale resolution: More than pretty pictures. *Physiology (Bethesda)* **25**, 116–124 (2010).
9. M. Maidorn, A. Olichon, S. O. Rizzoli, F. Opazo, Nanobodies reveal an extra-synaptic population of SNAP-25 and Syntaxin 1A in hippocampal neurons. *MAbs* **11**, 305–321 (2019).
10. A. Hatami, R. Albay III, S. Monjazeb, S. Milton, C. Glabe, Monoclonal antibodies against Aβ42 fibrils distinguish multiple aggregation state polymorphisms in vitro and in Alzheimer disease brain. *J. Biol. Chem.* **289**, 32131–32143 (2014).
11. F. Opazo, M. Levy, M. Byrom, C. Schäfer, C. Geisler, T. W. Groemer, A. D. Ellington, S. O. Rizzoli, Aptamers as potential tools for super-resolution microscopy. *Nat. Methods* **9**, 938–939 (2012).
12. M. Mikhaylova, B. M. C. Cloin, K. Finan, R. van den Berg, J. Teeuw, M. M. Kijanka, M. Sokolowski, E. A. Katrukha, M. Maidorn, F. Opazo, S. Moutel, M. Vantard, F. Perez, P. M. P. van Bergen en Henegouwen, C. C. Hoogenraad, H. Ewers, L. C. Kapitein, Resolving bundled microtubules using anti-tubulin nanobodies. *Nat. Commun.* **6**, 7933 (2015).
13. L. J. Harris, E. Skaletsky, A. McPherson, Crystallographic structure of an intact IgG1 monoclonal antibody. *J. Mol. Biol.* **275**, 861–872 (1998).
14. B. Huang, M. Bates, X. Zhuang, Super-resolution fluorescence microscopy. *Annu. Rev. Biochem.* **78**, 993–1016 (2009).
15. F. Chen, P. W. Tillberg, E. S. Boyden, Optical imaging. Expansion microscopy. *Science* **347**, 543–548 (2015).

Valdes *et al.*, *Sci. Transl. Med.* **16**, eabo0049 (2024) 31 January 2024

14 of 17

16. A. T. Wassie, Y. Zhao, E. S. Boyden, Expansion microscopy: Principles and uses in biological research. *Nat. Methods* **16**, 33–41 (2019).

17. D. Gambarotto, F. U. Zwettler, M. le Guennec, M. Schmidt-Cernohorska, D. Fortun, S. Borgers, J. Heine, J. G. Schloetel, M. Reuss, M. Unser, E. S. Boyden, M. Sauer, V. Hamel, P. Guichard, Imaging cellular ultrastructures using expansion microscopy (U-ExM). *Nat. Methods* **16**, 71–74 (2019).

18. T. Ku, J. Swaney, J. Y. Park, A. Albanese, E. Murray, J. H. Cho, Y. G. Park, V. Mangena, J. Chen, K. Chung, Multiplexed and scalable super-resolution imaging of three-dimensional protein localization in size-adjustable tissues. *Nat. Biotechnol.* **34**, 973–981 (2016).

19. P. W. Tillberg, F. Chen, K. D. Piatkevich, Y. Zhao, C. C. Yu, B. P. English, L. Gao, A. Martorell, H. J. Suk, F. Yoshida, E. M. DeGennaro, D. H. Roossien, G. Gong, U. Seneviratne, S. R. Tannenbaum, R. Desimone, D. Cai, E. S. Boyden, Protein-retention expansion microscopy of cells and tissues labeled using standard fluorescent proteins and antibodies. *Nat. Biotechnol.* **34**, 987–992 (2016).

20. F. Y. Shen, M. M. Harrington, L. A. Walker, H. P. J. Cheng, E. S. Boyden, D. Cai, Light microscopy based approach for mapping connectivity with molecular specificity. *Nat. Commun.* **11**, 4632 (2020).

21. O. M'Saad, J. Bewersdorf, Light microscopy of proteins in their ultrastructural context. *Nat. Commun.* **11**, 3850 (2020).

22. F. U. Zwettler, S. Reinhard, D. Gambarotto, T. D. M. Bell, V. Hamel, P. Guichard, M. Sauer, Molecular resolution imaging by post-labeling expansion single-molecule localization microscopy (Ex-SMLM). *Nat. Commun.* **11**, 3388 (2020).

23. E. D. Karagiannis, J. S. Kang, T. W. Shin. A. Emenari, S. Asano, L. Lin, E. K. Costa, IMAXT Grand Challenge Consortium; A. H. Marblestone, N. Kasthuri, E. S. Boyden, Expansion Microscopy of Lipid Membranes. *bioRxiv*. (2019), https://biorxiv.org/content/10.1101/829903v1.

24. C.-C.J. Yu, N. C. Barry, A. T. Wassie, A. Sinha, A. Bhattacharya, S. Asano, C. Zhang, F. Chen, O. Hobert, M. B. Goodman, G. Haspel, E. S. Boyden, Expansion microscopy of C. elegans. *eLife* **9**, e46249 (2020).

25. D. Sarkar, J. Kang, A. T. Wassie, M. E. Schroeder, Z. Peng, T. B. Tarr, A. H. Tang, E. D. Niederst, J. Z. Young, H. Su, D. Park, P. Yin, L. H. Tsai, T. A. Blanpied, E. S. Boyden, Revealing nanostructures in brain tissue via protein decrowding by iterative expansion microscopy. *Nat Biomed Eng* **6**, 1057–1073 (2022).

26. D. Sarkar, J. Kang, A. T. Wassie, M. E. Schroeder, Z. Peng, T. B. Tarr, A.-H. Tang, E. Niederst, J. Z. Young, L.-H. Tsai, T. A. Blanpied, E. S. Boyden, Expansion Revealing: Decrowding Proteins to Unmask Invisible Brain Nanostructures. *bioRxiv*, (2020), https://biorxiv.org/content/10.1101/2020.08.29.273540v1.

27. M. Schmid, T. K. Prinz, A. Stabler, S. Sangerlaub, Effect of sodium sulfite, sodium dodecyl sulfate, and urea on the molecular interactions and properties of whey protein isolate-based films. *Front. Chem.* **4**, 49 (2016).

28. H. Xu, Y. Yang, Controlled De-Cross-Linking and Disentanglement of Feather Keratin for Fiber Preparation via a Novel Process. *ACS Sustain. Chem. Eng.* **2**, 1404–1410 (2014).

29. M. Aumailley, The laminin family. *Cell Adh. Migr.* **7**, 48–55 (2013).

30. R. Glockshuber, T. Schmidt, A. Pluckthun, The disulfide bonds in antibody variable domains: Effects on stability, folding in vitro, and functional expression in Escherichia coli. *Biochemistry* **31**, 1270–1279 (1992).

31. A. L. Grigorian, J. J. Bustamante, P. Hernandez, A. O. Martinez, L. S. Haro, Extraordinarily stable disulfide-linked homodimer of human growth hormone. *Protein Sci.* **14**, 902–913 (2005).

32. Y.-G. Park, C. H. Sohn, R. Chen, M. M. Cue, D. H. Yun, G. T. Drummond, T. Ku, N. B. Evans, H. C. Oak, W. Trieu, H. Choi, X. Jin, V. Lilascharoen, J. Wang, M. C. Truttmann, H. W. Qi, H. L. Ploegh, T. R. Golub, S.-C. Chen, M. P. Frosch, H. J. Kulik, B. K. Lim, K. Chung, Protection of tissue physicochemical properties using polyfunctional crosslinkers. *Nat. Biotechnol.*, (2019).

33. P. Kleihues, F. Soylemezoglu, B. Schauble, B. W. Scheithauer, P. C. Burger, Histopathology, classification, and grading of gliomas. *Glia* **15**, 211–221 (1995).

34. J. B. Chang, F. Chen, Y. G. Yoon, E. E. Jung, H. Babcock, J. S. Kang, S. Asano, H. J. Suk, N. Pak, P. W. Tillberg, A. T. Wassie, D. Cai, E. S. Boyden, Iterative expansion microscopy. *Nat. Methods* **14**, 593–599 (2017).

35. F. Chen, A. T. Wassie, A. J. Cote, A. Sinha, S. Alon, S. Asano, E. R. Daugharthy, J. B. Chang, A. Marblestone, G. M. Church, A. Raj, E. S. Boyden, Nanoscale imaging of RNA with expansion microscopy. *Nat. Methods* **13**, 679–684 (2016).

36. N. Hirokawa, S. Hisanaga, Y. Shiomura, MAP2 is a component of crossbridges between microtubules and neurofilaments in the neuronal cytoskeleton: Quick-freeze, deep-etch immunoelectron microscopy and reconstitution studies. *J. Neurosci.* **8**, 2769–2779 (1988).

37. A. Yuan, M. V. Rao, Veeranna, R. P. Nixon, Neurofilaments and neurofilament proteins in health and disease. *Cold Spring Harb. Perspect. Biol.* **9**, a018309 (2017).

38. T. Yamada, T. Kawamata, D. G. Walker, P. L. McGeer, Vimentin immunoreactivity in normal and pathological human brain tissue. *Acta Neuropathol.* **84**, 157–162 (1992).

39. E. Wang, J. G. Cairncross, R. K. Liem, Identification of glial filament protein and vimentin in the same intermediate filament system in human glioma cells. *Proc. Natl. Acad. Sci. U.S.A.* **81**, 2102–2106 (1984).

40. F. D'Amico, E. Skarmoutsou, F. Stivala, State of the art in antigen retrieval for immunohistochemistry. *J. Immunol. Methods* **341**, 1–18 (2009).

41. D. Brown, J. Lydon, M. McLaughlin, A. Stuart-Tilley, R. Tyszkowski, S. Alper, Antigen retrieval in cryostat tissue sections and cultured cells by treatment with sodium dodecyl sulfate (SDS). *Histochem. Cell Biol.* **105**, 261–267 (1996).

42. O. J. Gustafsson, G. Arentz, P. Hoffmann, Proteomic developments in the analysis of formalin-fixed tissue. *Biochim. Biophys. Acta* **1854**, 559–580 (2015).

43. J. N. Keller, E. Dimayuga, Q. Chen, J. Thorpe, J. Gee, Q. Ding, Autophagy, proteasomes, lipofuscin, and oxidative stress in the aging brain. *Int. J. Biochem. Cell Biol.* **36**, 2376–2391 (2004).

44. J. Kaluzny, P. Purta, Z. Poskin, J. D. Rogers, A. A. Fawzi, Ex vivo confocal spectroscopy of autofluorescence in age-related macular degeneration. *PLOS ONE* **11**, e0162869 (2016).

45. H. Tohma, A. R. Hepworth, T. Shavlakadze, M. D. Grounds, P. G. Arthur, Quantification of ceroid and lipofuscin in skeletal muscle. *J. Histochem. Cytochem.* **59**, 769–779 (2011).

46. P. V. Belichenko, A. A. Fedorov, A. B. Dahlstrom, Quantitative analysis of immunofluorescence and lipofuscin distribution in human cortical areas by dual-channel confocal laser scanning microscopy. *J. Neurosci. Methods* **69**, 155–161 (1996).

47. A. Legrand, G. Alonso, Pregnenolone reverses the age-dependent accumulation of glial fibrillary acidic protein within astrocytes of specific regions of the rat brain. *Brain Res.* **802**, 125–133 (1998).

48. G. Bing, X. V. Nguyen, M. Liu, W. R. Markesbery, A. Sun, Biophysical and biochemical characterization of the intrinsic fluorescence from neurofibrillary tangles. *Neurobiol. Aging* **27**, 823–830 (2006).

49. D. Yin, Biochemical basis of lipofuscin, ceroid, and age pigment-like fluorophores. *Free Radic. Biol. Med.* **21**, 871–888 (1996).

50. T. Jung, N. Bader, T. Grune, Lipofuscin. *Ann. N. Y. Acad. Sci.* **1119**, 97–111 (2007).

51. A. Moreno-Garcia, A. Kun, O. Calero, M. Medina, M. Calero, An overview of the role of lipofuscin in age-related neurodegeneration. *Front. Neurosci.* **12**, 464 (2018).

52. U. T. Brunk, A. Terman, Lipofuscin: Mechanisms of age-related accumulation and influence on cell function. *Free Radic. Biol. Med.* **33**, 611–619 (2002).

53. S. S. Kushwaha, N. Patro, I. K. Patro, A sequential study of age-related lipofuscin accumulation in hippocampus and striate cortex of rats. *Ann Neurosci.* **25**, 223–233 (2019).

54. Y. Kakimoto, C. Okada, N. Kawabe, A. Sasaki, H. Tsukamoto, R. Nagao, M. Osawa, Myocardial lipofuscin accumulation in ageing and sudden cardiac death. *Sci. Rep.* **9**, 3304 (2019).

55. A. D. Linstedt, H. P. Hauri, Giantin, a novel conserved Golgi membrane protein containing a cytoplasmic domain of at least 350 kDa. *Mol. Biol. Cell* **4**, 679–693 (1993).

56. M. Lowe, Structural organization of the Golgi apparatus. *Curr. Opin. Cell Biol.* **23**, 85–93 (2011).

57. B. Wiedenmann, W. W. Franke, Identification and localization of synaptophysin, an integral membrane glycoprotein of Mr 38,000 characteristic of presynaptic vesicles. *Cell* **41**, 1017–1028 (1985).

58. E. M. Hol, M. Pekny, Glial fibrillary acidic protein (GFAP) and the astrocyte intermediate filament system in diseases of the central nervous system. *Curr. Opin. Cell Biol.* **32**, 121–130 (2015).

59. M. V. Sofroniew, H. V. Vinters, Astrocytes: Biology and pathology. *Acta Neuropathol.* **119**, 7–35 (2010).

60. A. Caceres, G. A. Banker, L. Binder, Immunocytochemical localization of tubulin and microtubule-associated protein 2 during the development of hippocampal neurons in culture. *J. Neurosci.* **6**, 714–722 (1986).

61. E. A. Bushong, M. E. Martone, Y. Z. Jones, M. H. Ellisman, Protoplasmic astrocytes in CA1 stratum radiatum occupy separate anatomical domains. *J. Neurosci.* **22**, 183–192 (2002).

62. J. A. Colombo, S. Gayol, A. Yanez, P. Marco, Immunocytochemical and electron microscope observations on astroglial interlaminar processes in the primate neocortex. *J. Neurosci. Res.* **48**, 352–357 (1997).

63. F. M. Brehar, D. Arsene, L. A. Brinduse, M. R. Gorgan, Immunohistochemical analysis of GFAP-δ and nestin in cerebral astrocytomas. *Brain Tumor Pathol.* **32**, 90–98 (2015).

64. M. Brenner, Role of GFAP in CNS injuries. *Neurosci. Lett.* **565**, 7–13 (2014).

65. K. C. Choi, S. E. Kwak, J. E. Kim, S. H. Sheen, T. C. Kang, Enhanced glial fibrillary acidic protein-delta expression in human astrocytic tumor. *Neurosci. Lett.* **463**, 182–187 (2009).

66. L. Alarcon-Martinez, S. Yilmaz-Ozcan, M. Yemisci, J. Schallek, K. Kılıç, A. Can, A. di Polo, T. Dalkara, Capillary pericytes express α-smooth muscle actin, which requires prevention of filamentous-actin depolymerization for detection. *eLife* **7**, e34861 (2018).

67. M. M. Verbeek, I. Otte-Holler, P. Wesseling, D. J. Ruiter, R. M. de Waal, Induction of alpha-smooth muscle actin expression in cultured human brain pericytes by transforming growth factor-beta 1. *Am. J. Pathol.* **144**, 372–382 (1994).

68. T. Yamazaki, Y. S. Mukouyama, Tissue specific origin, development, and pathological perspectives of pericytes. *Front. Cardiovasc. Med.* **5**, 78 (2018).

69. G. Bergers, S. Song, The role of pericytes in blood-vessel formation and maintenance. *Neuro Oncol.* **7**, 452–464 (2005).

70. M. J. Herpers, F. C. Ramaekers, J. Aldeweireldt, O. Moesker, J. Slooff, Co-expression of glial fibrillary acidic protein- and vimentin-type intermediate filaments in human astrocytomas. *Acta Neuropathol.* **70**, 333–339 (1986).

71. M. B. Graeber, W. J. Streit, G. W. Kreutzberg, The microglial cytoskeleton: Vimentin is localized within activated cells in situ. *J. Neurocytol.* **17**, 573–580 (1988).

72. L. Diaz-Flores, R. Gutierrez, H. Varela, N. Rancel, F. Valladares, Microvascular pericytes: A review of their morphological and functional characteristics. *Histol. Histopathol.* **6**, 269–286 (1991).

73. L. Cheng, Z. Huang, W. Zhou, Q. Wu, S. Donnola, J. K. Liu, X. Fang, A. E. Sloan, Y. Mao, J. D. Lathia, W. Min, R. E. McLendon, J. N. Rich, S. Bao, Glioblastoma stem cells generate vascular pericytes to support vessel function and tumor growth. *Cell* **153**, 139–152 (2013).

74. M. H. Deininger, K. Seid, S. Engel, R. Meyermann, H. J. Schluesener, Allograft inflammatory factor-1 defines a distinct subset of infiltrating macrophages/microglial cells in rat and human gliomas. *Acta Neuropathol.* **100**, 673–680 (2000).

75. E. Saavedra-López, M. Roig-Martínez, G. P. Cribaro, P. V. Casanova, J. M. Gallego, A. Pérez-Vallés, C. Barcia, Phagocytic glioblastoma-associated microglia and macrophages populate invading pseudopalisades. *Brain Commun.* **2**, cz043 (2020).

76. P. Díaz-Amarilla, S. Olivera-Bravo, E. Trias, A. Cragnolini, L. Martínez-Palma, P. Cassina, J. Beckman, L. Barbeito, Phenotypically aberrant astrocytes that promote motoneuron damage in a model of inherited amyotrophic lateral sclerosis. *Proc. Natl. Acad. Sci. U.S.A.* **108**, 18126–18131 (2011).

77. Y. M. Morizawa, Y. Hirayama, N. Ohno, S. Shibata, E. Shigetomi, Y. Sui, J. Nabekura, K. Sato, F. Okajima, H. Takebayashi, H. Okano, S. Koizumi, Reactive astrocytes function as phagocytes after brain ischemia via ABCA1-mediated pathway. *Nat. Commun.* **8**, 28 (2017).

78. L. C. Huysentruyt, Z. Akgoc, T. N. Seyfried, Hypothesis: Are neoplastic macrophages/microglia present in glioblastoma multiforme? *ASN Neuro* **3**, AN20110011 (2011).

79. A. Persson, E. Englund, Phagocytic properties in tumor astrocytes. *Neuropathology* **32**, 252–260 (2012).

80. M. A. Gomes de Castro, C. Hobartner, F. Opazo, Aptamers provide superior stainings of cellular receptors studied under super-resolution microscopy. *PLOS ONE* **12**, e0173050 (2017).

81. M. A. DeTure, D. W. Dickson, The neuropathological diagnosis of Alzheimer's disease. *Mol. Neurodegener.* **14**, 32 (2019).

82. A. Serrano-Pozo, M. P. Frosch, E. Masliah, B. T. Hyman, Neuropathological alterations in Alzheimer disease. *Cold Spring Harb. Perspect. Med.* **1**, a006189 (2011).

83. P. Cras, M. Kawai, D. Lowery, P. Gonzalez-DeWhitt, B. Greenberg, G. Perry, Senile plaque neurites in Alzheimer disease accumulate amyloid precursor protein. *Proc. Natl. Acad. Sci. U.S.A.* **88**, 7552–7556 (1991).

84. D. P. Perl, Neuropathology of Alzheimer's disease. *Mt. Sinai J. Med.* **77**, 32–42 (2010).

85. M. Querol-Vilaseca, M. Colom-Cadena, J. Pegueroles, R. Nuñez-Llaves, J. Luque-Cabecerans, L. Muñoz-Llahuna, J. Andilla, O. Belbin, T. L. Spires-Jones, E. Gelpi, J. Clarimon, J. Loza-Alvarez, J. Fortea, A. Lleó, Nanoscale structure of amyloid-β plaques in Alzheimer's disease. *Sci. Rep.* **9**, 5181 (2019).

86. M. G. Mendez, S.-I. Kojima, R. D. Goldman, Vimentin induces changes in cell shape, motility, and adhesion during the epithelial to mesenchymal transition. *FASEB J.* **24**, 1838–1851 (2010).

87. L. Lin, G. Wang, J. Ming, X. Meng, B. Han, B. Sun, J. Cai, C. Jiang, Analysis of expression and prognostic significance of vimentin and the response to temozolomide in glioma patients. *Tumour Biol.* **37**, 15333–15339 (2016).

88. M. O. Nowicki, J. L. Hayes, E. A. Chiocca, S. E. Lawler, Proteomic analysis implicates vimentin in glioblastoma cell migration. *Cancers* **11**, 466 (2019).

89. H. J. Jan, C. C. Lee, Y. L. Shih, D. Y. Hueng, H. I. Ma, J. H. Lai, H. W. Wei, H. M. Lee, Osteopontin regulates human glioma cell invasiveness and tumor growth in mice. *Neuro Oncol.* **12**, 58–70 (2010).

90. J. Zhao, L. Zhang, X. Dong, L. Liu, L. Huo, H. Chen, High expression of vimentin is associated with progression and a poor outcome in glioblastoma. *Appl. Immunohistochem. Mol. Morphol.* **26**, 337–344 (2018).

91. S. X. Jiang, J. Slinn, A. Aylsworth, S. T. Hou, Vimentin participates in microglia activation and neurotoxicity in cerebral ischemia. *J. Neurochem.* **122**, 764–774 (2012).

92. E. J. van Bodegraven, J. V. van Asperen, P. A. J. Robe, E. M. Hol, Importance of GFAP isoform-specific analyses in astrocytoma. *Glia* **67**, 1417–1433 (2019).

93. L. Lau, Y. L. Lee, S. J. Sahl, T. Stearns, W. E. Moerner, STED microscopy with optimized labeling density reveals 9-fold arrangement of a centriole protein. *Biophys. J.* **102**, 2926–2935 (2012).

94. W. Liedtke, W. Edelmann, F. C. Chiu, R. Kucherlapati, C. S. Raine, Experimental autoimmune encephalomyelitis in mice lacking glial fibrillary acidic protein is characterized by a more severe clinical course and an infiltrative central nervous system lesion. *Am. J. Pathol.* **152**, 251–259 (1998).

95. K. Xu, A. T. Malouf, A. Messing, J. Silver, Glial fibrillary acidic protein is necessary for mature astrocytes to react to beta-amyloid. *Glia* **25**, 390–403 (1999).

96. W. Liedtke, W. Edelmann, P. L. Bieri, F. C. Chiu, N. J. Cowan, R. Kucherlapati, C. S. Raine, GFAP is necessary for the integrity of CNS white matter architecture and long-term maintenance of myelination. *Neuron* **17**, 607–615 (1996).

97. M. Pekny, K. A. Stanness, C. Eliasson, C. Betsholtz, D. Janigro, Impaired induction of blood-brain barrier properties in aortic endothelial cells by astrocytes from GFAP-deficient mice. *Glia* **22**, 390–400 (1998).

98. C. De Pascalis, C. Pérez-González, S. Seetharaman, B. Boëda, B. Vianay, M. Burute, C. Leduc, N. Borghi, X. Trepat, S. Etienne-Manneville, Intermediate filaments control collective migration by restricting traction forces and sustaining cell-cell contacts. *J. Cell Biol.* **217**, 3031–3044 (2018).

99. G. Reifenberger, T. Bilzer, R. J. Seitz, W. Wechsler, Expression of vimentin and glial fibrillary acidic protein in ethylnitrosourea-induced rat gliomas and glioma cell lines. *Acta Neuropathol.* **78**, 270–282 (1989).

100. R. A. Battaglia, S. Delic, H. Herrmann, N. T. Snider, Vimentin on the move: New developments in cell migration. *F1000Res.* **7**, 1796 (2018).

101. M. Osswald, E. Jung, F. Sahm, G. Solecki, V. Venkataramani, J. Blaes, S. Weil, H. Horstmann, B. Wiestler, M. Syed, L. Huang, M. Ratliff, K. Karimian Jazi, F. T. Kurz, T. Schmenger, D. Lemke, M. Gömmel, M. Pauli, Y. Liao, P. Häring, S. Pusch, V. Herl, C. Steinhäuser, D. Krunic, H. Jarahian, H. Miletic, A. S. Berghoff, O. Griesbeck, G. Kalamakis, O. Garaschuk, M. Preusser, S. Weiss, H. Liu, S. Heiland, M. Platten, P. E. Huber, T. Kuner, A. von Deimling, W. Wick, F. Winkler, Brain tumour cells interconnect to a functional and resistant network. *Nature* **528**, 93–98 (2015).

102. S. Weil, M. Osswald, G. Solecki, J. Grosch, E. Jung, D. Lemke, M. Ratliff, D. Hänggi, W. Wick, F. Winkler, Tumor microtubes convey resistance to surgical lesions and chemotherapy in gliomas. *Neuro Oncol.* **19**, 1316–1326 (2017).

103. C. E. Lewis, J. W. Pollard, Distinct role of macrophages in different tumor microenvironments. *Cancer Res.* **66**, 605–612 (2006).

104. B. Z. Qian, J. W. Pollard, Macrophage diversity enhances tumor progression and metastasis. *Cell* **141**, 39–51 (2010).

105. C. Kubelt, K. Hattermann, S. Sebens, H. M. Mehdorn, J. Held-Feindt, Epithelial-to-mesenchymal transition in paired human primary and recurrent glioblastomas. *Int. J. Oncol.* **46**, 2515–2525 (2015).

106. S. Alon, D. R. Goodwin, A. Sinha, A. T. Wassie, F. Chen, E. R. Daugharthy, Y. Bando, A. Kajita, A. G. Xue, K. Marrett, R. Prior, Y. Cui, A. C. Payne, C.-C. Yao, H.-J. Suk, R. Wang, C.-C.J. Yu, P. Tillberg, P. Reginato, N. Pak, S. Liu, S. Punthambaker, E. P. R. Iyer, R. E. Kohman, J. A. Miller, E. S. Lein, A. Lako, N. Cullen, S. Rodig, K. Helvie, D. L. Abravanel, N. Wagle, B. E. Johnson, J. Klughammer, M. Slyper, J. Waldman, J. Jané-Valbuena, O. Rozenblatt-Rosen, A. Regev, IMAXT Consortium, G. M. Church, A. H. Marblestone, E. S. Boyden, Expansion sequencing: Spatially precise in situ transcriptomics in intact biological systems. *Science* **371**, eaax2656 (2021).

107. R. Gao, S. M. Asano, S. Upadhyayula, I. Pisarev, D. E. Milkie, T. L. Liu, V. Singh, A. Graves, G. H. Huynh, Y. Zhao, J. Bogovic, J. Colonell, C. M. Ott, C. Zugates, S. Tappan, A. Rodriguez, K. R. Mosaliganti, S. H. Sheu, H. A. Pasolli, S. Pang, C. S. Xu, S. G. Megason, H. Hess, J. Lippincott-Schwartz, A. Hantman, G. M. Rubin, T. Kirchhausen, S. Saalfeld, Y. Aso, E. S. Boyden, E. Betzig, Cortical column and whole-brain imaging with molecular contrast and nanoscale resolution. *Science* **363**, eaau8302 (2019).

108. A. Olar, K. M. Wani, K. D. Alfaro-Munoz, L. E. Heathcock, H. F. van Thuijl, M. R. Gilbert, T. S. Armstrong, E. P. Sulman, D. P. Cahill, E. Vera-Bolanos, Y. Yuan, J. C. Reijneveld, B. Ylstra, P. Wesseling, K. D. Aldape, IDH mutation status and role of WHO grade and mitotic index in overall survival in grade II-III diffuse gliomas. *Acta Neuropathol.* **129**, 585–596 (2015).

109. M. P. Pusztaszeri, W. Seelentag, F. T. Bosman, Immunohistochemical expression of endothelial markers CD31, CD34, von Willebrand factor, and Fli-1 in normal human tissues. *J. Histochem. Cytochem.* **54**, 385–395 (2006).

110. S. F. De Meyer, G. Stoll, D. D. Wagner, C. Kleinschnitz, von Willebrand factor: An emerging target in stroke therapy. *Stroke* **43**, 599–606 (2012).

111. A. C. Yang, R. T. Vest, F. Kern, D. P. Lee, M. Agam, C. A. Maat, P. M. Losada, M. B. Chen, N. Schaum, N. Khoury, A. Toland, K. Calcuttawala, H. Shin, R. Pálovics, A. Shin, E. Y. Wang, J. Luo, D. Gate, W. J. Schulz-Schaeffer, P. Chu, J. A. Siegenthaler, M. W. McNerney, A. Keller, T. Wyss-Coray, A human brain vascular atlas reveals diverse mediators of Alzheimer's risk. *Nature* **603**, 885–892 (2022).

112. W. K. Yung, M. Luna, A. Borit, Vimentin and glial fibrillary acidic protein in human brain tumors. *J. Neurooncol* **3**, 35–38 (1985).

113. A. Chacinska, C. M. Koehler, D. Milenkovic, T. Lithgow, N. Pfanner, Importing mitochondrial proteins: Machineries and mechanisms. *Cell* **138**, 628–644 (2009).

114. C. A. Wurm, D. Neumann, M. A. Lauterbach, B. Harke, A. Egner, S. W. Hell, S. Jakobs, Nanoscale distribution of mitochondrial import receptor Tom20 is adjusted to cellular conditions and exhibits an inner-cellular gradient. *Proc. Natl. Acad. Sci. U.S.A.* **108**, 13546–13551 (2011).

115. X. Wang, H. H. Gerdes, Transfer of mitochondria via tunneling nanotubes rescues apoptotic PC12 cells. *Cell Death Differ.* **22**, 1181–1191 (2015).

116. J. Pasquier, B. S. Guerrouahen, H. al Thawadi, P. Ghiabi, M. Maleki, N. Abu-Kaoud, A. Jacob, M. Mirshahi, L. Galas, S. Rafii, F. le Foll, A. Rafii, Preferential transfer of mitochondria from endothelial to cancer cells through tunneling nanotubes modulates chemoresistance. *J. Transl. Med.* **11**, 94 (2013).

117. C. Roehlecke, M. H. H. Schmidt, Tunneling nanotubes and tumor microtubes in cancer. *Cancers* **12**, 857 (2020).

Valdes *et al.*, *Sci. Transl. Med.* **16**, eabo0049 (2024)   31 January 2024

16 of 17

118. L. Wang, X. Wang, C. C. Wang, Protein disulfide-isomerase, a folding catalyst and a redox-regulated chaperone. *Free Radic. Biol. Med.* **83**, 305–313 (2015).

119. S. Xu, S. Sankar, N. Neamati, Protein disulfide isomerase: A promising target for cancer therapy. *Drug Discov. Today* **19**, 222–240 (2014).

120. K. L. Ligon, J. A. Alberta, A. T. Kho, J. Weiss, M. R. Kwaan, C. L. Nutt, D. N. Louis, C. D. Stiles, D. H. Rowitch, The oligodendroglial lineage marker OLIG2 is universally expressed in diffuse gliomas. *J. Neuropathol. Exp. Neurol.* **63**, 499–509 (2004).

121. K. Ishizawa, T. Komori, S. Shimada, T. Hirose, Olig2 and CD99 are useful negative markers for the diagnosis of brain tumors. *Clin. Neuropathol.* **27**, 118–128 (2008).

122. S. Camelo-Piragua, M. Jansen, A. Ganguly, J. C. M. Kim, D. N. Louis, C. L. Nutt, Mutant IDH1-specific immunohistochemistry distinguishes diffuse astrocytoma from astrocytosis. *Acta Neuropathol.* **119**, 509–511 (2010).

123. D. N. Louis, A. Perry, G. Reifenberger, A. von Deimling, D. Figarella-Branger, W. K. Cavenee, H. Ohgaki, O. D. Wiestler, P. Kleihues, D. W. Ellison, The 2016 World Health Organization classification of tumors of the central nervous system: A summary. *Acta Neuropathol.* **131**, 803–820 (2016).

124. D. E. Reuss, F. Sahm, D. Schrimpf, B. Wiestler, D. Capper, C. Koelsche, L. Schweizer, A. Korshunov, D. T. W. Jones, V. Hovestadt, M. Mittelbronn, J. Schittenhelm, C. Herold-Mende, A. Unterberg, M. Platten, M. Weller, W. Wick, S. M. Pfister, A. von Deimling, ATRX and IDH-R132H immunohistochemistry with subsequent copy number analysis and IDH sequencing as a basis for an "integrated" diagnostic approach for adult astrocytoma, oligodendroglioma and glioblastoma. *Acta Neuropathol.* **129**, 133–146 (2015).

125. C. Koschmann, A.-A. Calinescu, F. J. Nunez, A. Mackay, J. Fazal-Salom, D. Thomas, F. Mendez, N. Kamran, M. Dzaman, L. Mulpuri, J. Krasinkiewicz, R. Doherty, R. Lemons, J. A. Brosnan-Cashman, Y. Li, S. Roh, L. Zhao, H. Appelman, D. Ferguson, V. Gorbunova, A. Meeker, C. Jones, P. R. Lowenstein, M. G. Castro, ATRX loss promotes tumor growth and impairs nonhomologous end joining DNA repair in glioma. *Sci. Transl. Med.* **8**, 328ra328 (2016).

126. J. M. Boggs, Myelin basic protein: A multifunctional protein. *Cell. Mol. Life Sci.* **63**, 1945–1961 (2006).

127. R. C. Roberts, J. K. Roche, R. E. McCullumsmith, Localization of excitatory amino acid transporters EAAT1 and EAAT2 in human postmortem cortex: A light and electron microscopic study. *Neuroscience* **277**, 522–540 (2014).

128. C. D. Katsetos, M. M. Herman, S. J. Mork, Class III beta-tubulin in human development and cancer. *Cell Motil. Cytoskeleton* **55**, 77–96 (2003).

129. E. Draberova, Z. Lukas, D. Ivanyi, V. Viklicky, P. Draber, Expression of class III beta-tubulin in normal and neoplastic human tissues. *Histochem. Cell Biol.* **109**, 231–239 (1998).

130. J. Q. Trojanowski, V. M. Lee, W. W. Schlaepfer, An immunohistochemical study of human central and peripheral nervous system tumors, using monoclonal antibodies against neurofilaments and glial filaments. *Hum. Pathol.* **15**, 248–257 (1984).

131. T. Wierzba-Bobrowicz, B. Schmidt-Sidor, E. Gwiazda, E. Bertrand, The significance of immunocytochemical markers, synaptophysin and neurofilaments in diagnosis of ganglioglioma. *Folia Neuropathol.* **37**, 157–161 (1999).

132. D. Davydova, C. Marini, C. King, J. Klueva, F. Bischof, S. Romorini, C. Montenegro-Venegas, M. Heine, R. Schneider, M. S. Schröder, W. D. Altrock, C. Henneberger, D. A. Rusakov, E. D. Gundelfinger, A. Fejtova, Bassoon specifically controls presynaptic P/Q-type Ca(2+) channels via RIM-binding protein. *Neuron* **82**, 181–194 (2014).

133. E. Kim, M. Sheng, PDZ domain proteins of synapses. *Nat. Rev. Neurosci.* **5**, 771–781 (2004).

134. C. J. Choong, T. Mochizuki, Neuropathology of α-synuclein in Parkinson's disease. *Neuropathology* **42**, 93–103 (2022).

135. K. Wakabayashi, S. Hayashi, M. Yoshimoto, H. Kudo, H. Takahashi, NACP/alpha-synuclein-positive filamentous inclusions in astrocytes and oligodendrocytes of Parkinson's disease brains. *Acta Neuropathol.* **99**, 14–20 (2000).

136. D. W. Dickson, Neuropathology of Parkinson disease. *Parkinsonism Relat. Disord.* **46**, S30–S33 (2018).

137. M. Goedert, R. Jakes, M. G. Spillantini, The synucleinopathies: Twenty years on. *J. Parkinsons Dis.* **7**, S51–S69 (2017).

138. G. K. Tofaris, P. Garcia Reitböck, T. Humby, S. L. Lambourne, M. O'Connell, B. Ghetti, H. Gossage, P. C. Emson, L. S. Wilkinson, M. Goedert, M. Grazia Spillantini, Pathological changes in dopaminergic nerve cells of the substantia nigra and olfactory bulb in mice transgenic for truncated human alpha-synuclein(1-120): Implications for Lewy body disorders. *J. Neurosci.* **26**, 3942–3950 (2006).

139. H. D. E. Booth, W. D. Hirst, R. Wade-Martins, The role of astrocyte dysfunction in Parkinson's Disease pathogenesis. *Trends Neurosci.* **40**, 358–370 (2017).

140. B. Sonustun, M. F. Altay, C. Strand, K. Ebanks, G. Hondhamuni, T. T. Warner, H. A. Lashuel, R. Bandopadhyay, Pathological relevance of post-translationally modified alpha-synuclein (pSer87, pSer129, nTyr39) in idiopathic Parkinson's disease and multiple system atrophy. *Cell* **11**, 906 (2022).

141. E. Hohenester, P. D. Yurchenco, Laminins in basement membrane assembly. *Cell Adh. Migr.* **7**, 56–63 (2013).

142. D. Florian, H. Kock, K. Plankensteiner, M. Glavanovics, Auto focus and image registration techniques for infrared imaging of microelectronic devices. *Meas. Sci. Technol.* **24**, 074020 (2013).

143. C. Stringer, T. Wang, M. Michaelos, M. Pachitariu, Cellpose: A generalist algorithm for cellular segmentation. *Nat. Methods* **18**, 100–106 (2021).

144. N. Otsu, A Threshold Selection Method from Gray-Level Histograms. *IEEE Trans. Syst. Man Cybern.* **9**, 62–66 (1979).

Science Translational Medicine

Supplementary Materials for

Improved immunostaining of nanostructures and cells in human brain specimens through expansion-mediated protein decrowding

Pablo A. Valdes *et al.*

Corresponding author: E. Antonio Chiocca, eachiocca@bwh.harvard.edu; Edward S. Boyden, edboyden@mit.edu

The PDF file includes:

Materials and Methods
Step-by-step protocol
Figs. S1 to S15
Legends for movies S1 and S2
Tables S1 and S2
References (*108–144*)

Other Supplementary Material for this manuscript includes the following:

Movies S1 to S2
Data file S1
MDAR Reproducibility Checklist

Supplementary Methods

<u>Tissue processing methods</u>

Collagenase treatment

For FFPE 5- µm thick samples of human high-grade glioma brain tumor tissues with high degree of extracellular matrix underwent format conversion and pre-expansion immunostaining (**Fig. S4A**), followed by anchoring and gelation (**Fig. S4B**). After gelation, all coverslips were gently removed from the glass slide that carried the gelled tissue. Excessive gels around the tissue sample were trimmed away using a razor blade. Tissues that were designated for the collagenase treatment (**Fig. S4C**) were submerged in collagenase type II (Thermo Fisher Scientific, #17101015) at 1500 U/ml in Hank's balanced salt solution (HBSS) for 3 hr at 37°C. Next, the collagenases were inactivated by incubating the sample in the softening buffer for 15 min at room temperature (RT) (**Fig. S4C**). Then, tissues were incubated in fresh softening buffer and underwent subsequent softening steps (**Fig. S4D**) and expansion without post-expansion immunostaining (**Fig. S4E**).

Antibody stripping and restaining

To enable highly multiplexed imaging, sequential rounds of antibody stripping and post-decrowding staining were performed. For antibody stripping on tissues stained at the post-decrowding state, we incubated tissues in the softening buffer for 2 hr at 70°C. Afterwards, we washed the tissues 5 times with 1x PBS at RT for 3 min each (**Fig. S1F**). At this stage, tissues had an expansion factor of ~2.3x. Samples were then expanded and imaged (**Fig. S11C**) or subsequently immunostained with only secondary antibodies (**Fig. S11D**) or both primary and secondary antibodies (**Fig. S11H,J; S12**).

Format conversation, antigen retrieval, pre-expansion NHS ester staining and pre-expansion immunostaining

Tissues designated for 3,3'-diaminobenzidine (DAB) chromogenic staining, first underwent format conversion antigen retrieval, immunostaining with primary antibody overnight at 4C, and washing with 1x PBS for 5 minutes. Next, endogenous peroxidase activity was blocked using BLOXALL solution (Vector Labs, #SP-6000) for 10 minutes and washing with 1x PBS for 5 minutes, before

the sample was incubated with biotinylated secondary antibody for 30 minutes at room temperature followed by washing with 1x PBS for 5 minutes. Then, we prepared the VECTASTAIN ABC reagent (Vector labs, #PK-4000) by adding 2 drops (100ul) of reagent A and two drops (100 μl) of reagent B to 10 ml of 1xPBS buffer. The VECTASTAIN reagent was mixed well and allowed to stand for 30 minutes at room temperature. The VECTASTAIN reagent was added to the sample and incubated for 30 minutes at room temperature followed by washing in 1x PBS for 5 minutes. The working solution of DAB was prepared by adding 1 drop (~30 μl) of ImmPACT DAB reagent to 1ml of ImmPACT DAB (Vector Labs, #SK4103) diluent and mixed thoroughly. The substrate solution was added to the slide and incubated for 2-10 minutes until the brown staining from DAB visibly developed and was then washed for 5 minutes in water. Counterstaining was performed using Hematoxylin for 2 minutes and washed again with water for 5 minutes. Finally, the antifade solution was added to cover the sample and sealed with a No. 1 coverslip prior to imaging.

Following format conversion, tissue samples designated for pre-expansion NHS ester staining, were incubated in Alexa Fluor 647 succinimidyl ester (Thermoscientific, #A20006) at a concentration of 0.02 mg/ml in 1x PBS with 0.5% Triton-X, at 4°C for 12 hrs. All pre-expansion stained tissues were immersed in VectaShield mounting media (Vector Laboratories, #H-1000-10) and covered with a No. 1 coverslip prior to imaging (**Fig. 2A,B; 3A-C,L; 4A,G,M,S; 5A,B; 7A; S5A,B; S6A-C**).

Image processing methods

Distortion quantification

We quantified sample distortion based on the same analysis employed in other ExM publications (*4, 15, 19, 34, 35*), using the custom algorithm developed in MATLAB. In this analysis, we performed B-spline-based non-rigid registration between a pair of images to derive a distortion vector field.   We then computed the root-mean-square (RMS) errors on feature measurements in the vector field. This analysis was performed on registrations from pre-expansion and post-expansion images (**Fig. 2E, F; Fig. S5E; S11K**).

Image registration between pre-expansion and post-expansion images

To register a post-expansion image to a given pre-expansion image of the same sample, we first took the entire post-expansion image stack (which thus contained the axial plane corresponding to the entirety of the pre-expansion image), and computed a stack of sum-intensity z-projection images, each of which was a sum of 4 consecutive images in the z-stack (and this moving window of 4 images ran through the entire raw stack, by increments of 1 image in the raw stack; for example, z-projection image #1 was made from raw images #1 - #4, z-projection image #2 was from raw images #2 - #5, and so forth). This procedure ensured that each post-expansion z-projection image covered a similar optical section in biological units given the 4-fold linear expansion of the post-expansion sample. Then, we searched within the stack of post-expansion images (acquired through the entire depth of the tissue sample), for the post-expansion z-projection image that corresponded best to the axial plane of the selected pre-expansion image; by applying a scale-invariant feature transform (SIFT) algorithm followed by random-sample-consensus (RANSAC) with a published, open-source MATLAB package (*142*), which registered the pre-expansion image to every post-expansion z-projection image based on program-generated features on these images, and identified the post-expansion z-projection image with the greatest number of matching features. Afterwards, we performed a rigid transformation to rigidly register the pre-expansion image and the post-expansion z-projection image that had the greatest number of matching features (**Fig. 2A,C and B,D; 3A-C and E-G; 3L,M; 4A,B and G,H and M, N and S,T; 5A,C and B,D; 6A,B; Fig. S5A,C; S6A-C and E-G; S7A-C and E-G; S10A,B**).

Image registration between post-expansion images and post-decrowding ~4x expanded Images

To register a post-decrowding image to a given post-expansion image of the same sample, we first took the entire post-decrowding image stack which thus contained the axial plane corresponding to the entirety of the pre-expansion image), and computed a stack of sum-intensity z-projection images, each of which was a sum of 4 consecutive images in the z-stack (and this moving window of 4 images rans through the entire raw stack, by increments of 1 image in the raw stack; for example, z-projection image #1 was made from raw images #1 - #4, z-projection image #2 was from raw images #2 - #5, and so forth). This procedure ensured that each post-decrowding z-projection image covered a similar optical section compared to a given post-expansion z-projection image. Then, we searched within the stack of post-decrowding images (acquired through the entire depth of the tissue sample), for the post-decrowding z-projection

image that corresponded best to the axial plane of the matched post-expansion z-projection image; by applying a SIFT-RANSAC algorithm, which identified the post-decrowding z-projection image with the greatest number of matching features to the matched post-expansion z-projection image above. Afterwards, we performed a rigid transformation to rigidly register the matched post-expansion z-projection image and the matched post-decrowding z-projection image (**Fig. 3E-G and I-K; 4B,C and H,I and N,O and T,U; 5C,E and D,F; 6C,D**).

To register other images which were only in ~4x-expanded states, (**Fig. S11A-D, H, J; S12**) we first selected a sum-intensity z-projection image centered at approximately the mid-z-axial plane image of an image stack, which we assigned as the initial state z-projection image (see **Fig. S11A**, in which the post-expansion (not stained) z-projection image was the initial state image). Then, each of the subsequent state image stacks (the stacks following after the initial state) was individually registered to the image at the initial state using the workflow from above to find the z-projection image with the greatest number of matching features to the initial z-projection image using DAPI (DAPI not shown) (see **Fig. S11B-D,** in which post-expansion (stained, stripped x2 hrs, or 2ry antibody only stained) z-projection images were the subsequent state images after the initial state). All registrations were performed as described above: first by applying the SIFT-RANSAC algorithm to identify the corresponding z-projection image from the subsequent stack with the highest number of matching features, and then by performing a rigid transformation to rigidly register the subsequent state z-projection images to the initial state z-projection image.

Image Registration between Pre-expansion, Pre-decrowding, Post-decrowding 1x state and ~4x Expanded Images

To register the five images in **Fig. 7A-E**,, which were at either the pre-expansion, shrunken or ~4x-expanded states, we performed rigid registrations in the following order using the SIFT-RANSAC algorithm described above: the ~4x-expanded pre-decrowding-staining z-projection image (**Fig. 9C**) was registered to the pre-expansion single z-slice image (**Fig. 7A**); the pre-decrowding-staining shrunken state single slice image (**Fig. 7B**) was registered to the registered ~4x-expanded pre-decrowding-staining z-projection image (**Fig. 7C**); the ~4x-expanded post-decrowding-staining image (**Fig. 7E**) was registered to the ~4x-expanded pre-decrowding-staining z-projection image (**Fig. 7C**); and then the post-decrowding-staining shrunken state image (**Fig. 7D**) was registered to the ~4x-expanded post-decrowding-staining z-projection image (**Fig. 7E**).

Quantification of Lipofuscin Autofluorescence Removal

To quantify the autofluorescence intensity of lipofuscin between the pre-expansion (not stained) state (**Fig. 3A-C; Supp. Fig. 6A-C**) and the post-expansion (not stained) state (**Fig. 3E-G; Fig. S6E-G**), we generated masks, and quantified fluorescence after applying them to selected ROIs.

Generation of masks: Autofluorescence from lipofuscin was regarded as the signal in this analysis. Since the autofluorescence was observed in all 3 fluorescent channels imaged (**Fig. 3A-C; Fig. S6A-C**), we used the 488 nm excitation (abbreviated as "ex")/525 nm emission (abbreviated as "em") channel (**Fig. 3A; Fig. S6A**) as a representative channel and performed segmentation of the lipofuscin aggregates in images from that channel.   Pre-expansion images of the 488ex/525em channel were segmented into signal-positive regions (whose pixels were assigned to the signal mask) and signal-negative regions (all other pixels, which were assigned to the background mask), by manually setting a threshold intensity value, such that the regions whose intensity values were greater than the threshold (thus with sufficiently bright autofluorescence) completely covered the lipofuscin aggregates, by manual inspection. All pixels whose values were greater than the threshold were assigned to the signal mask, and all others were assigned to the background mask.

Selection of regions of interest (ROIs) and fluorescence quantification: For each of the reported mean fluorescence intensities (**Fig. 3D, H; Fig. S6D, H**), we selected 5 signal and 3 background ROIs per field of view. We imaged 3 fields of view for each sample. We evaluated 3 tissue samples each from a different patient. For each signal ROI, the reported fluorescence intensity was computed from the mean fluorescence intensity value across the entire signal ROI, in either the pre-expansion images (**Fig. 3D; Fig. S6D**) or the post-expansion images (**Fig. 3H; Fig. S6H**). ROIs have a dimension of 5x5 pixels (corresponds to 0.2 microns in biological units). The signal and background ROIs were selected based on the following criteria:

Lipofuscin and Background (**Fig. 3E-G; Fig S6E-G**)
    Signal ROIs
    - Lipofuscin-positive ROI, in normal cortex tissue: ROIs that fit entirely within the lipofuscin-signal mask

Background ROIs

-   Background ROI, in normal cortex tissue: ROIs that fit entirely within the background mask that were at least one ROI width away from the pixels that were positive for the lipofuscin-signal mask.

Mean Fluorescence Intensity Calculations

-   We calculated the mean fluorescence intensities in the 488ex/525em channel (**Fig. 3D, H**; **Fig. S6D, H**; cyan), 561ex/607em channel (**Fig. 3D, H**; **Fig. S6D, H**; yellow), and 640ex/685em channel (**Fig. 3D**, **H**; **Supp. Fig. 6D, H**; magenta) for the lipofuscin-positive ROIs (**Fig. 3D**, **H**; **Fig. S6D, H**; left) and background ROIs (**Fig. 3D**, **H**; **Fig. S6D, H**; right), respectively, in both the pre-expansion (**Fig. 3D; SFig. 6D**) and post-expansion images (**Fig. 3H; Fig. S6H**).

Statistical analysis: We averaged the mean fluorescence value of all 5 signal (and of all 3 background) ROIs in each field of view and given 4 samples and 3 field of view per sample, a total of 12 mean signal and 12 mean background fluorescence intensity values for the lipofuscin-positive signal and background ROIs for each channel in the pre-expansion (**Fig. 3D; Fig. S6D**) and post-expansion (**Fig. 3H; SFig. 6H**) images. Box plot: individual values (open circles), median (middle line), mean (dotted line), first and third quartiles (lower and upper box boundaries), lower and upper raw values (whiskers). We then applied a 2-tailed paired t-test (non-Bonferroni corrected) to lipofuscin vs. background, for pre-expansion mean fluorescence intensities for each spectral channel and also separately for post-expansion mean fluorescence intensities for each spectral channel, with $p < 0.05$ considered statistically significant.

Fluorescence quantification for protein decrowding

To quantify post-decrowding staining, pixel intensity values were compared between post-expansion (not restained) (**Fig. 4B, H, N, T)** and post-expansion (restained) images (**Fig. 4C, I, O, U**), as expansion factor strongly affects pixel intensity values. Quantitative analysis was conducted as follows.

Generation of the signal mask: We constructed a binary image "signal" mask, for each stain, that corresponded to positive pixels (above a manually selected threshold; we were not blinded to condition) for a given stain in both pre-expansion and post-expansion staining images. All images

were segmented into signal-positive pixels according to the threshold intensity value for each image. All pixels whose values were greater than the thresholds in both post-expansion (no restained) and post-expansion (restained) images were assigned to the signal mask.

Generation of background mask: Because post-expansion (restained) images revealed additional structures not visible in pre-expansion or post-expansion (not restained) images, we created a second "background" mask for each stain in each of the pre-expansion and post-expansion (restained) images, corresponding to negative pixels that were below the threshold used for the signal mask. Then, a "double negative" background mask was constructed for each stain, corresponding to the pixels that were negative in both the pre-expansion and post expansion (restained) image background masks for that stain.

Selection of regions of interest (ROIs) and fluorescence quantification: For each of the reported mean fluorescence intensities (**Fig. 4D-F; 4J-L; 4P-R; 4V-X**), we evaluated 3 tissue samples, each from a different patient, with 3 fields of view for each sample, and selected 5 signal and 3 background ROIs per field of view. For each signal ROI, the reported fluorescence intensity was computed from the mean fluorescence intensity value across the entire signal ROI, in either the post-expansion (not restained) staining images (**Fig. 4B, H, N, T**) or the post-expansion (restained) images (**Fig. 4C, I, O, U**), which were both ~4x-expanded sample states. ROIs corresponded to 0.2 microns in biological units (or 5x5 pixels). The signal and background ROIs were selected based on the following criteria, manually selected, without blinding to condition:

MAP2 and GFAP (**Fig. 4D-F**)
  Signal ROIs
  - MAP2-positive ROIs, in normal hippocampus tissue: ROIs that fit entirely within the MAP2-signal mask (all 25 pixels were signal positive) that were at least one ROI width away from the GFAP-signal mask
  - GFAP-positive ROIs, in normal hippocampus tissue: ROIs that fit entirely within the GFAP-signal mask that were at least one ROI width away from the MAP2-signal mask
  Background, Double Negative ROIs
  - MAP2 and GFAP double negative ROIs, in normal hippocampus tissue: ROIs that fit entirely within the double negative mask that were at least one ROI width away from the pixels that were positive for either the MAP2- or GFAP-signal masks.
  Mean Fluorescence Intensity Calculations

- We calculated the mean fluorescence intensities of MAP2-positive ROIs, in the MAP2 channel (**Fig. 4D**, left, cyan) and in the GFAP channel (**Fig. 4D**, right, magenta) in the post-expansion (not restained, NR) and post-expansion (restained, R) images. Box plot: individual values (open circles), median (middle line), mean (dotted line), first and third quartiles (lower and upper box boundaries), lower and upper raw values (whiskers). We did the same procedure for the GFAP-positive ROIs (**Fig. 4E**) and the double negative ROIs (**Fig. 4F**).

GFAP and α-SMA (**Fig. 4J-L**)

Signal ROIs

- GFAP-positive ROIs, in high-grade glioma tissue: ROIs that fit entirely within the GFAP-signal mask that were at least one ROI width away from the α-SMA-signal mask
- α-SMA-positive ROIs, in high-grade glioma tissue: ROIs that fit entirely within the α-SMA-signal mask that were at least one ROI width away from the GFAP-signal mask

Background, Double Negative ROIs

- GFAP and α-SMA double negative ROIs, in high-grade glioma tissue: ROIs that fit entirely within the double negative mask that were at least one ROI width away from the pixels that were positive for either the GFAP- or α-SMA-signal masks.

Mean Fluorescence Intensity Calculations

- We calculated the mean fluorescence intensities of GFAP-positive ROIs, in the GFAP channel (**Fig. 4J**, left, cyan) and in the α-SMA channel (**Fig. 4J**, right, magenta) in the post-expansion (not restained, NR) and post-expansion (restained, R) images. Box plot: individual values (open circles), median (middle line), mean (dotted line), first and third quartiles (lower and upper box boundaries), lower and upper raw values (whiskers). We did the same procedure for the α-SMA-positive ROIs (**Fig. 4K**) and the double negative ROIs (**Fig. 4L**)

Vimentin and α-SMA (**Fig. 4P-R)**

Signal ROIs

- Vimentin-positive ROIs, in high-grade glioma tissue: ROIs that fit entirely within the vimentin-signal mask that were at least one ROI width away from the α-SMA-signal mask
- α-SMA-positive ROIs, in high-grade glioma tissue: ROIs that fit entirely within the α-SMA-signal mask that appeared to have as low as possible an amount of vimentin, yet as noted in the results, there was a high likelihood, that some vimentin-positive signal pixels were

found in α-SMA ROIs, unlike the methods noted above in which the α-SMA-positive ROIs were at least one ROI width away from the GFAP-signal mask.

Background, Double Negative ROIs

- Vimentin and α-SMA double negative ROIs, in high-grade glioma tissue: ROIs that fit entirely within the double negative mask that were at least one ROI width away from the pixels that were positive for either the vimentin- or α-SMA-signal masks.

Mean Fluorescence Intensity Calculations

- We calculated the mean fluorescence intensities of vimentin-positive ROIs, in the vimentin channel (**Fig. 4P**, left, cyan) and in the α-SMA channel (**Fig. 4P**, right, magenta) in the post-expansion (not restained, NR) and post-expansion (restained, R) images. Box plot: individual values (open circles), median (middle line), mean (dotted line), first and third quartiles (lower and upper box boundaries), lower and upper raw values (whiskers). We did the same procedure for the α-SMA-positive ROIs (**Fig. 4Q**) and the double negative ROIs (**Fig. 4R**)

Iba1 and GFAP (**Fig. 4V-X**)

Signal ROIs

- Iba1-positive ROIs, in low-grade glioma tissue: ROIs that fit entirely within the Iba1-signal mask that were at least one ROI width away from the GFAP-signal mask

- GFAP-positive ROIs, in low-grade glioma tissue: ROIs that fit entirely within the GFAP-signal mask that were at least one ROI width away from the Iba1-signal mask

Background ROIs

- Iba1 and GFAP double negative ROIs, in low-grade glioma tissue: ROIs that fit entirely within the double negative mask that were at least one ROI width away from the pixels that were positive for either the Iba1- or GFAP-signal masks.

Mean Fluorescence Intensity Calculations

- We calculated the mean fluorescence intensities of Iba1-positive ROIs, in the Iba1 channel (**Fig. 4V**, left, cyan) and in the GFAP channel (**Fig. 4V**, right, magenta) in the post-expansion (not restained, NR) and post-expansion (restained, R) images. Box plot: individual values (open circles), median (middle line), mean (dotted line), first and third quartiles (lower and upper box boundaries), lower and upper raw values (whiskers). We did the same procedure for the GFAP-positive ROIs (**Fig. 4W**) and the double negative ROIs (**Fig. 4X**)

Statistical analysis: We averaged the mean fluorescence value of all 5 signal ROIs and all 3 double negative ROIs in each field of view. With 3 samples and 3 fields of view per sample, a total of 9 mean signal fluorescence intensity values for the MAP2-positive signal mask ROIs for pre- and post-decrowding images in the MAP2-channel (**Fig. 4D**, left, cyan) and GFAP-channel (**Fig. 4D**, right, magenta), and 9 mean double negative fluorescence intensity values for the MAP2/GFAP images were calculated. We performed the same calculations for GFAP/α-SMA (**Fig. 4J**), vimentin/α-SMA (**Fig. 4P**), and Iba1/GFAP (**Fig. 4V**). We then applied a 2-tailed paired t-test, (non-Bonferroni corrected) to each post-expansion (not restained) and post-expansion (restained) set of 9 averaged values (**Fig. 4D-F, J-L, P-R, and W-X**), with $p < 0.05$ considered statistically significant.

Quantification of amyloid β Plaque Autofluorescence Removal

To quantify the autofluorescence intensity of amyloid β between the pre-expansion (not stained) state (**Fig. 6A**) and the post-expansion (methoy-x04 stained only) state (**Fig. 6B**), we generated masks, and quantified fluorescence after applying them to selected ROIs.

Generation of masks: Autofluorescence from amyloid β plaques was regarded as the signal in this analysis. Since the autofluorescence was observed in the 488ex/525em fluorescent channel (**Fig. 6A-i**), we used it as a representative channel and performed segmentation of the amyloid β plaques in images from that channel.   Pre-expansion images of the 488ex/525em channel were segmented into signal-positive regions (whose pixels were assigned to the signal mask) and signal-negative regions (all other pixels, which were assigned to the background mask), by manually setting a threshold intensity value, such that the regions whose intensity values were greater than the threshold (thus with sufficiently bright autofluorescence) completely covered the amyloid β aggregates, by manual inspection. All pixels whose values were greater than the threshold were assigned to the signal mask, and all others were assigned to the background mask.

Selection of regions of interest (ROIs) and fluorescence quantification: For each of the reported mean fluorescence intensities, we selected 5 signal and 3 background ROIs per field of view and imaged 3 fields of view for each sample. We evaluated 3 tissue samples, each from a different

patient. For each signal ROI, the reported fluorescence intensity was computed from the mean fluorescence intensity value across the entire signal ROI, in either the pre-expansion images (**Fig. 6A**) or the post-expansion images (**Fig. 6B**). ROIs had a dimension of 15x15 pixels (corresponding to 0.6 microns in biological units). The signal and background ROIs were selected based on the following criteria:

Amyloid β plaques and Background (**Fig. 6A,B**)

Signal ROIs

- Amyloid β-positive ROI, in AD human brain cortex tissue: ROIs that fit entirely within the amyloid β-signal mask

Background ROIs

- Background ROI, in cortex tissue: ROIs that fit entirely within the background mask that were at least one ROI width away from the pixels that were positive for the amyloid β-signal mask.

Mean Fluorescence Intensity Calculations

- We calculated the mean fluorescence intensities in the 488ex/525em channel (**Fig. 6A-ii;6B-iii**; Plaque, left), for the amyloid β-positive ROIs and background ROIs in both the pre-expansion (**Fig. 6A-ii**) and post-expansion images (**Fig. 6B-iii**).

Statistical analysis: We averaged the mean fluorescence value of all 5 signal (and of all 3 background) ROIs in each field of view and given 3 samples and 3 plaques per sample, a total of 9 mean signal and 9 mean background fluorescence intensity values were obtained for the amyloid β-positive signal and background ROIs, respectively, for the 488ex/525em channel in the pre-expansion (**Fig. 6A**) and post-expansion (**Fig. 6B**) images. We then applied a 2-tailed paired t-test to amyloid β plaques vs. background, for pre-expansion mean fluorescence intensities for the 488ex/525em spectral channel, and also separately, for post-expansion mean fluorescence intensities for the 488ex/525em spectral channel, with $p < 0.05$ considered statistically significant.

Quantification of fluorescence co-localization of vimentin, Iba1, and GFAP in in low-grade gliomas

To quantify the co-localization of the markers vimentin, GFAP and Iba1, in the pre-expansion-stained state (**Fig. 7F-H**, gray boxplots) and the post-decrowding staining at shrunken state (**Fig. 7F-H**, white boxplots) images, we performed the following analysis.

Generation of nuclei masks: We constructed a binary image "nuclei" mask, corresponding to pixels positive for nuclei (DAPI) in pre-expansion images. Pre-expansion images were each segmented into nuclei-positive pixels using a publicly-available automated, deep learning based segmentation method called Cellpose (www.cellpose.org)(*143*). Gray scale (DAPI channel) images of DAPI-stained pre-expansion images were uploaded to the Cellpose algorithm, which provided an output of segmented nuclei. From the segmented nuclei, we extracted the edges of each nucleus, as well as the centroid, and calculated the total number of nuclei per pre-expansion image.

Generation of signal mask: We constructed binary image "signal" masks for each stain, corresponding to pixels that were positive for that stain in pre-expansion or post-decrowding stained at shrunken state images. Pre-expansion and post-decrowding staining images for each stain were each segmented into signal-positive pixels using an automated Otsu's segmentation algorithm(*144*) in Matlab to calculate a threshold intensity value for each image. All pixels whose values were greater than the automatically determined threshold in the pre-expansion image were assigned to the pre-expansion signal mask, and all pixels whose values were greater than the automatically determined threshold in the post-decrowding staining image were assigned to the post-decrowding signal mask. We calculated this for each individual stain.

Fluorescence quantification:

Percent of positive pixels
Next, we quantified the percent positive pixels among all pixels in each field of view within each stain (vimentin, V; Iba1, I; GFAP, G), or combination of stains (Iba1 and vimentin, I&V; vimentin and GFAP, V&G; Iba1 and GFAP, I&G) (**Fig. 7F**). First, for each individual stain we counted the number of pixels in the signal mask that were positive for that stain. Then we counted the total number of pixels (positive or not) in the field of view. We then calculated the percent positive pixels for that stain by dividing the number of positive signal pixels by the total number of pixels in the field of view and multiplying by 100. Next, for each combination of stains, we counted the number of pixels that were "double positive" for both stains using the signal masks for each individual stain. We then calculated the percent of "double positive" pixels for that combination of stains by dividing the number of "double positive" signal pixels over the total number of pixels in the field of view and multiplying by 100. We performed this pixel quantification method for the pre-

expansion images (**Fig. 7F,** gray colored bars) and then also for the post-decrowding images (**Fig. 7F,** black colored bars).

Number of positive cells

Next, we quantified the total number of positive cells in each field of view for each stain (vimentin, V; Iba1, I; GFAP, G), or combination of stains (Iba1 and vimentin, I&V; vimentin and GFAP, V&G; Iba1 and GFAP, I&G) (**Fig. 7G**). First, for each individual stain we created an image overlay which consisted of the signal mask for a single stain (such as a vimentin-positive signal mask displayed in white) and of the nuclei mask (which displayed the centroids in red and the nuclei boundary in green).

We observed cell nuclei and considered a nucleus "positive" for a stain when at least 25% of the linear surface of the nuclear boundary (nuclei boundary displayed in green; nuclei centroid displayed in red) was surrounded by positive signal pixels such that the sum of the pixels surrounded the nuclear boundary was at least >25% (displayed in white).

Using manual selection via a graphical user interface, cells were considered "positive" for a stain if >25% of the cell nuclei boundary (nuclei boundary displayed in green; nuclei centroid displayed in red) was in contact or surrounded by the positive signal pixels (displayed in white). To label a cell as positive for a stain, we visually inspected each image overlay and manually selected the nuclei user a graphical user interface. This manual selection was used to calculate the total number of positive cells for each stain (vimentin, V; Iba1, I; GFAP, G) in pre-expansion and post-decrowding images. From the nuclei selected for each individual stain, we then calculated the cells that were "double positive" for each combination of stains (Iba1 and vimentin, I&V; vimentin and GFAP, V&G; Iba1 and GFAP, I&G) (**Fig. 7G**).

Next, with the cells counted above, we could then calculate the percent of positive cells with co-localized staining among all cells that were positive for a single type of stain in the field of view. For example, to calculate the percent of cells that were "double positive" (that co-localized) for GFAP and vimentin (**Fig. 7G**, G&V) among all cells that were positive for GFAP (**Fig. 7G**, G), we divided the number of cells calculated above that were "double positive" for GFAP and vimentin (G&V) by the number of cells positive for GFAP (G) x 100. We performed the same analysis using the number of cells calculate above for the other combinations of stains in **Fig. 7H** (G&V/V; I&V/I; I&V/V; I&G/I; I&G/G)

Statistical analysis: We calculated the positive pixels, "double positive" pixels, or number of positive or "double positive" cells in each field of view, and given 3 samples and 2 fields of view per sample, a total of 6 values for the number of positive pixels, "double positive" pixels, or number of positive or "double positive" cells for each stain (or combination of stains) in the pre- and post-decrowding staining images. Box plot: individual values (open circles), median (middle line), mean (dotted line), first and third quartiles (lower and upper box boundaries), lower and upper raw values (whiskers), used throughout the graphs of this figure. We then applied a 2-tailed paired t-test (non-Bonferroni corrected) for the set of values across all 6 values comparing the pre- and post-decrowding staining images, $p < 0.05$ considered statistically significant.

Quantification of fluorescence signal change with NHS ester staining

To quantify the fluorescent intensity of pre-expansion or post-decrowding NHS ester staining (**Fig. S10A,B**), we performed the following analysis. Post-decrowding NHS ester staining fluorescent intensities were so high, such that to ensure there was no camera saturation, exposure times for image acquisition for post-decrowding NHS ester staining images were less than for pre-expansion images. As such, for each pre-expansion and post-decrowding image pair we calculated an exposure factor by dividing the exposure time for the pre-expansion image by the exposure time for the post-decrowding image.

Selection of ROIs and fluorescence quantification: From the image corresponding to pre-expansion staining ("Pre-expansion staining" in **Fig. S10A**), we selected 15 signal ROIs across 2 fields of view from 3 tissue samples derived from 3 patients (1 sample per patient). ROIs have a dimension of 4.9 microns, or 30x30 pixels, and were selected as regions with relatively high fluorescence intensities for NHS by manual inspection. For each signal ROI, we computed the average intensity value across the entire signal ROI, in the pre-expansion state (NHS stained) and post-expansion (NHS re-stained). The fluorescent intensity for the post-expansion signal ROI was then multiplied by its exposure factor to determine the signal ROI for post-decrowding images. The population statistics of these average intensities were reported in **Fig. S10C**.

Statistical analysis: For the fluorescent intensity measurements, we calculated the average of the 15 ROI measurements in each field of view for each tissue sample to calculate a representative quantity for each field of view for a total of 6 values for pre-expansion and post-decrowding staining images. We pre-grouped the measurements by tissue sample. We then performed a 2-tailed paired t-test analysis between the representative quantities obtained from the pre-expansion staining image and post-decrowding staining image, p< 0.05 considered statistically significant.

Quantification of fluorescence signal change with antibody stripping

To quantify the fluorescent intensity of post-decrowding immunostaining at different stages of the antibody stripping protocol (**Fig. S11A-D**), we performed the following analysis.

Selection of ROIs and fluorescence quantification: For each stain (histone H3, **Fig. S11E; vimentin, Fig. S11F; GFAP, Fig. S11G**), we selected 10 signal ROIs on the post-decrowding-staining images (i.e., **Fig. S11B**, because this is the state where we can clearly identify positive regions for each stain) from each of the 4 tissue samples derived from 2 patients (2 samples per patient), for a total of 40 signal ROIs per stain. ROIs have a dimension of 15x15 pixels (corresponds to 0.6 microns in biological units) and were selected on regions with relatively high fluorescence intensities for each stain, to be rigorous about confronting any residual staining, by manual inspection. For each signal ROI, we computed the average intensity value across the entire signal ROI, in the post-expansion state (not stained), post-expansion (stained), post-expansion states (stripped for 1 hr), post-expansion state (stripped for 2 hrs), and post-expansion (2ry antibody only stained). The population statistics of these average intensities were reported in **Fig. S11E-G** for the three analyzed stains.

Statistical analysis: For the fluorescent intensity measurements, we first group the 40 measurements by their tissue sample (n = 4 samples, with 10 ROIs each), using the average of the 10 measurements in each tissue sample as the representative quantity. We pre-grouped the measurements by tissue sample. We then performed a 2-tailed paired t-test (non-Bonferroni corrected) analysis, between the representative quantities obtained from the post-decrowding-staining image, and images acquired at the other states, p < 0.05 considered statistically significant.

Quantification of fluorescence signal change with multiple rounds of immunostaining

To quantify the fluorescent intensity of post-decrowding immunostaining for vimentin, in consecutive rounds of antibody stripping and re-staining (**Fig. S11I**), we performed the following analysis.

Selection of ROIs and fluorescence quantification: From the image corresponding to the first round of immunostaining ("Round 1" in **Fig. S11H**), we selected 15 signal ROIs across 2 fields of view from 3 tissue samples. ROIs have a dimension of 0.6 microns, or 15x15 pixels, and were selected as regions with relatively high fluorescence intensities for vimentin, by manual inspection. For each signal ROI, we computed the average intensity value across the entire signal ROI, and we did this for each image acquired at each of the four rounds of immunostaining (Rounds 1 and 4 shown in **Fig. S11H**). The population statistics of these average intensities were reported in **Fig. S11I**.

Statistical analysis: For the fluorescent intensity measurements, we calculated the average of the 15 ROI measurements in each field of view for each tissue sample to calculate a representative quantity for each field of view for a total of 6 values for each round. We pre-grouped the measurements by tissue sample. We then performed a 2-tailed paired t-test (non-Bonferroni corrected) analysis between each of the four different rounds of immunostaining, $p < 0.05$ considered statistically significant.

Supplementary Figures

dExPath for multiplexing
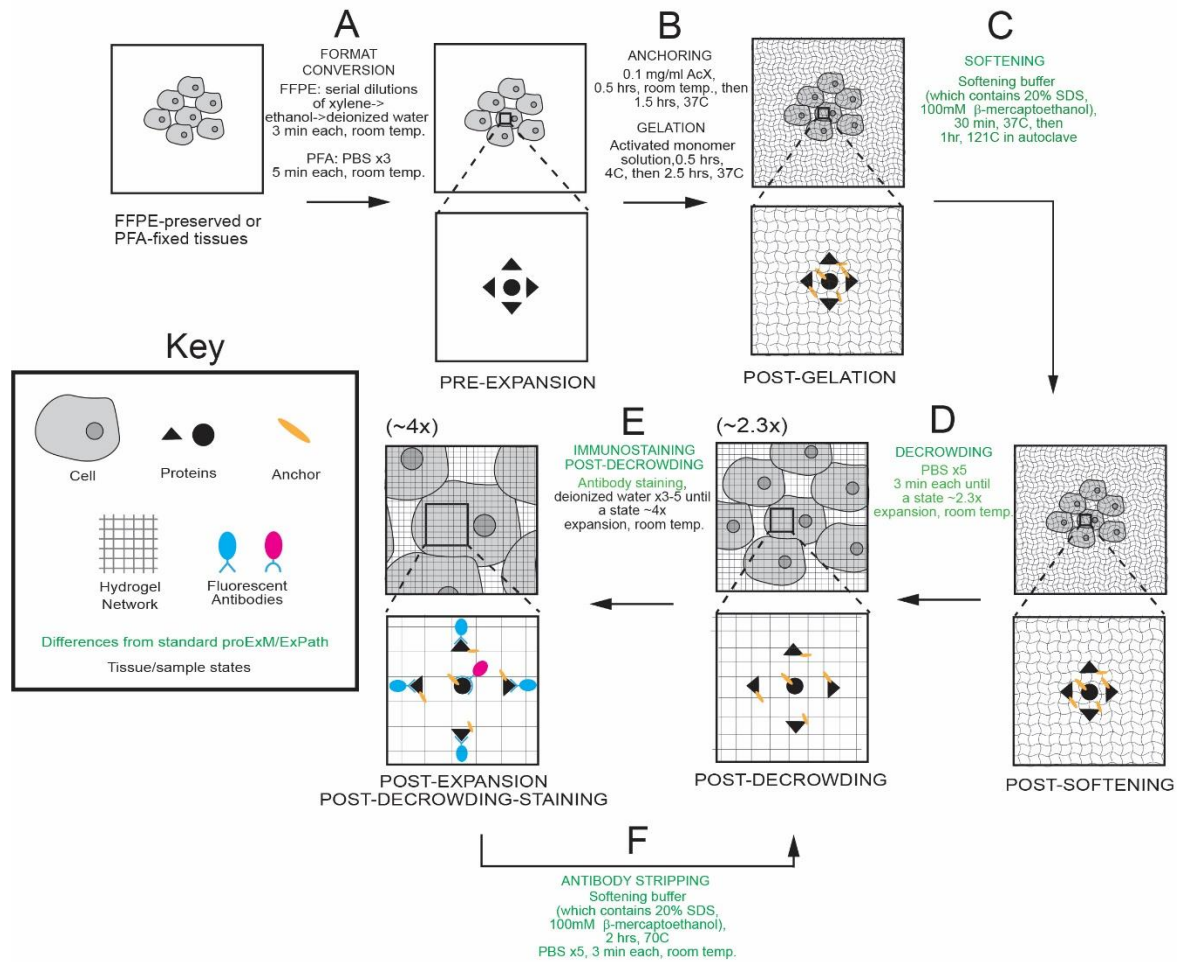
Fig. S1. dExPath for multiplexed post-expansion immunostaining of formaldehyde-fixed specimens. (A-E) Workflow for expanding FFPE (formalin-fixed paraffin-embedded), or formaldehyde-fixed, human (or mouse) brain specimens, enabling multiple rounds of sequential post-decrowding immunostaining. Key modifications of published proExM and ExPath protocols are shown in green. PFA, paraformaldehyde; PBS, phosphate buffered saline; AcX, Acryloyl-X; SDS, sodium dodecyl sulfate. For steps after decrowding (D), linear expansion factor of the hydrogel-specimen composite is shown in parentheses above the schematic of the step. (A) Tissue samples undergo conversion into a state compatible with expansion. (B) Tissue samples are treated so that gel-anchorable groups are attached to proteins, then the sample is permeated with an expandable polyacrylate hydrogel. (C) Samples are incubated in a softening buffer to denature, and loosen disulfide bonds and fixation crosslinks between proteins in the sample. (D) Softened samples are washed in a buffer to partially expand them. (E) Samples are stained and

then expanded fully by immersion in water. (F) Samples undergo repeated rounds of sequential antibody stripping by incubation in softening buffer to remove antibodies, which shrinks the specimen back to 1x, followed by re-expansion to 2.3x, post-decrowding immunostaining and full expansion (E) to enable highly multiplexed imaging.
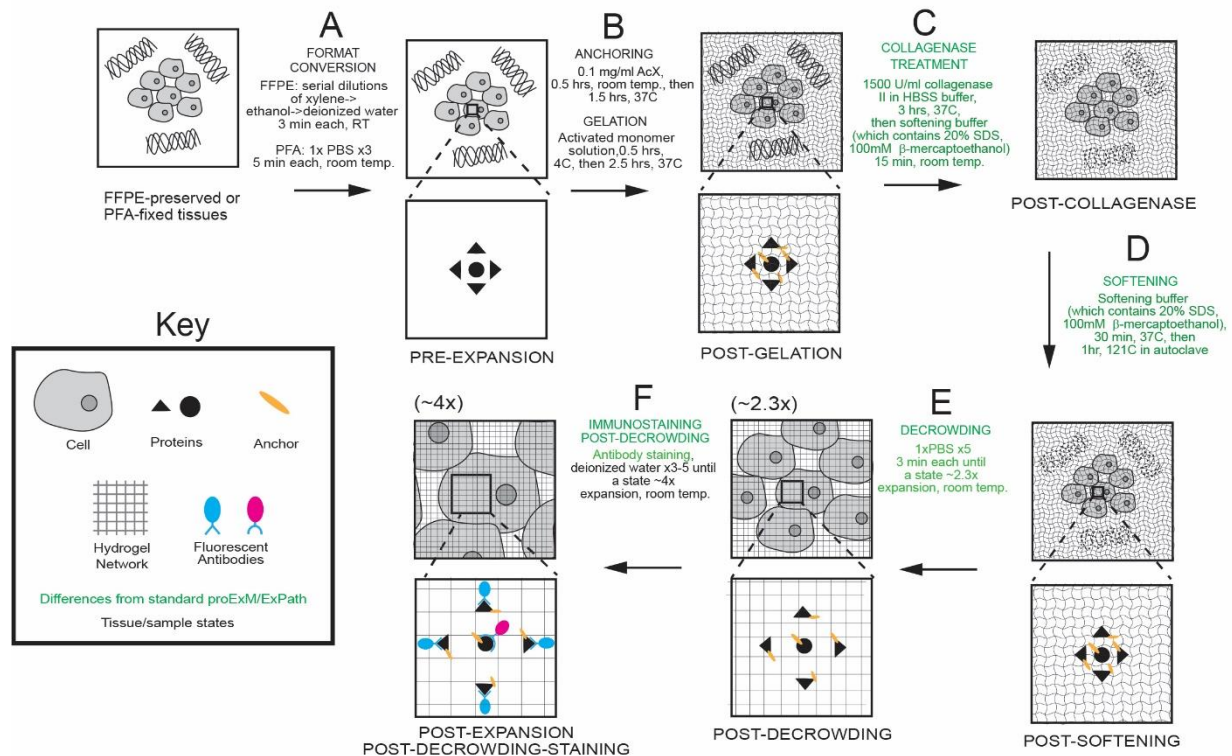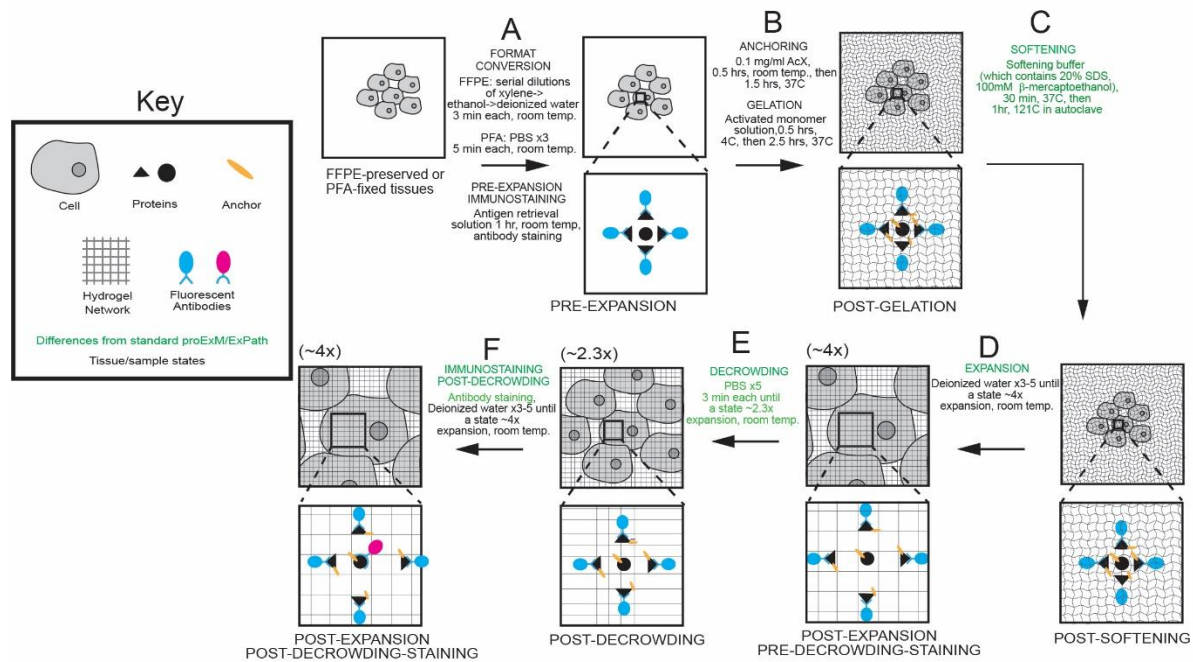
Fig. S2. dExPath for post-expansion immunostaining of formaldehyde-fixed specimens with a high degree of extracellular matrix. (A-F) Workflow for expanding FFPE, or formaldehyde-fixed, human (or mouse) brain specimens, enabling post-decrowding immunostaining in human brain tissues with a high degree of extracellular matrix. HBSS, Hank's balanced salt solution. Key modifications of published proExM and ExPath protocols are shown in green. For steps after decrowding (E), linear expansion factor of the hydrogel-specimen composite is shown in parentheses above the schematic of the step. (A) Tissue samples undergo conversion into a state compatible with expansion. (B) Tissue samples are treated so that gel-anchorable groups are attached to proteins, then the sample is permeated with an expandable polyacrylate hydrogel. (C) Samples are incubated in a buffer containing collagenase. (D) Samples are incubated in a softening buffer to denature, and loosen disulfide bonds and fixation crosslinks between, proteins in the sample. (E) Softened samples are washed in a buffer to partially expand them. (F) Samples are stained and then expanded fully by immersion in water.
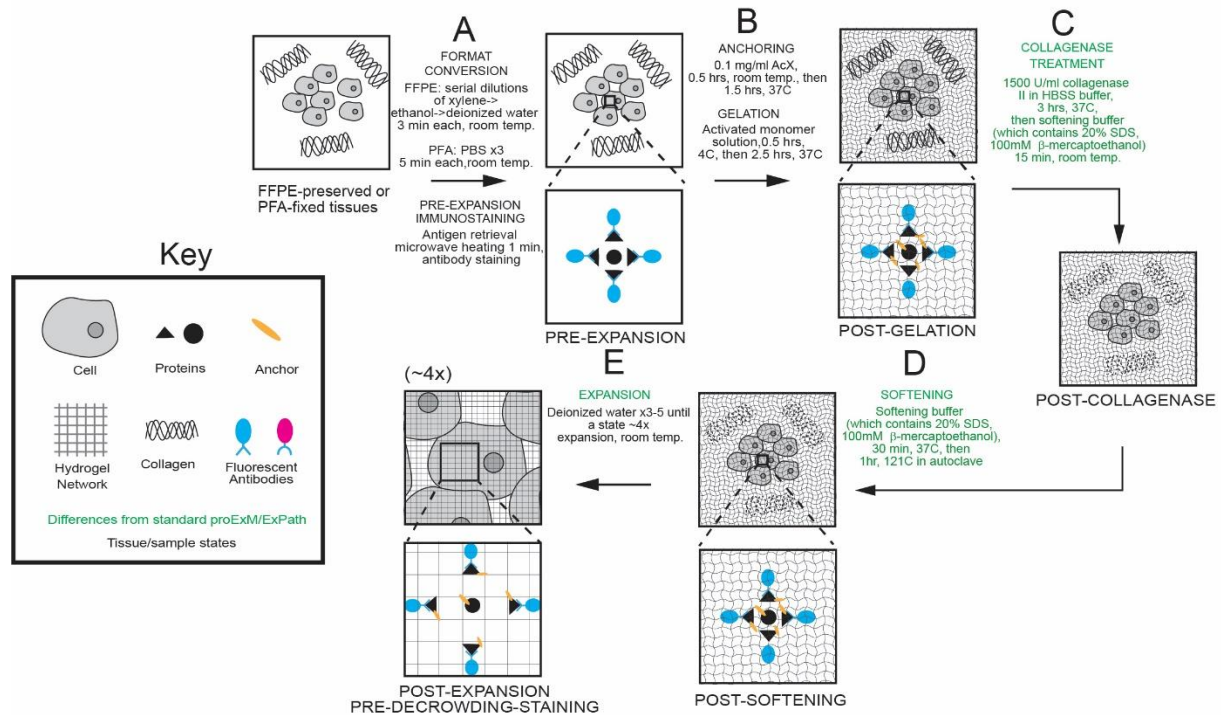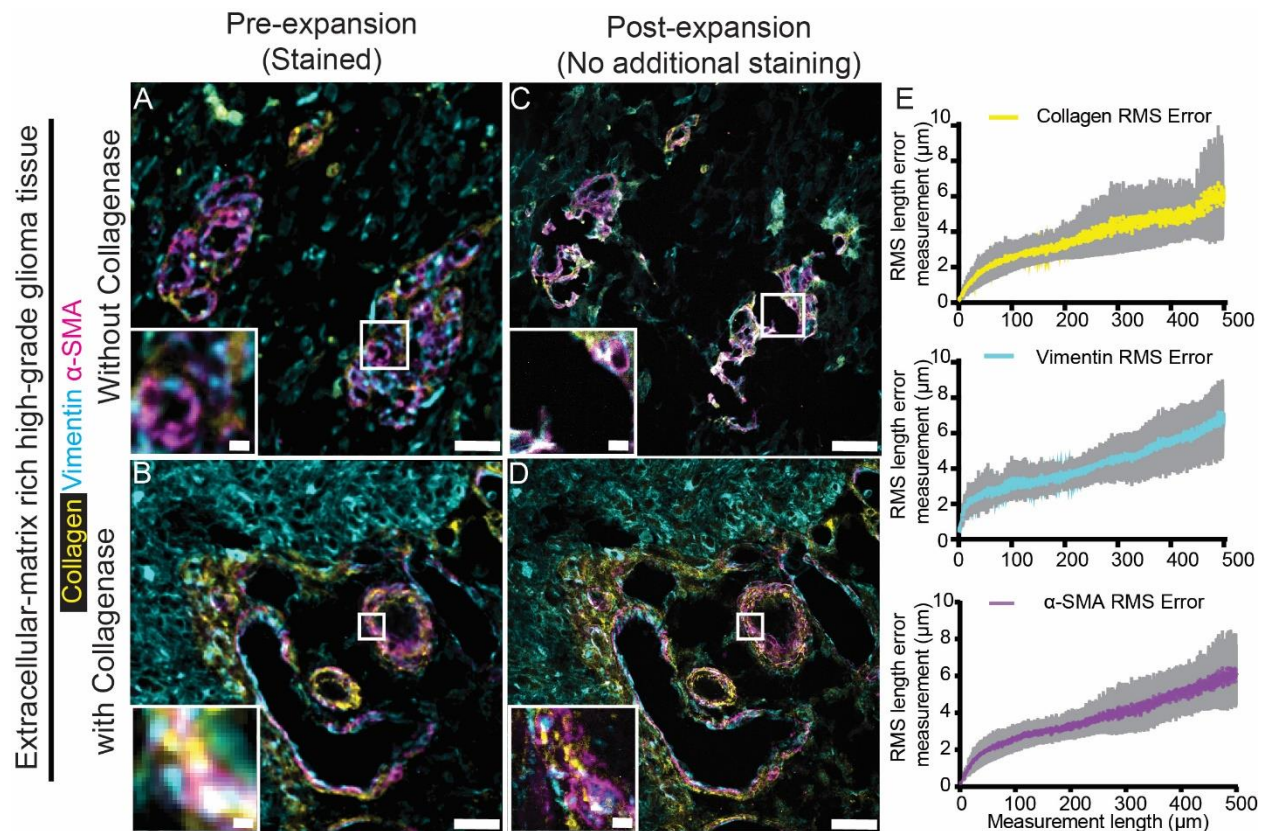
Fig. S3. dExPath for post-expansion immunostaining of formaldehyde-fixed specimens that enables comparison of pre- and post-expansion immunostaining. (A-F) Workflow for expanding FFPE, or formaldehyde-fixed, human (or mouse) brain specimens, enabling comparison of pre- and post-decrowding immunostaining. Key modifications of published proExM and ExPath protocols are shown in green. For steps after expansion (D), linear expansion factor of the hydrogel-specimen composite is shown in parentheses above the schematic of the step. (A) Tissue samples undergo conversion into a state compatible with expansion, followed by antigen retrieval and pre-expansion immunostaining. (B) Tissue samples are treated so that gel-anchorable groups are attached to proteins, then the sample is permeated with an expandable polyacrylate hydrogel. (C) Samples are incubated in a softening buffer to denature, and loosen disulfide bonds and fixation crosslinks between, proteins in the sample. (D) Softened samples are then fully expanded for comparative analysis. (E) Expanded samples are converted into a state similar to the decrowded state (~2.3x) prior to immunostaining. (F) Samples are additionally stained and then expanded fully for comparative analysis.

Fig S4. dExPath of formaldehyde-fixed specimens with a high degree of extracellular matrix that enables comparison of pre- and post-expansion tissues. (A-E) Workflow for expanding FFPE, or formaldehyde-fixed, human (or mouse) brain specimens with a high degree of extracellular matrix, enabling comparison of pre- and post-expansion tissues. Key modifications of published proExM and ExPath protocols are shown in green. Following expansion (E), linear expansion factor of the hydrogel-specimen composite is shown in parentheses above the schematic of the step. (A) Tissue samples undergo conversion into a state compatible with expansion, followed by antigen retrieval and pre-expansion immunostaining. (B) Tissue samples are treated so that gel-anchorable groups are attached to proteins, then the sample is permeated with an expandable polyacrylate hydrogel. (C) Samples are incubated in a buffer containing collagenase. (D) Samples are incubated in a softening buffer to denature, and loosen disulfide bonds and fixation crosslinks between proteins in the sample. (E) Softened samples are then fully expanded for comparative analysis.

Fig. S5. Isotropy of dExPath, with and without collagenase, in human glioma tissues with a high degree of extracellular matrix. (A-B) Representative pre-expansion confocal images of FFPE 5-μm-thick slices of extracellular matrix-rich human high grade-glioma brain tumor tissue (A and B, both n = 3 samples, each from a different patient) which underwent processing as in **Fig. S4A** (tissue deparaffinization, rehydration, antigen retrieval, and immunostaining)), with immunostaining being for collagen, vimentin, and α-SMA, and staining for DAPI (not shown; used for initial rigid alignment). White boxes in (A-B) mark extracellular matrix-rich regions; lower left inset is zoomed-into image of the upper right white box. (C-D) Post-expansion images of the same fields of view as shown in (A-B), respectively. Specifically, samples were treated with anchoring and gelation (as in **Fig. S4B**), and either no collagenase treatment followed by softening (C), or collagenase treatment followed by softening (D) (as in **Fig. S4C-D**), and another round of DAPI staining, ~4x linear expansion (as in **Fig. S4E**), and imaging with confocal microscopy. White boxes in (C-D), as in (A-B). (E) Root mean square (RMS)-length measurement errors obtained by comparing pre- and post-expansion images for collagenase-treated samples, such as shown in B and D (n = 3 samples, each from a different patient). Line, mean; shaded area, standard deviation. All images are single z-

slice confocal images of pre-expansion images (A-B) or sum intensity z-projections of confocal image stacks (C-D), both covering an equivalent tissue depth in biological units. Brightness and contrast settings in images (A-D): first set by the ImageJ auto-scaling function, and then manually adjusted (by raising the minimum-intensity threshold and lowering the maximum-intensity threshold) to improve contrast for stained structures but quantitative analysis in (E) was conducted on raw image data. Scale bars (in biological units): (A-D) outer panel 15 μm; inset, 3 μm. Linear expansion factors: (C-D) 4.0x.
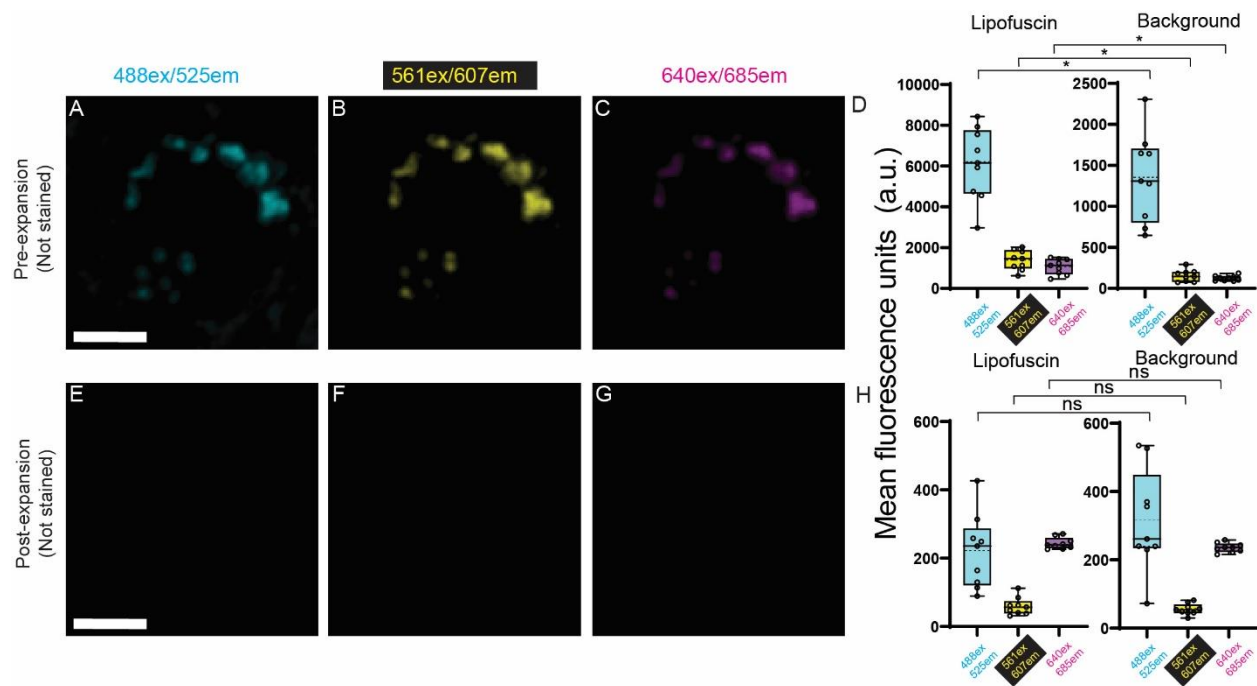
Fig. S6. dExPath removal of lipofuscin autofluorescence to background levels in tissue specimens from older patients. (A-C) Representative (n = 3 samples, each from a different patient) pre-expansion confocal images (single z slices) of a neuron of an FFPE 5-µm-thick sample of AD human cortex (age: all patients were 73 years old). The samples underwent format conversion (as in **Fig. 1A**, tissue deparaffinization and rehydration), and DAPI staining (images not shown in this figure; used for registration across images). Images were acquired for 3 common fluorescent filter settings: (A) 488 nm excitation (abbreviated as "ex") / 525 nm emission (abbreviated as "em") channel; (B) 561ex/607em channel; (C) 640ex/685em channel. (D) Mean fluorescence intensities from pre-expansion images, averaged across regions of interest (ROIs) that exhibited prominent lipofuscin (left bar graph), as well as across background ROIs (right bar graph); colors correspond to the colors of A-C (n = 3 tissue samples, each from a different patient). Brightness and contrast settings in images (A-C): first set using the ImageJ auto-scaling function, then manually adjusted (by raising the minimum-intensity threshold and lowering the maximum-intensity threshold) to improve contrast for lipofuscin; quantitative analysis in (D) was conducted on raw image data . Box plot: individual values (open circles; 3 measurements were acquired from each patient), median (middle line), mean (dotted line), first and third quartiles (lower and upper box boundaries), lower and upper raw values (whiskers).

Statistical testing: 2-tailed paired t-test (non-Bonferroni corrected) was applied to lipofuscin vs. background, for pre-expansion mean fluorescence intensities for each spectral channel. *, $p < 0.05$. (E-G) Post-expansion confocal images after the sample from A-C was additionally treated with anchoring, gelation, digestion, DAPI staining, and ~4x linear expansion following the dExPath protocol. Sum intensity z-projections of image stacks corresponding to the biological thickness of the original slice, taken under identical settings and of the same field of view as A-C and displayed under the same settings. (H) Mean fluorescence intensities, from post-expansion images, averaged across the same lipofuscin (left) and background (right) ROIs used in panel D, for the same samples as panel D. Plots and statistics as in D. Scale bars (in biological units): (A, E) 6 μm; linear expansion factor: (E-G) 4.5x.
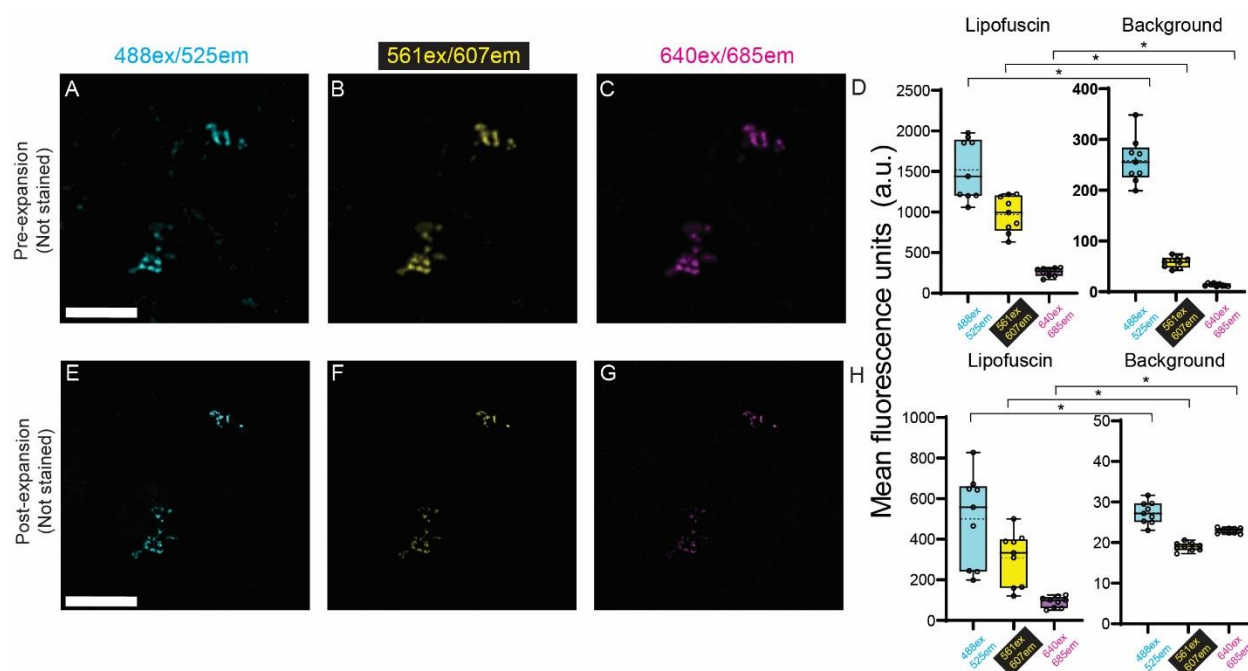
Fig. S7. Classical ExPath does not reduce lipofuscin autofluorescence to background levels. (A-C) Representative (n = 3 samples, each from a different patient) pre-expansion confocal images (single z slices) of a neuron of an FFPE 5-μm-thick sample of normal human cortex. The samples underwent format conversion (as in **Fig. 1A**, tissue deparaffinization and rehydration), and DAPI staining (images not shown in this figure; used for registration across images). Images were acquired for 3 common fluorescent filter settings: (A) 488 nm excitation (abbreviated as "ex") / 525 nm emission (abbreviated as "em") channel; (B) 561ex/607em channel; (C) 640ex/685em channel. (D) Mean fluorescence intensities from pre-expansion images, averaged across regions of interest (ROIs) that exhibited prominent lipofuscin (left bar graph), as well as across background ROIs (right bar graph); colors correspond to the colors of A-C (n = 3 tissue samples, each from a different patient). Brightness and contrast settings in images (A-C): first set by the ImageJ auto-scaling function, and then manually adjusted (by raising the minimum-intensity threshold and lowering the maximum-intensity threshold) to improve contrast for lipofuscin but quantitative analysis in (D) was conducted on raw image data. Box plot: individual values (open circles; 3 measurements were acquired from each patient), median (middle line), mean (dotted line), first and third quartiles (lower and upper box boundaries), 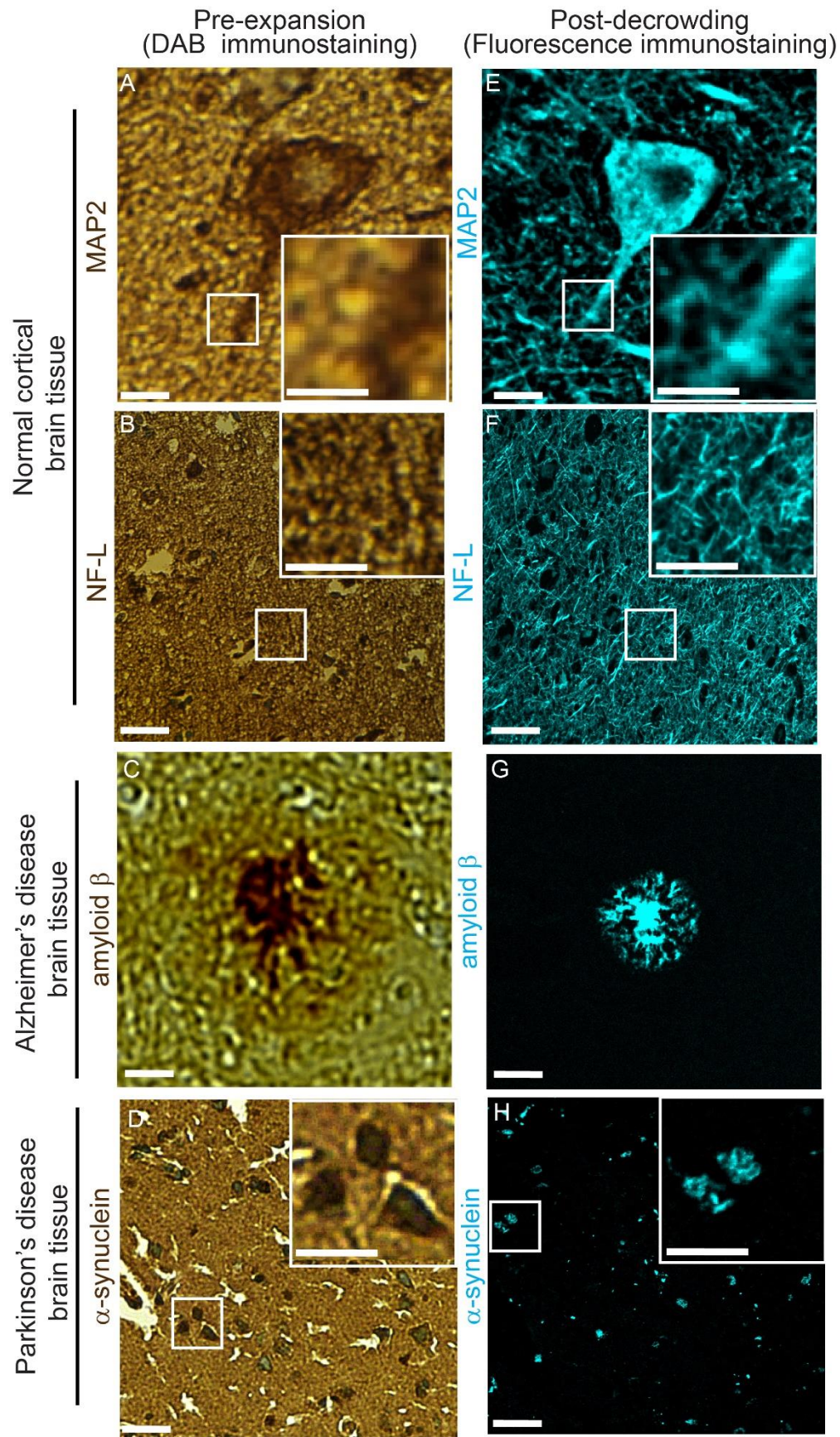lower and upper raw values (whiskers). Statistical testing: 2-tailed paired t-test (non-Bonferroni corrected) was applied to lipofuscin vs. background, for pre-expansion mean

fluorescence intensities for each spectral channel. *, p < 0.05. (E-G) Post-expansion confocal images after the sample from A-C was additionally treated with anchoring, gelation, digestion with proteinase K, DAPI staining, and ~4x linear expansion following the proteinase-based ExPath protocol. Sum intensity z-projections of image stacks correspond to the biological thickness of the original slice, taken under identical settings and of the same field of view as A-C and displayed under the same settings. (H) Mean fluorescence intensities, from post-expansion images, averaged across the same lipofuscin (left) and background (right) ROIs used in panel D, for the same samples as panel D. Plots and statistics as in D. Scale bars (in biological units): (A, E) 7 µm; linear expansion factor: (E-G) 4.4x.

Pre-expansion
(DAB immunostaining)

Post-decrowding
(Fluorescence immunostaining)

Normal cortical brain tissue

MAP2

NF-L

Alzheimer's disease brain tissue

amyloid β

Parkinson's disease brain tissue

α-synuclein

A B C D E F G H

Fig. S8. dExPath post-decrowding immunostaining, compared to standard chromogenic staining. (A-D) Representative pre-expansion brightfield images of FFPE 5-μm-thick slices of normal human cortex (A,B), Alzheimer's disease human cortex (C), and Parkinson's disease human cortex (D), which underwent processing as in **Fig. S3A** (tissue deparaffinization, rehydration, antigen retrieval, and immunostaining), with immunostaining for MAP2 (A), neurofilament light chain (NF-L) (B), amyloid-β (C), or α-synuclein (D) with standard chromogenic staining using 3,3'-diaminobenzidine (DAB). White boxes mark regions shown magnified in insets on the right. (E-G) Post-decrowding images of immediately adjacent sections of those shown in (A-D). Samples underwent format conversion (as in **Fig. 1A**), anchoring and gelation (as in **Fig. 1B**), softening (as in **Fig. 1C**), followed by decrowding (as in **Fig. 1D**), and post-decrowding staining for MAP2 (E), NF-L (F), amyloid-β (G), or α-synuclein (H) (as in **Fig. 1E**), and imaging with confocal microscopy. Scale bars (in physical units): (A) 28 μm; inset, 14 μm; (B) 100 μm; inset, 14 μm; (C) 28 μm; (D) 60 μm; inset, 30 μm; (E) 26 μm; inset, 13 μm; (F) 70 μm; inset, 10 μm (G) 64 μm; (H) 90 μm; inset, 45 μm.
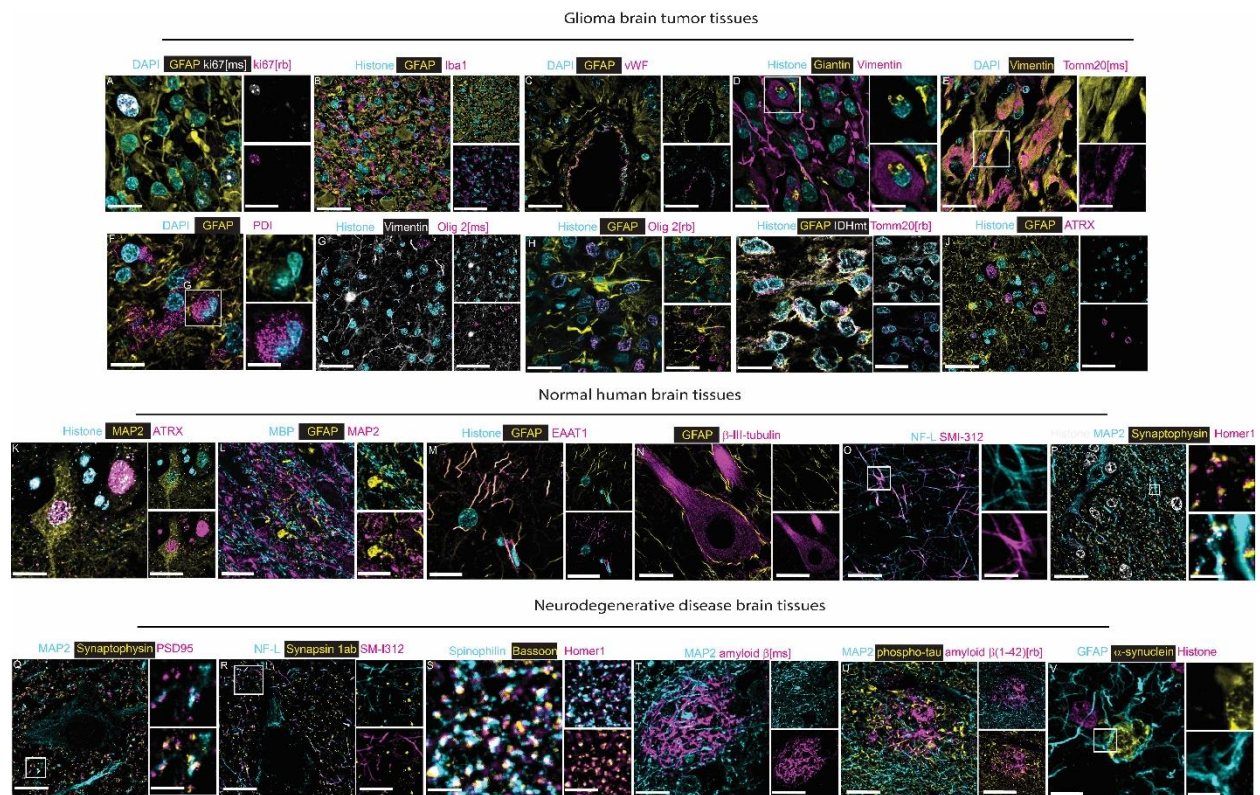
Fig. S9. dExPath is compatible with commonly used antibodies for normal, glioma, Alzheimer's Disease (AD), and Parkinson's Disease (PD) human brain tissues. Confocal images of FFPE 5-μm-thick samples of glioma (**A**-**J**), normal brain (**K** - **S**), AD brain (**T** - **U**) and PD brain (**V**). Samples underwent format conversion (**Fig. 1A**), anchoring, gelation (**Fig. 1B**), softening (**Fig. 1C**), decrowding (**Fig. 1D**), post-decrowding immunostaining, and confocal imaging at ~2.3x or ~4x linear expansion (**Fig. 1E**). The tissue samples were stained for the following: (A) DAPI, GFAP, ki67 [mouse (ms)] and ki67 [rabbit (rb)] (a nuclear protein of proliferating cells). (B) histone H3, GFAP, Iba1 (a microglial protein). (C) DAPI, GFAP, von Willebrand factor (vWF, an endothelial cell protein). (D) histone H3, Giantin (a cis-golgi body protein), and vimentin. (E) DAPI, vimentin, translocase of outer mitochondrial membrane 20 [mAb] (Tomm20, a mitochondrial protein). (F) DAPI, GFAP and protein disulfide isomerase (PDI, an endoplasmic reticulum protein). (G) histone H3, vimentin, oligodendrocyte transcription factor 2 [ms] (Olig2, a glioma protein). (H) histone H3, GFAP, Olig2 [rb]. (I) histone H3, GFAP, isocitrate dehydrogenase mutant (IDHmt, a glioma protein), and Tomm20 [rb]. (J) histone H3, GFAP, and α-thalassemia/mental retardation, X-linked (ATRX, a nuclear protein). (K) histone H3, MAP2, and ATRX. (L) myelin basic protein (MBP), GFAP, and MAP2. (M) histone H3, GFAP, and excitatory amino acid transporter 1 (EAAT1, a glial glutamate transporter protein). (N) GFAP, β-III-tubulin (a

microtubule neuron protein). (O) neurofilament light chain (NF-L, neurofilament protein), and SMI-312 (a pan-axonal marker of neurofilaments). (P) MAP2, synaptophysin (a pre-synaptic protein) and homer1 (a post-synaptic protein). (Q) MAP2, synaptophysin, and post-synaptic density protein 95 (PSD95) (a post-synaptic protein). (R) NF-L, synapsin 1ab (a pre-synaptic protein), and SMI-312. (S) spinophilin (a pre-synaptic protein), bassoon (a pre-synaptic protein) and homer1. (T) MAP2, amyloid β [ms] (an amyloid β plaque marker). (U) MAP2, phospho-tau (a neurofibrillary tangle protein) and amyloid β (1-42) [rb] (an amyloid β plaque marker). (V) GFAP, a-synuclein (a neuronal protein that aggregates in PD), and histone H3. White boxes mark regions shown in insets on the right. Insets on the right with no corresponding white boxes correspond to the complete region shown on the left. All images are sum intensity z-projections of a confocal image stack. Brightness and contrast settings in images (A-V): first set by the ImageJ auto-scaling function, then manually adjusted (by raising the minimum-intensity threshold and lowering the maximum-intensity threshold) to improve contrast of stained structures. Scale bars (in physical units): (A) left panel, 38 μm; inset, 76 μm; (B) left panel, 83 μm; inset, 166 μm; (C) left panel, 83 μm; inset, 166 μm; (D) left panel, 40 μm; inset, 20 μm; (E) left panel, 88 μm; inset, 44 μm; (F) left panel, 40 μm; inset, 22 μm; (G) left panel, 70 μm; inset, 140 μm; (H) left panel, 50 μm; inset, 100 μm; (I) left panel, 55 μm; inset, 110 μm; (J) left panel, 83 μm; inset, 167 μm; (K) left panel, 30 μm; inset, 30 μm; (L) outer panel, 110 μm; inset, 80 μm; (M) left panel, 36 μm; inset, 71 μm; (N) left panel, 75 μm; inset, 150 μm; (O) left panel,40 μm; inset, 12 μm; (P) left panel, 55 μm; inset, 8 μm; (Q) left panel, 45 μm; inset, 12 μm; (R) left panel, 40 μm; inset, 18 μm; (S) left panel, 6 μm; inset, 13 μm; (T) left panel, 33 μm; inset, 65 μm; (U) left panel, 40 μm; inset, 80 μm; (V) left panel, 29 μm; inset, 10 μm.

In more detail: We surveyed a panel of antibodies commonly used by clinical pathology labs to examine the images they would yield, with dExPath. We found that dExPath could produce high quality images with clinical antibodies used by pathology cores in the diagnoses of a broad range of neurologic diseases, including antibodies against histone-H3 (wildtype), ki67, GFAP, Iba1, von Willebrand factor (vWF), vimentin, giantin, translocase of outer mitochondrial membrane 20 (Tomm20), protein disulfide isomerase (PDI), oligodendrocyte transcription factor 2 (Olig2), isocitrate dehydrogenase mutant (IDHmt), α-thalassemia/mental retardation, X-linked (ATRX), myelin basic protein (MBP), excitatory amino acid transporter 1 (EAAT1), β-III-tubulin, neurofilament light chain (NF-L), SMI-312, MAP2, synaptophysin, homer, post-synaptic density protein 95 (PSD95), synapsin 1ab, spinophillin, bassoon, amyloid β (36-43), phospho-tau and amyloid β (1-42) (**Table S2**). Staining the same tissue with two different antibodies for ki67 (mouse monoclonal (ms); rabbit polyclonal (rb)), a nuclear protein of proliferating cells (*108*),

yielded consistent results for both antibodies, with the expected visualization of patterns in glioma tissues (**Fig. S9A**). Staining with GFAP, an astrocyte marker and marker of glial tumors, was observed in glioma tissue with associated dense Iba1 staining of putative microglia (**Fig. S9B**). Staining patterns with von Willebrand factor (vWF), a common endothelial cell marker (*109-111*), were consistent with those of blood vessels (**Fig. S9C**). Vimentin staining, a mesenchymal cell marker used in diagnoses of central nervous system (CNS) tumors (*38, 70, 112, 86*), was observed in cells with perinuclear staining of cis-golgi protein Giantin (*55*) (Fig. S9D). Tomm20 staining was observed along vimentin positive structures in glioma tissues, showing the expected pattern of positivity for mitochondria in tumor tissues (*113, 114*), that of long tubular structures (*115-117*) (**Fig. S9E**). PDI staining was found surrounding cell nuclei, consistent with the expected location of the endoplasmic reticulum (*118, 119*) (**Fig. S9F**). Two different Olig2 antibodies (**Fig. S9G**, monoclonal; **Fig. S9H**, polyclonal) used as glioma markers (*120, 121*) both stained cell nuclei in glioma tissues. IDHmt glioma tissues showed positive staining of putative glioma tumor cells (*122, 123*), with intracellular Tomm20 staining consistent with the location of mitochondria (**Fig. S9I**). ATRX staining was absent in multiple nuclei in diffuse astrocytoma tissue (**Fig. S9J**), an expected finding in diffuse astrocytomas, but was observed in all nuclei in normal brain tissue, as expected (**Fig. S9K**) (*124, 125*). MBP showed staining of putative myelin distinct from GFAP in normal brain tissues (*107, 126*) (**Fig. S9L**). EAAT1, an astrocyte glutamate transporter, stained putative okastrocytes, co-localizing with GFAP staining in normal brain tissues (*127*) (**Fig. S9M**). Staining for GFAP, a protein found in astrocytes, and β-III-tubulin, a microtubule protein found in neurons (*128, 129*), showed no staining overlap (**Fig. S9N**). Staining for NF-L and SMI-312, both markers of neurofilament subunit proteins and useful for diagnosis of neuronal and glioneuronal tumors, showed significant overlap (*37, 130, 131*) (**Fig. S9O**). Pre-synaptic and post-synaptic markers often were localized near each other (*57, 132, 133*) (**Fig. S9P,Q,R,S**). Staining for amyloid β plaques was observed with expected patterns (Fig. S9T) and co-staining for neurofibrillary tangles using phospho-tau showed close spatial association of amyloid β plaques and neurofibrillary tangles (**Fig. S9U**), recapitulating expected histological findings in AD (*81-84*). Staining for α-synuclein showed structures with a globular appearance consistent with Lewy Bodies with a ~10-30 μm diameter found in PD tissues (*134-138*) surrounded by GFAP stained fibrillary structures of putative astrocytes (Fig. S9V) (*139, 140*).
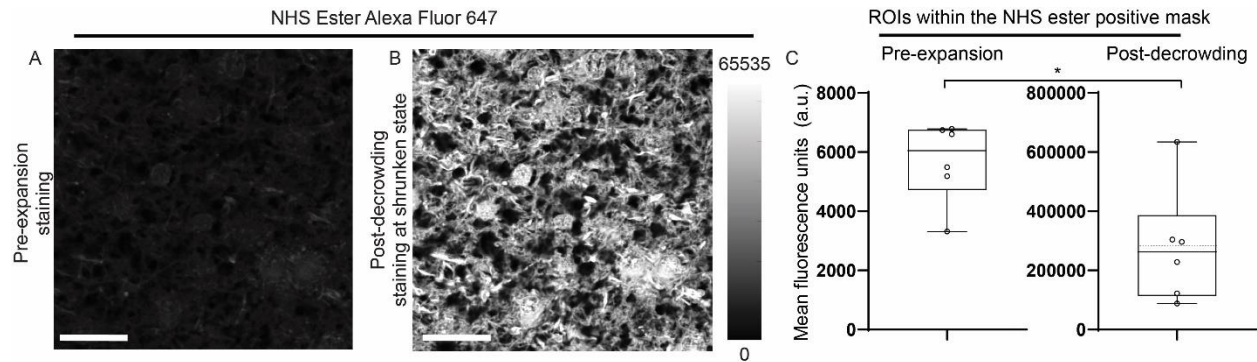
Fig. S10. dExPath retains proteins following softening. (A) Representative (n = 3 samples, each from a different patient) pre-expansion confocal image (single z slice) of an FFPE 5-μm-thick sample of human glioma tumor. The samples underwent processing (as in **Fig. S3A**, tissue deparaffinization, rehydration, and staining) and staining with NHS ester Alexa Fluor 647. Images were acquired using the fluorescent filter 640ex/685em. (B) Confocal image of the sample from A, following post-decrowding NHS ester staining and then tissue shrinkage. The sample from A was treated with anchoring, gelation (as in **Fig. S1B**), softening (as in **Fig. S1C**), and decrowding (as in **Fig. S1D**), then stained with NHS ester Alexa Fluor 647 post-decrowding, before the tissue was shrunken (by adding high salt solution) back to ~1.3x of the original size, and imaged via confocal microscopy. Image is a single z-slice centered at the same midpoint as the original image; images were of the same fields of view as in (A), using identical hardware and software settings, except that the exposure time was reduced post-decrowding in the shrunken state to avoid saturating the camera (pre-expansion, 500 ms exposure time; post-decrowding, 100 ms exposure time). (C) Mean fluorescence intensities from pre-expansion images (left bar graph) averaged across regions of interest (ROIs) within NHS ester positive regions (n = 3 tissue samples, each from a different patient). Mean fluorescence intensities, from post-decrowding-staining, shrunken state, images (right bar graph), averaged across the same ROIs used for pre-expansion images and corrected for exposure time, by multiplying by an factor equal to pre-expansion exposure time divided by post-decrowding exposure time. Brightness and contrast settings: first set by the ImageJ auto-scaling function, and then manually adjusted (by raising the minimum-intensity threshold and lowering the maximum-intensity threshold) to improve contrast in (C) and then images in (A) were displayed at the same brightness and contrast settings as (B). Quantitative analysis in (C) was conducted on raw image data. Box plot: individual values (open circles; 2

measurements were acquired from each patient), median (middle line), mean (dotted line), first and third quartiles (lower and upper box boundaries), lower and upper raw values (whiskers). Statistical testing: 2-tailed paired t-test (non-Bonferroni corrected) was applied to NHS ester positive regions pre-expansion vs. NHS ester positive regions post-decrowding-stained, shrunken state. *, $p < 0.05$; ns, not significant. Scale bars (in biological units): (A, B) 29 µm. Linear expansion factors: (B) 1.3.
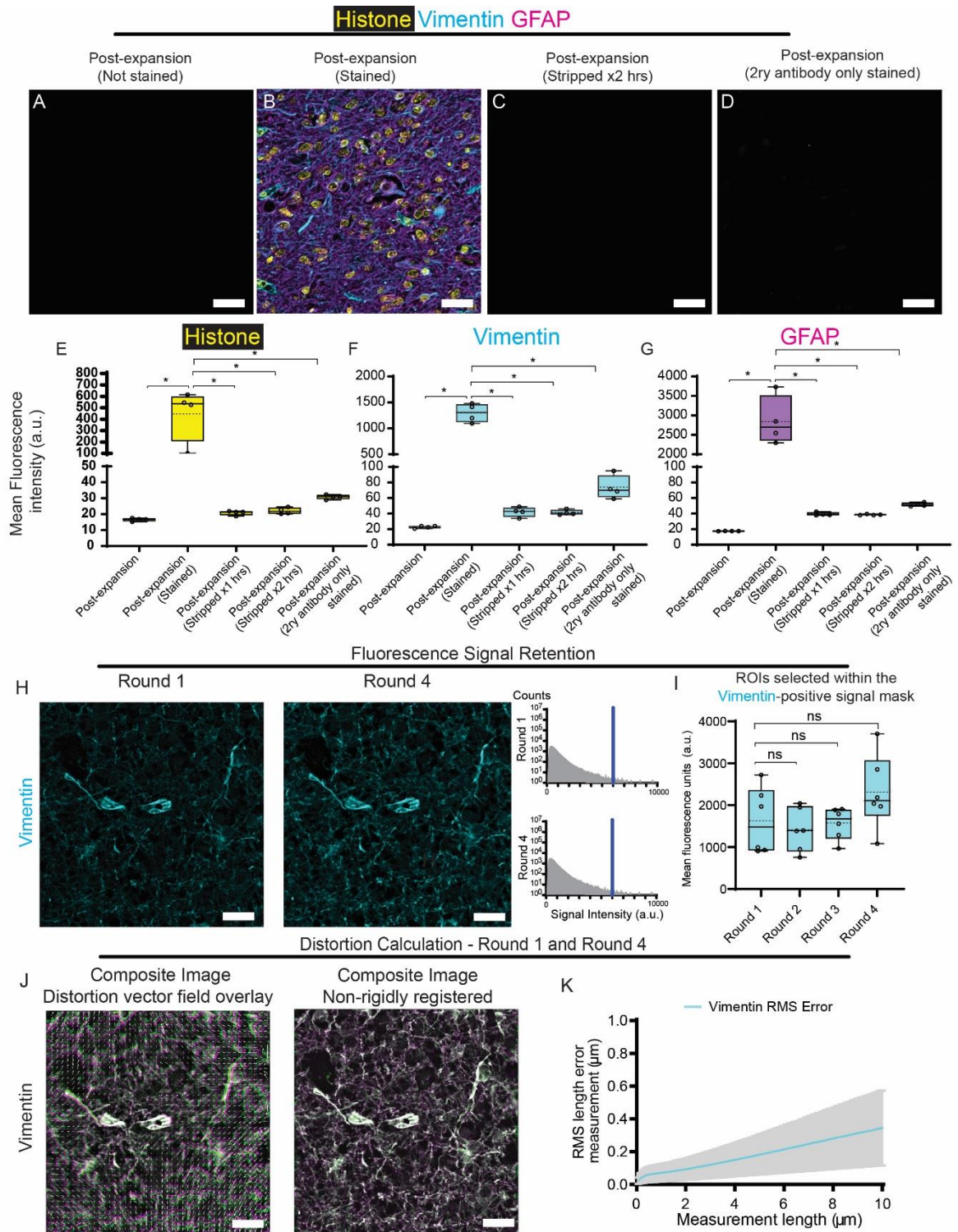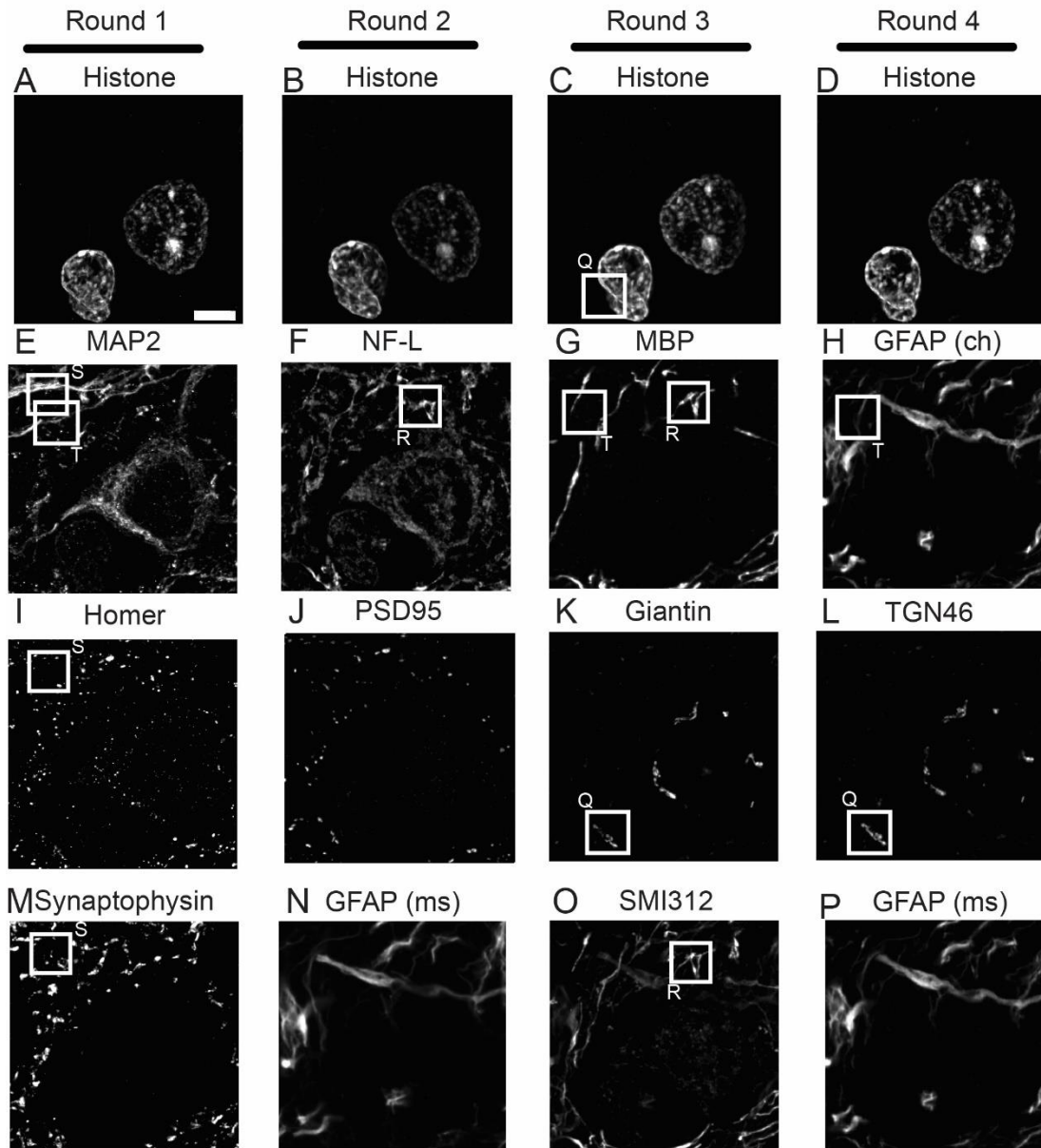
Fig. S11. dExPath antibody stripping clears fluorescence signals and enables multiple rounds of post-decrowding immunostaining. (A) Representative (n = 4 samples, from 2 patients with 2 samples per patient) confocal images (sum intensity z-projections of image stacks) of an FFPE, 5-µm-thick tissue slice of human high-grade glioma. Sample

underwent format conversion (**Fig. S1A**; tissue deparaffinization and rehydration), anchoring, gelation (**Fig. S1B**), softening (**Fig. S1C**), decrowding (**Fig. S1D**), no immunostaining, and confocal imaging at 4x linear expansion (**Fig. S1E**). (B) Sample used for (A) after immunostaining post-decrowding for histone H3, vimentin, and GFAP, and imaging at ~4x linear expansion (**Fig. S1E**). Sum intensity z-projection of an image stack covering the biological thickness of the original z-projection (used for all expanded images throughout this figure); image was of the same field of view as in (A), using identical hardware settings. (C) Sample used for (A) after antibody stripping for 2 hrs (**Fig. S1F**), expansion, and imaging at 4x linear expansion; image was of the same field of view as in (A), using identical settings. (D) Sample used for (A) after additional immunostaining with only the fluorescent secondary (abbreviated 2ry throughout this figure) antibodies, using the same staining conditions as used in (B), and confocal imaging at 4x linear expansion (**Fig. S1E**); image was of the same field of view as in (A), using identical settings. (E-G) Mean fluorescence intensities, from (from left to right in each graph) post-expansion (not stained, as in A), post-expansion (stained, as in B), post-expansion (stripped for 1 hr), post-expansion (stripped for 2 hrs, as in C), and post-expansion (2ry antibody-only stained, as in D), averaged across ROIs that exhibited prominent fluorescence for (E) histone H3, (F) vimentin, or (G) GFAP in the post-expansion (stained, as in B) state; colors correspond to the colors in (B) (n = 4 samples, from 2 patients with 2 samples per patient). Box plot: individual values (open circles; 2 measurements were acquired from each patient), median (middle line), mean (dotted line), first and third quartiles (lower and upper box boundaries), lower and upper raw values (whiskers). Statistical testing: 2-tailed paired t-test (non-Bonferroni corrected) was applied to post-expansion (stained) vs. all other post-expansion mean fluorescence intensities for each spectral channel. *, p < 0.05. (H) Representative (n = 3 samples, each from a different patient) confocal images of FFPE, 5-μm-thick tissue of 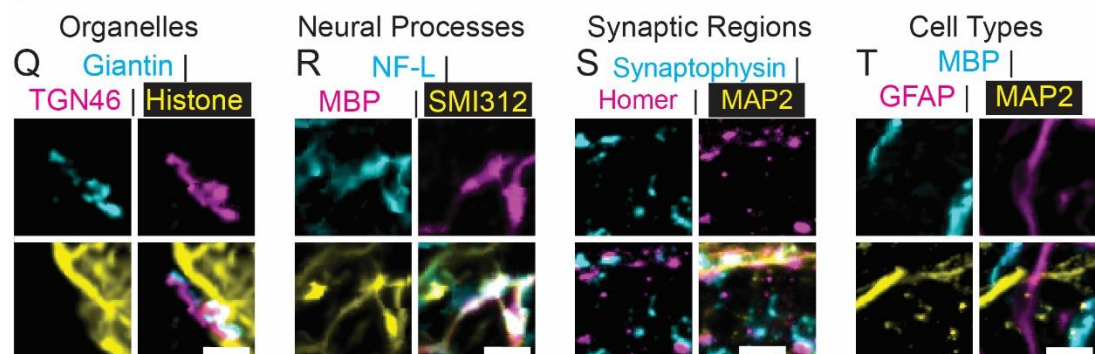human high-grade glioma. The sample underwent format conversion (**Fig. S1A**; tissue deparaffinization and rehydration), anchoring, gelation (**Fig. S1B**), softening (**Fig. S1C**), decrowding (**Fig. S1D**), and immunostaining post-decrowding for vimentin, and confocal imaging at ~4x linear expansion (**Fig. S1E**) after one round (left panel, Round 1) of post-decrowding staining. The sample then underwent three additional sequential rounds of antibody stripping (**Fig. S1F**), re-staining post-decrowding with anti-vimentin, and 4x linear expansion (**Fig. S1E**), for a total of four rounds of immunostaining (right panel, Round 4). Shown in both cases is the sum intensity z-projection of the confocal image stack, corresponding to the

biological thickness of the z-projection in Round 1, taken under identical settings and of the same field of view as in Round 1. For display purposes, histograms of pixel values for vimentin images were adjusted so that 1% of the pixels were saturated (histograms for Rounds 1 and 4 are shown to the right of the Round 4 image, top and bottom, respectively). Vertical blue line, upper look-up table (LUT) limit (so that 1% of pixels are saturated). (I) Mean fluorescence intensities, from Round 1 to Round 4 post-expansion images (raw image data, not adjusted as in the images of H), averaged across ROIs that exhibited prominent fluorescence for vimentin (n = 3 samples, each from a different patient). Box plot: individual values (open circles; 2 measurements were acquired from each patient), median (middle line), mean (dotted line), first and third quartiles (lower and upper box boundaries), lower and upper raw values (whiskers). Statistical testing: 2-tailed paired t-test (non-Bonferroni corrected) was applied on Round 1 vs each of Round 2 through 4, post-expansion mean fluorescence intensities. Statistical significance: ns, not significant. (J) (Left panel) Same sample as in (H), with composite image overlaying Round 1 (magenta) and Round 4 (green) post-expansion images prior to non-rigid registration. Distortion vector field overlay (white arrows) derived from non-rigid registration. (Right panel) Composite image of Round 1 and 4 as in left panel, following non-rigid registration. (K) RMS length measurement errors obtained by comparing Round 1 and Round 4 post-expansion images such as those of (J) (n = 3 samples, each from a different patient). Line, mean; shaded area, standard deviation. Scale bars (in biological units): (A-D) 90 μm; (H) 30 μm; (J) 30 μm.

Same field of view, registered over 4 rounds of immunostaining

Round 1   Round 2   Round 3   Round 4

A   Histone   B   Histone   C   Histone   D   Histone

E   MAP2   F   NF-L   G   MBP   H   GFAP (ch)

I   Homer   J   PSD95   K   Giantin   L   TGN46

M Synaptophysin N   GFAP (ms)   O   SMI312   P   GFAP (ms)

Co-localized staining across rounds

Q   Organelles   R   Neural Processes   S   Synaptic Regions   T   Cell Types
    Giantin | NF-L | Synaptophysin | MBP |
    TGN46 | Histone   MBP | SMI312   Homer | MAP2   GFAP | MAP2

Fig. S12. dExPath antibody multiplexing of archival pathology samples of human cortex.
(A-L) Example confocal images of the same field of view, for 10 distinct protein targets, from a formalin-fixed paraffin-embedded (FFPE), 5-µm-thick tissue of human cortex, which underwent format conversion (as in **Fig. S1A**; including tissue deparaffinization and rehydration), anchoring, gelation (as in **Fig. S1B**), softening (as in **Fig. S1C**), decrowding (as in **Fig. S1D**), and 4 total rounds of post-decrowding immunostaining (as in **Fig. S1E**), alternating with antibody stripping treatment (as in **Fig. S1F**).   The protein targets included (A-D) histone H3, which was a common target across all 4 rounds of staining, to provide a constant landmark for image registration across separate rounds; (E) microtubule-associated protein 2 (MAP2); (F) neurofilament light chain (NF-L); (G) myelin-basic protein (MBP); (H) glial fibrillary acidic protein (GFAP) stained by a polyclonal antibody raised in chicken ("ch", for contrast to a differently sourced GFAP antibody, below); (I) Homer, a post-synaptic protein; (J) Post-synaptic density 95 (PSD95), another post-synaptic protein; (K) Giantin, a cis-Golgi marker; (L) TGN46, a trans-Golgi marker; (M) synaptophysin, a pre-synaptic protein; (N) GFAP, stained by a mouse monoclonal ("ms"); (O) SMI-312, a monoclonal antibody against phosphorylated neurofilament subunits; (P) GFAP, stained as in N. White boxes are zoomed-in, and overlaid, in Q-T. (Q) Magnified views of the regions inside the solid white boxes in C, K, and L. Upper left, giantin; upper right, TGN46; lower left, histone H3; lower right, overlay of the other 3 images. (R) Magnified views of the regions inside the solid white boxes in F, G, and O. Upper left, NF-L; upper right, MBP; lower left, SMI-312; lower right, overlay of the other 3 images. (S) Magnified views of the regions inside solid white boxes in E, I, and M. Upper left, synaptophysin; upper right, Homer; lower left, overlay of Homer and synaptophysin; lower right, overlay of Homer, synaptophysin, and MAP2. (T) Magnified views of the regions inside solid white boxes in E, G, and H. Upper left, MBP; upper right, GFAP; lower left, MAP2; lower right, overlay of the other 3 images. All images are sum intensity z-projections of image stacks acquired with confocal microscopy. Brightness and contrast settings: first set by the ImageJ auto-scaling function, and then manually adjusted (by raising the minimum-intensity threshold and lowering the maximum-intensity threshold) to improve contrast for the stained structures of interest. Pixel intensity values were deliberately saturated for a subset of pixels, to facilitate visualizing the spatial distribution of the stains. The adjustments were individually performed for each image. Scale bars (in biological units): (A) 3.5 µm (Panels A-P show the same field of view in the tissue sample). (Q-T) 1.1 µm. Linear expansion factor, 3.9 x.
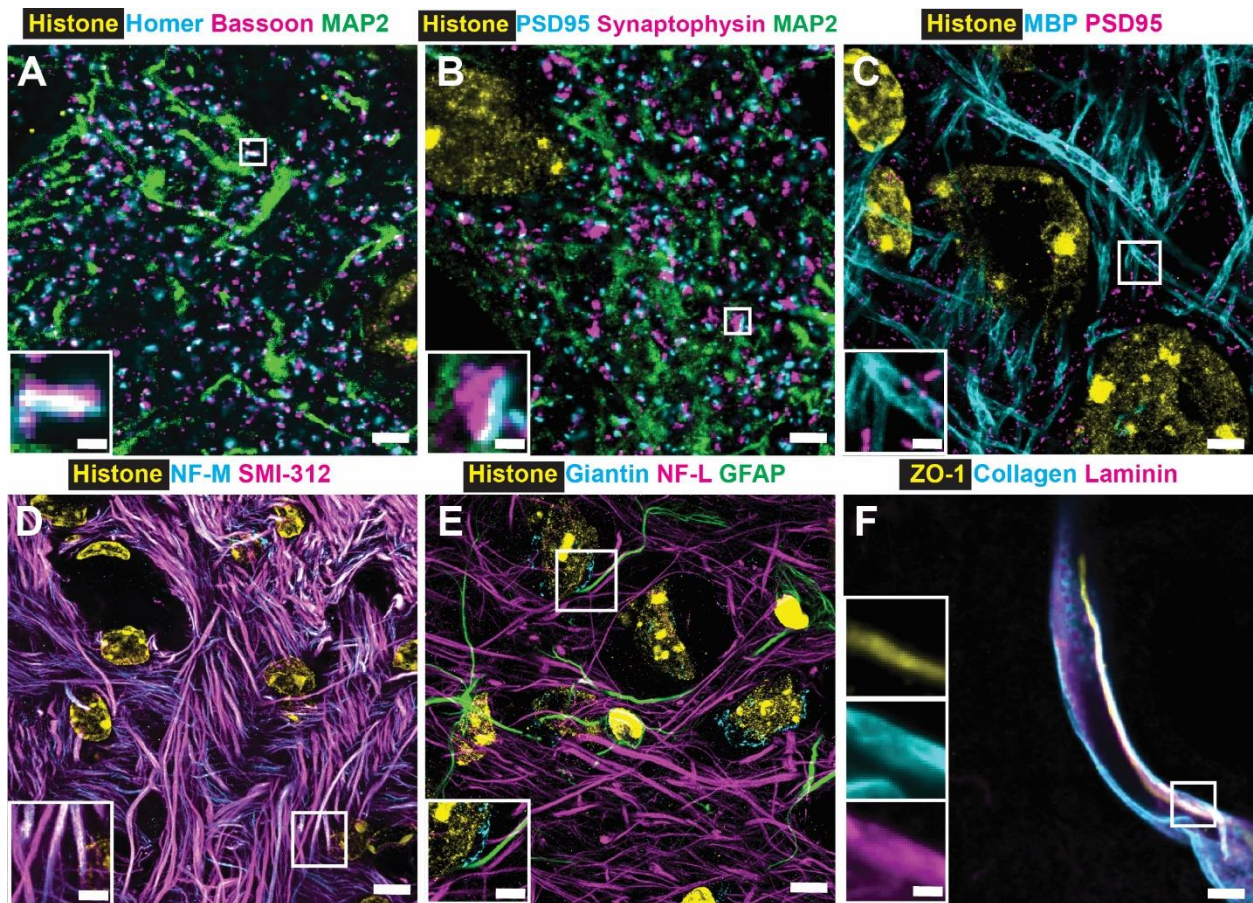
Fig. S13. dExPath applied to formaldehyde-fixed mouse brain tissue. (A–F) Confocal images of 4%-PFA-fixed, 10-µm-thick samples of mouse cortex. Samples underwent format conversion (**Fig. 1A**), anchoring, gelation (**Fig. 1B**), softening (**Fig. 1C**), decrowding (**Fig. 1D**), post-decrowding immunostaining, and confocal imaging at 4x linear expansion (**Fig. 1E**). The tissue samples were stained for the following: (A) histone H3 (a nuclear protein), homer (a postsynaptic protein), bassoon (a presynaptic protein), and MAP2. (B) histone H3, postsynaptic density protein 95 (PSD95, a postsynaptic protein), synaptophysin (a presynaptic protein), and MAP2. (C) histone H3, myelin-basic protein (MBP, a protein of myelinated axons), and PSD95. (D) histone H3, neurofilament medium chain (NF-M, a neurofilament subunit), and SMI-312 (a pan-axonal marker of neurofilaments). (E) histone H3, giantin (a protein of the Golgi complex), neurofilament light chain (NF-L, a neurofilament subunit distinct from NF-M), and GFAP. (F) zona occludens-1 (ZO-1, a protein of tight junctions), and laminin and collagen IV (two distinct proteins of the basement membrane of blood vessels). White boxes mark regions shown magnified in insets on the left. All images are sum intensity z-projections of a confocal image stack. Brightness and contrast settings in images (A-F): first set by the ImageJ auto-scaling function, and then manually

adjusted (by raising the minimum-intensity threshold and lowering the maximum-intensity threshold) to improve contrast of stained structures. Scale bars (in biological units): (A-B) outer panel, 2.25 μm; inset, 300 nm; (C) outer panel, 2.5 μm; inset, 500 nm; (D) outer panel, 6 μm; inset, 1.25 μm; (E) outer panel, 6 μm; inset, 2 μm; (F) outer panel, 1.45 μm; inset, 400 nm; Linear expansion factors: (A) 4.0 x; (B) 4.1 x; (C) 4.2 x; (D) 4.0 x; (E) 3.9 x; (F) 4.2 x.

In more detail: dExPath worked well on mouse brain tissue, fixed through standard PFA fixation protocols, and resulted in high quality images of mouse cortex and white matter, using antibodies against a wide array of proteins including bassoon, synaptophysin, homer, post-synaptic density protein 95 (PSD95), MAP2, histone H3, MBP (*37, 126*), neurofilament medium chain (NF-M), SMI-312, neurofilament light chain (NF-L)), GFAP, giantin, laminin, collagen IV(*141*), and zona occludens-1 (ZO-1) (*92*). Pre- and post-synaptic markers were localized near each other (**Fig. S13A,B**). MBP staining revealed tubular structures, appropriate for putative axons (**Fig. S13C**). Staining intermediate filament proteins (NF-M, NF-L, SMI-312 and GFAP) resulted in expected patterns (**Fig. S13D, E**). Staining for components of blood vessels, laminin, collagen IV, and ZO-1, showed patterns reminiscent of blood vessels (**Fig. S13F**). Thus, we show that dExPath provides an avenue for decrowded nanomapping of proteins in many subcellular locations within multiple cell types in PFA-fixed brain tissue.
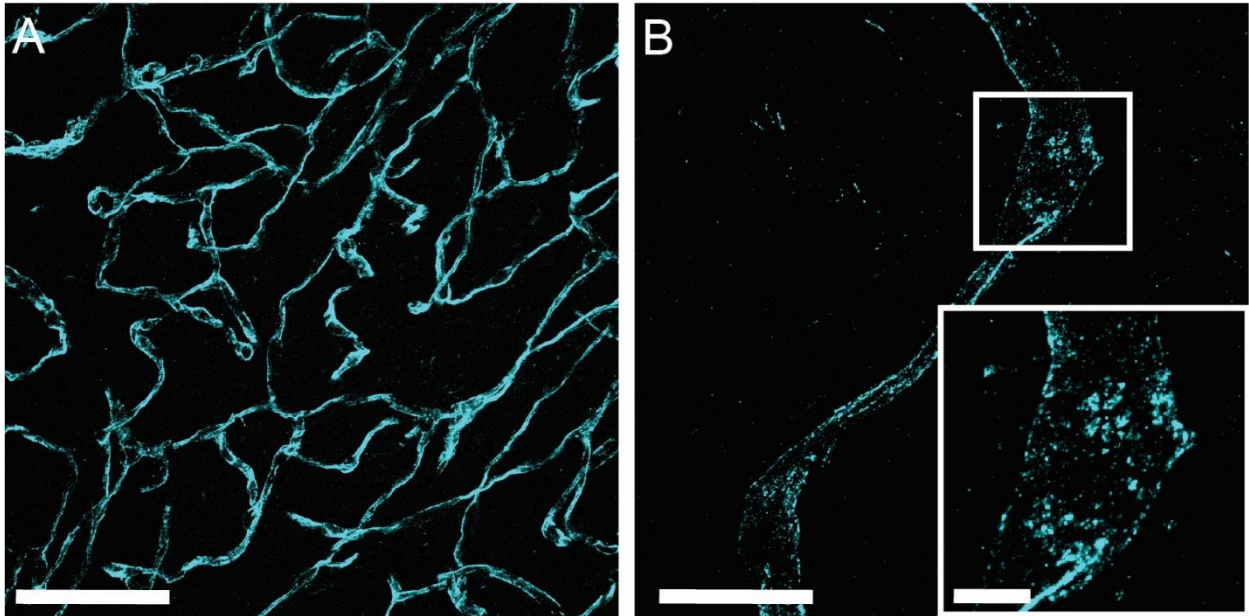
Fig. S14. dExPath is compatible with thick, formaldehyde-fixed mouse brain tissue. (A-B) Confocal images from the middle of a 4%-PFA-fixed, 100-μm-thick sample of mouse cortex. Sample underwent format conversion (**Fig. 1A**), anchoring, gelation (**Fig. 1B**), softening (**Fig. 1C**), decrowding (**Fig. 1D**), post-decrowding immunostaining, and confocal imaging at ~4x linear expansion (**Fig. 1E**). The tissue sample was stained for aquaporin 4 (a protein of brain blood vessels). Images are max intensity z-projections from the middle of a (A) 240-μm thick confocal image stack at 10x magnification and a (B) 70 μm thick confocal image stack at 40x magnification.

DAPI
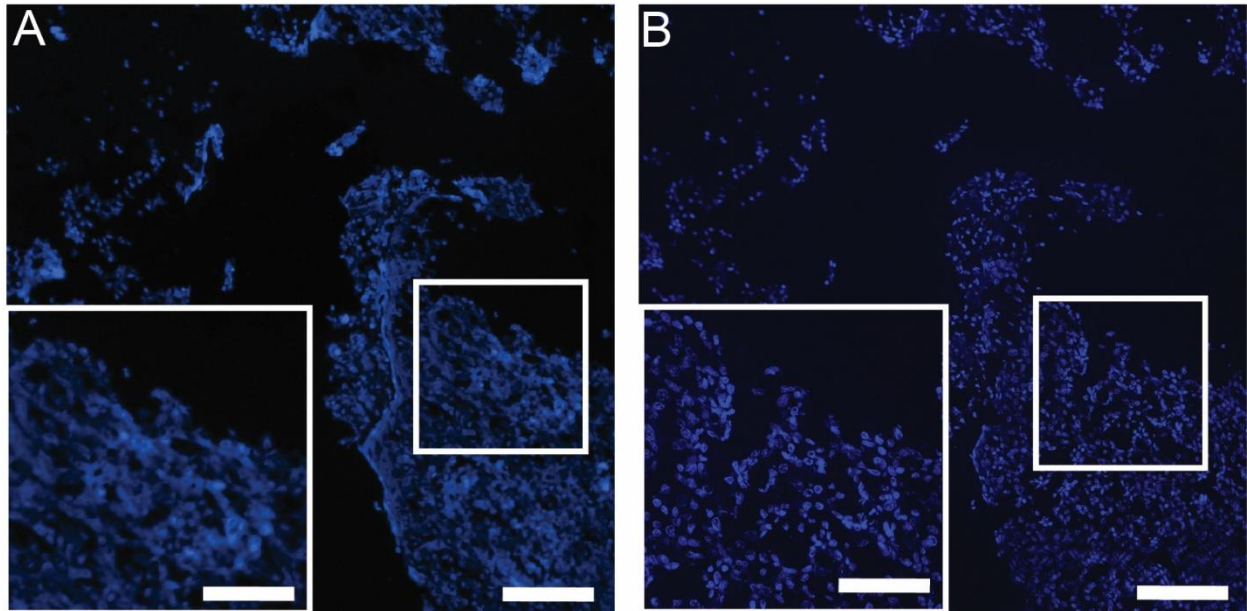
Fig. S15. Non-isotropic expansion of human lymph node tissue following dExPath. (A) Representative pre-expansion wide field images of FFPE 5-µm-thick slices of human lymph node tissue (A, n = 3 samples, each from a different patient) which underwent processing as in **Fig. S4A** (tissue deparaffinization, rehydration), with staining for DAPI. White box on the right marks region shown magnified in inset on the left. (B) Post-expansion image of the same fields of view as shown in (A). Specifically, samples were treated with anchoring and gelation (as in **Fig. S4B**), followed by softening (as in **Fig. S4C-D**), and another round of DAPI staining, with ~2x linear expansion, and imaging with wide field microscopy. White boxes in (B), as in (A). Brightness and contrast settings in images (A-B): first set by the ImageJ auto-scaling function, and then manually adjusted (by raising the minimum-intensity threshold and lowering the maximum-intensity threshold) to improve contrast for stained structures. Scale bars (in biological units): (A-B) outer panel 180 µm; inset, 100 µm. Linear expansion factor: (B) 2.1x.

Description – Movies

Movie S1. dExPath 3-dimensional image stack of thick, formaldehyde-fixed mouse brain tissue. Confocal images from the middle of a 4%-PFA-fixed, 100-μm-thick sample of mouse cortex. Sample underwent format conversion (**Fig. 1A**), anchoring, gelation (**Fig. 1B**), softening (**Fig. 1C**), decrowding (**Fig. 1D**), post-decrowding immunostaining, and confocal imaging at ~4x linear expansion (**Fig. 1E**). The tissue sample was stained for aquaporin 4 (a protein of brain blood vessels). Images are max intensity z-projections from the middle of a 240-μm thick confocal image stack at 10x magnification showing all images through the 3-dimensional stack. Brightness and contrast settings in images: first set by the ImageJ auto-scaling function, and then manually adjusted (by raising the minimum-intensity threshold and lowering the maximum-intensity threshold) to improve contrast of stained structures. Scale bars (in physical units): 240 μm.

Movie S2. dExPath 3-dimensional image stack volume of thick, formaldehyde-fixed mouse brain tissue. Confocal images from the middle of a 4%-PFA-fixed, 100-μm-thick sample of mouse cortex. Sample underwent format conversion (**Fig. 1A**), anchoring, gelation (**Fig. 1B**), softening (**Fig. 1C**), decrowding (**Fig. 1D**), post-decrowding immunostaining, and confocal imaging at ~4x linear expansion (**Fig. 1E**). The tissue sample was stained for aquaporin 4 (a protein of brain blood vessels). Images are from the middle of a 240-μm thick confocal image stack at 10x magnification showing 3-dimensional projections rotating about the x axis. Brightness and contrast settings in images: first set by the ImageJ auto-scaling function, and then manually adjusted (by raising the minimum-intensity threshold and lowering the maximum-intensity threshold) to improve contrast of stained structures. Scale bars (in physical units): 240 μm.

Table S1. Comparison of tissue expansion protocols. Abbreviations: FFPE = formalin-fixed-paraffin-embedded; PBS = phosphate buffered saline; SDS = sodium dodecyl sulfate; EDTA = ethylenediaminetetraacetic acid; LysC = endoproteinase LysC; TBS = tris-buffered saline; NaCl = sodium chloride; AcX = Acryloyl-X; PFA = paraformaldehyde; AA = acrylamide; SA = sodium acrylate; Bis = N,N'-methylenebisacrylamide; APS = ammoniium persulfate; TEMED = tetramethylethylenediamine; 4-HT = 4-Hydroxy-2,2,6,6-tetramethylpiperidine 1-oxyl

Protocol	Sample type demonstrated	Expansion-induced distortion	Fixations compatible with method	Chemistry to covalently anchor proteins to the hydrogel	Gelation	Homogenization buffer	Homogenization conditions
Past protocol that was optimized for clinical samples							
ExPath*	cell culture, human normal and cancer tissues (breast, prostate, lung, colon, pancreas, kidney, liver and ovary)	3-4%	4% PFA, FFPE, Fresh Frozen	AcX	1x PBS, 2M NaCl, 8.6% (w/v) SA, 2.5% (w/v) AA, 0.10% (w/v) Bis, 0.01% (w/v) 4-HT, 0.2% (w/v) TEMED, 0.2% (w/v) APS	50 mM Tris, pH 8, 1M NaCl, 25 mM EDTA, 0.5% Triton X-100, 8U/mL Proteinase K	60 C for 3 hrs
Protocols for post-expansion immunostaining							

proExM (via autoclave)	mouse tissues (brain)	uncharacterized	4% PFA	AcX	1x PBS, 2M NaCl, 8.6% (w/v) SA, 2.5% (w/v) AA, 0.15% (w/v) Bis, 0.01% (w/v) 4-HT, 0.2% (w/v) TEMED, 0.2% (w/v) APS	100 mM Tris base (pH unadjusted), 1% SDS, 5% Triton-X	121 C (autoclave) for 1 hr
proExM (via LysC)	mouse tissues (brain)	uncharacterized	4% PFA	AcX	1x PBS, 2M NaCl, 8.6% (w/v) SA, 2.5% (w/v) AA, 0.15% (w/v) Bis, 0.01% (w/v) 4-HT, 0.2% (w/v) TEMED, 0.2% (w/v) APS	25 mM Tris, pH 8.5, 1 mM EDTA, 33 µg/ml LysC, with 600U/ml collagenase II pre-treatment	37 C for > 8 hrs
MAP	cell culture, mouse tissues (brain, lung, spinal cord, liver, kidney, intestine)	2-3%	4% PFA along with the hydrogel monomer solution, including 30% AA, 10% SA, 0.05-0.1% Bis, and 0.1%VA-044 or V-50	PFA- and AA-mediated addition of acryloyl groups to proteins, during fixation	Same as fixative solution: 4% PFA, 30% AA, 10% SA, 0.05-0.10% Bis, 0.1%VA-044 or V-50	50 mM Tris, pH 9.0, 5.8% SDS, 200 mM NaCl	37 C overnight then 70 C for 0-50 hrs then 95 C for 1-24 hrs

UExM	cell culture, isolated centrioles	1-3%	4% PFA, 3% PFA + 0.1% glutaraldehyde, 0.7% PFA + 1% AA, 100% methanol (optimized on a per subcellular organelle basis)	PFA- and AA-mediated addition of acryloyl groups to proteins, during fixation, or as an additional step after fixation	1x PBS, 19% (w/w) SA, 10% (w/w) AA, 0.1% (w/w) Bis, 0.5% TEMED, 0.5% APS	50 mM Tris, pH 9.0, 5% SDS, 200 mM NaCl	95 C for 30 min
miriEx	mouse tissues (brain), human tissues (brain)	uncharacterized	4% PFA	Acrylic acid N-hydroxysuccinimide ester	1× PBS, 5.3% SA, 4% AA, 0.1% Bis, 0.5% VA-044	1x TBS, 5.8% SDS	70 C overnight
pan-ExM	cell culture	3-4%	3% PFA + 0.1% glutaraldehyde	PFA- and AA-mediated addition of acryloyl groups to proteins, as an additional	1x PBS, 19% (w/v) SA, 10% AA (w/v), 0.1% (w/v) DHEBA, 0.25% (v/v) TEMED, 0.25% (w/v) APS	50 mM Tris, pH 6.8, 5.8% SDS, 200 mM NaCl	73 C for 1 hr

				step after fixation			
ExR	mouse tissues (brain)	few percent	4% PFA, 2% AA followed by 30% AA	PFA- and AA-mediated addition of acryloyl groups to proteins, during fixation	0-8.625% SA, 2.5% -13.75% AA, 0.038-0.075% Bis, 0.01% HT, 0.025-0.2% TEMED, 0.025-0.2% APS	50 mM Tris, pH 9, 5.8% SDS, 200 mM NaCl	95 C for 1 hr
mExM	mouse tissues (brain)	few percent	4% PFA + 0.1% glutaraldehyde	AcX	1x PBS, 11.7%M NaCl, 8.6% (w/v) SA, 2.5% (w/v) AA, 0.15% (w/v) Bis, 0.01% (w/v) 4-HT, 0.5% (w/v) TEMED, 0.2% (w/v) APS	100 mM Tris, pH 8, 4% SDS, 0.5% Polyethylene glygocl 20000, 100 mM dithiothreitol	100 C for 30 min then 80C for 2 hrs, or autoclave for 1 hr
dExPath	mouse tissues (brain), human normal and cancer tissues (brain)	2-4%	4% PFA, FFPE	AcX	1x PBS 2M NaCl 8.6% (w/v) SA 2.5% (w/v) AA 0.10% (w/v) Bis 0.01% (w/v) 4-HT 0.2% (w/v) TEMED 0.2% (w/v) APS	50 mM Tris, pH 8, 20% SDS, 0.5% Triton X-100, 25 mM EDTA, 100 mM β-mercaptoethanol	37 C for 30 min, 121 C (autoclave) for 1 hr

*ExPath does not allow for post-expansion immunostaining

Table S2. Antibodies Used

Primary Antibodies				
Target	**Host**	**Manufacturer**	**Catalog No.**	**Successful Staining**
Aquaporin (4/18)	Mouse	Abcam	ab9512	Yes
ATRX	Rabbit	Millipore Sigma	HPA001906	Yes
α-SMA (1A4)	Mouse	Agilent	M085129-2	Yes
α-synuclein (LB509)	Rabbit	Cell Signaling Technology	51510	Yes
α-synuclein (EP1536Y)	Rabbit	Abcam	ab51253	No
β-amyloid (1-42)	Rabbit	Cell Signaling Technology	D9A3A	Yes
β-amyloid (LN27)	Mouse	ThermoFisher Scientific	13-0200	Yes
β-amyloid (BAM01)	Mouse	ThermoFisher Scientific	MA5-11617	No
β-III-tubulin	Rabbit	Abcam	ab18207	Yes
Bassoon (SAP7F407)	Mouse	Abcam	ab82958	Yes
CD31(EP3095)	Rabbit	Abcam	ab134168	Yes
CD68 (KP1)	Mouse	Abcam	ab955	No
CNPase	Mouse	Millipore Sigma	MAB326	No
Collagen IV	Goat	Millipore Sigma	AB769	Yes
Collagen IV	Rabbit	Abcam	ab6586	Yes
EAAT1 (D44E2)	Rabbit	Cell Signaling Technology	5684	Yes
GFAP (GA5)	Mouse	ThermoFisher Scientific	14-9892-82	Yes
GFAP	Chicken	Novus Biologicals	NBP105198	Yes
GFAP	Chicken	Aves Labs	GFAP	Yes
Giantin	Rabbit	Biolegend	924302	Yes
Iba1	Rabbit	WAKO	019-19741	Yes

Histone-H3	Goat	Abcam	ab12079	Yes
Homer 1	Rabbit	Synaptic Systems	160 003	Yes
Hsp60	Mouse	Abcam	ab59457	No
ki67	Mouse	BD Biosciences	550609	Yes
ki67	Rabbit	Millipore Sigma	AB9260	Yes
Laminin	Chicken	LSBio	LS-C96142	Yes
MAP2	chicken	Novus Biologicals	NB300213	Yes
MBP	Chicken	Millipore Sigma	AB9348	Yes
NEFL (NF70)	Chicken	ThermoFisher Scientific	PA1-10000	Yes
NeuN	Guinea Pig	Synaptic Systems	266 004	Yes
NeuN	Mouse	Millipore Sigma	MAB377	No
Neurofilament-M	Rabbit	Millipore Sigma	AB1987	Yes
O4 (81)	Mouse	Millipore Sigma	MAB345	No
Olig 2	Rabbit	Millipore Sigma	AB9610	Yes
Olig 2 (EP12)	Rabbit	Millipore Sigma	387R-17	Yes
Olig 2	Guinea Pig	Millipore Sigma	ABE1024	No
PDGFRB	Rabbit	ThermoFisher Scientific	PA5-14718	No
PDI (C81H6)	Rabbit	Cell Signaling Technology	3501	Yes
Phospho-tau (AT8)	Mouse	ThermoFisher Scientific	MN1020	Yes
Phospho-tau (AT180)	Mouse	ThermoFisher Scientific	MN1040	Yes
PSD95	Rabbit	Cell Signaling Technology	2507	Yes
PSD95(7E3)	Mouse	Santa Cruz Biotechnology	sc32290	No
SMI312	Mouse	Biolegend	837904	Yes
Spinophilin (PPP1R9B)	Sheep	Novus Biologicals	AF6465	Yes
Synapsin 1ab	Goat	Santa Cruz Biotechnology	sc-55774	Yes
Synaptophysin (SVP-38)	Mouse	Millipore Sigma	S5768	Yes
Tomm20	Rabbit	Santa Cruz Biotechnology	sc11415	Yes
Vimentin	Chicken	Abcam	ab24525	Yes

von Willebrand factor	Rabbit	ThermoFisher Scientific	AB7356	Yes
ZO-1 (ZO1-1A12)	Mouse	ThermoFisher Scientific	33-9100	Yes
Secondary Antibodies				
Target	**Host**	**Manufacturer**	**Catalog No.**	Yes
AlexaFluor 350, anti-goat	Donkey	ThermoFisher Scientific	A10040	Yes
AlexaFluor 405, anti-goat	Donkey	Abcam	ab175664	Yes
AlexaFluor 488, anti-chicken	Donkey	Jackson Immunoresearch Laboratories	703545155	Yes
AlexaFluor 488, anti-mouse	Donkey	Abcam	ab150109	Yes
AlexaFluor 488, anti-chicken	Goat	ThermoFisher Scientific	A11039	Yes
AlexaFluor 546, anti-rabbit	Donkey	ThermoFisher Scientific	A10040	Yes
AlexaFluor 546, anti-rabbit	Goat	ThermoFisher Scientific	A10035	Yes
AlexaFluor 555, anti-rabbit	Donkey	ThermoFisher Scientific	A31572	Yes
CF 640, anti-mouse	Donkey	Biotium	20177	Yes
CF 633, anti-chicken	Donkey	Biotium	20168	Yes

Protocol: Decrowding Expansion Pathology

This protocol is designed for 5-10 μm thick brain sections of human formalin-fixed paraffin embedded (FFPE) tissues or 5-10 μm thick brain mouse tissues fixed in 4% paraformaldehyde (PFA). Incubation times need to be adjusted for thicker tissues, e.g., 100 μm thick. For the reader's guidance, we have provided additional details for use in thicker mouse tissues.

A. STOCK SOLUTIONS (Anchoring, Gelation)

First, prepare the stock solutions and store in aliquots at -20°C for long term storage. We found that storing these solutions in 1-1.5 mL aliquots was ideal for use when preparing 1-20 tissue gels per day, 3-5 times per week.

1. Monomer solution:

#	Component	Stock concentration*	Amount (mL)	Final concentration*
	Table 1. Monomer Solution Composition			
1	Sodium acrylate	38	2.25	8.6
2	Acrylamide	50	0.5	2.5
3	N,N′-Methylenebisacrylamide	2	0.50	0.10
4	Sodium chloride	29.2	4	11.7
5	Phosphate buffered saline (PBS)	10x	1	1x
6	Water		1.15	
	Total		**9.4****	

*All concentrations are in g/100 mL in ultrapure deionized water except phosphate buffered saline (PBS) 10x. Remember, these are weight by volume (w/v) concentrations, so make sure, for example, when making the acrylamide stock solution, you have 2.5 g added to the vial and then fill up the vial to the 100 mL mark, or 0.25 g and fill up the vial to the 10 mL mark. DO NOT add 10 mL and then 0.25 g of solid or else your final concentration will be incorrect.
**9.4/10 mL with the remaining 6% volume brought up by initiator, accelerator and inhibitor.

Prepare the monomer solution at room temperature (RT). In a 10 mL conical tube add each component (**Table 1**) #1-6 in sequential order. After adding each component, vortex the components to ensure they are in solution. Once you have mixed all the components, dispense into 1-1.5 mL aliquots and then store at -20°C for long term storage.

2. Inhibitor solution

Prepare the 4-hydroxy-TEMPO (**4HT)** stock solution at RT made up at 0.5% w/v in water and then dispense into 1-1.5 mL aliquots.

3. Accelerator solution

Prepare the tetramethylethylenediamine (**TEMED)** stock solution at RT made up at 10% w/v in water and then dispense into 1-1.5 mL aliquots.

4. Initiator solution

Prepare the APS (**APS)** stock solution at RT made up at 10% w/v in water and then dispense into 1-1.5 mL aliquots.

*TEMED, APS, and 4HT stock solutions can be kept at -20°C for at least 6 months.

5. Anchoring solution

Acryloyl-X, SE (Life Technologies, A20770) (**AcX**) comes in a solid powder. Prepare the AcX stock solution by adding 500 µL anhydrous dimethylsulfoxide (DMSO) into the original container resulting in a 10 mg/mL stock solution, dispense into 20 µL aliquots and store in a desiccated environment at -20°C for long term storage.

5. PBS 1x in Triton-X (PBST)

Prepare a PBST stock solution at RT made up of PBS 1x with 0.5% Triton-X (v/v) and store at RT in 10 mL conical tube. Make fresh every week.

B. BUFFERS (Softening, Immunostaining)

Table 2. Softening Buffer Composition (pH = 8.0)*	
1	50 mM Tris buffer
2	20% wt/vol Sodium dodecyl sulfate (SDS)
3	25 mM Ethylenediaminetetraacetic acid (EDTA)
4	0.5% Triton-X
5**	100 mM beta-mercaptoethanol (BME)

*Buffer can be stored at room temperature. Should be made fresh regularly every week without beta-mercaptoethanol (BME) (**Table 2**).

**IMPORTANT: Use a 14M stock solution of BME and add immediately prior to use with tissue to achieve a final concentration of 100 mM BME in softening buffer. DO NOT store Softening buffer with BME.

Prepare Softening buffer by first weighing out the solid SDS powder and adding into a glass container with a magnetic stirrer. Then, add deionized water to below the desired volume to leave sufficient room for the Tris, EDTA and Triton-X. Stir at a temperature of approximately 90°C. Then, add the Tris buffer, using a stock solution of Tris. We use a 1 or 2 M Tris buffer stock solution. Then add the EDTA, using a stock solution of 500 mM EDTA. Allow components to mix well so they all go into solution, and once that has occurred add the Triton-X. Then adjust pH = 8.0 by slowly adding stock concentrated hydrochloric acid. Then store the Softening buffer WITHOUT the BME at room temperature. Add the BME immediately prior to using with tissue.

Collagenase Buffer (make fresh each time):

Table 3. Collagenase Buffer Composition*	
1	Hanks' Balanced Salt Solution (1x),(HBSS), with calcium, with magnesium, no phenol red (Gibco, Thermofisher #14025134)
2	Collagenase II 1500 U/ml (Gibco, Thermofisher #17101015)

Prepare Collagenase buffer by adding HBSS 1x stored at RT into the collagenase container to achieve a final concentration of Collagenase II of 1500 U/mL (**Table 3**). <u>No not store but make fresh each time.</u>

Table 4. Immunostaining Buffers	
1	**Blocking buffer**: MAXblock™ Blocking Medium (Active Motif)
2	**Staining buffer**: MAXbind™ Staining Medium (Active Motif)
3	**Washing buffer**: MAXwash™ Washing Medium (Active Motif)

We used these commercial immunostaining buffers for blocking, staining, and washing. However, the protocol can be used with any conventional immunofluorescence protocol, e.g., use of normal goat serum rather than the blocking buffer from Active Motif.

C. Step-by-step PROTOCOL: Decrowding ExPath Protocol for Fixed Human Tissues
Step 1. FORMAT CONVERSION
For formaldehyde-fixed paraffin-embedded (FFPE) clinical samples
1. Completely immerse the tissue slide sample (herein, "slide") through a series of solutions, by sequentially immersing the slide for three (3) mins in each solution in the following order (**Step 1.1**): xylene → xylene → 50/50 solution of xylene/100% ethanol → 100% ethanol → 95% ethanol → 90% ethanol→ 80% ethanol → 50% ethanol → deionized water → deionized water. All steps are done at RT. All ethanol dilutions from 95% down to 50% are diluted with deionized water.

2. Remove any excess deionized water from around and on top of the tissue by air drying and using a Kim wipe.

     *Removing excess deionized water ensures that the anchoring solution is not diluted.

3. Place in 1x PBS for 5 min and then remove any excess PBS from around and on top of the tissue by air drying and using a Kim wipe.

For 4% paraformaldehyde (PFA) samples
1. Completely the immerse tissue slide three (3) times in 1x PBS for 5 min each time at RT.
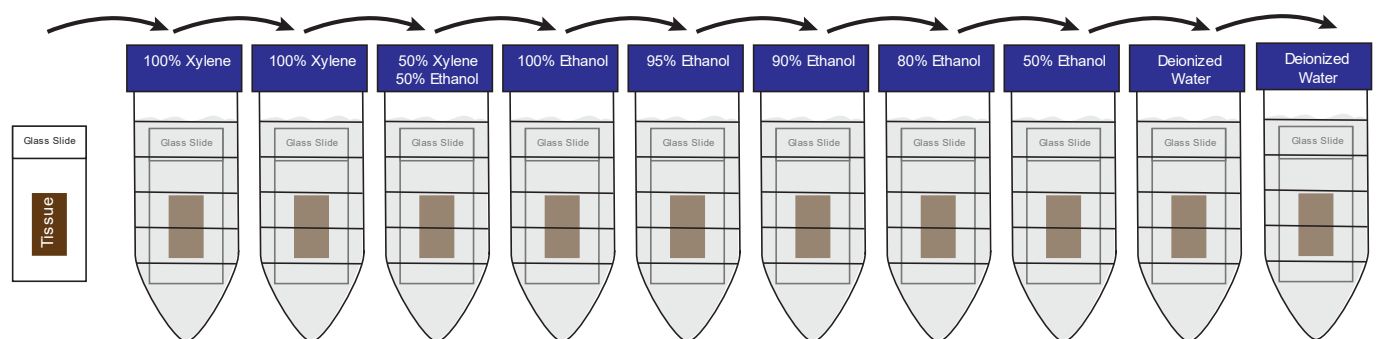
Step 1.1: Deparaffinization and rehydration. Tissue glass slide with FFPE tissue (brown) is sequentially transferred starting in xylene through subsequent solutions of varying ethanol concentration and eventually to deionized water to deparaffinize and rehydrate tissue prior to anchoring and gelation.

Pre-Expansion Staining: If the user wishes to do pre-expansion staining for comparison between pre-expansion staining and post-expansion staining on the same tissue, please see below section **Pre-Expansion Staining. The user would then proceed from **Step 1** to **Step 1-Extra: Pre-Expansion Staining.**

Step 2. ANCHORING & GELATION

Anchoring
1. Use the 10 mg/mL aliquot of AcX stock solution and allow it to come to RT.
2. Dilute stock AcX solution to a final concentration of 0.1 mg/ml using stock solution of PBST to prepare the working AcX solution.
3. To each slide, add 200 - 500 µL of working AcX solution.
     *It is important to make sure the tissue is fully covered with working AcX solution.
4. Incubate slides for 30 min at RT and then transfer the slides for another 1.5 hours to a temperature of 37°C
     *Incubate slides in a humidified closed container.
     **If desired, this reaction can be run overnight at 4°C and then for 1 hour at 37°C to ensure complete gelation.

***For 50-100 µm thick PFA fixed mouse brain slices do an overnight incubation at 4°C and then 1 hour at 37°C to ensure complete anchoring.

Gelation
5. Remove the AcX solution from the slide by washing three (3) times in 1x PBS for three (3) min each wash

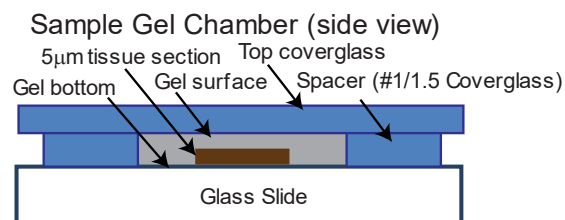6. Remove any excess PBS from around and on top of the tissue by air drying and using a Kim wipe.

   *Removing excess PBS ensures that the gelling solution is not diluted

7. Assemble a gel chamber by first sandwiching the tissue between the slide and a coverslip, with spacers on either side of the tissue section to prevent compression of the tissue (**Step 2.7**).
       *Spacers are made from cut coverslips using a diamond knife.
       **For most human tissue sections in clinical settings (5-10 µm thick), one piece of cover glass (VWR micro cover glass, 24x60mm, No. 1.5) can be used for spacers and a whole, uncut cover glass for the top cover glass.

Sample Gel Chamber (side view)
5µm tissue section   Top coverglass
Gel bottom   Gel surface   Spacer (#1/1.5 Coverglass)
Glass Slide

Step 2.7. Gel Chamber. Gel chamber for gelation of anchored tissue. The tissue is positioned between the glass slide and the top cover glass, with cover glass spacers on each end to allow for space for the gelation solution to enter the chamber to form the gel and without compressing the tissue.

8. Make the gelling solution (**Table 5**) by mixing 4 solutions in the following order: a) monomer solution, b) TEMED (accelerator), c) 4HT (inhibitor), d) APS (initiator). The mixture should be vortexed to ensure full mixing.

   ***HT** which inhibits gelation to enable diffusion into tissue sections.

   ****TEMED** accelerates radical generation by APS.

   *****APS** initiates the gelling process, so it needs to be added last to prevent premature gelation.

Table 5. Gelling Solution Composition				
#	Component	Amount of stock solution (µL)	Dilution ratio	Final concentration (w/v)
1	Monomer solution	187	N/A	N/A
2	4HT (inhibitor)	4	1:50	0.01%
3	TEMED (accelerator)	4	1:50	0.2%
4	APS (initiator)	5	1:50	0.2%
	Total (µL)	**200**		

9. Add gelling solution into the gelling chamber by using a micropipette with a 200 µL tip.

    a) <u>THIN sections, 5-10 µm thick</u>: Use freshly prepared gelling solution (adding APS at the very end). Make sure at least a 100-fold excess volume of monomer solution is used, e.g., ~200 µl of gelling solution for each tissue section on the slide, and then incubate for 30 min at 4°C in a humidified environment followed by 2.5 hours at 37°C.

        *You can also perform the incubation overnight at 4°C followed by 1.5 hours at 37°C.

    b) <u>THICK sections, 50-100 µm thick</u>. Use freshly prepared gelling solution (without APS) making sure the whole tissue section is immersed in the solution and incubate at 4°C in a humidified environment overnight. Then remove excess gelling solution (without APS) and add fresh gelling solution (with APS) and incubate for 30 min at 4°C in the gel chamber and then for 2.5 hours at 37°C.

10. Once the sample is gelled you can proceed to softening and decrowding (below), or storage by placing the slide chamber at 4°C inside a humidified container such as a Petri dish with a damp Kim wipe (or other container as appropriate) sealed with Parafilm for storage. You can also cut out the tissue gels and transfer into an airtight Eppendorf tube for later use.

    a. For clinical FFPE tissues that are tightly attached to the charged slide: in those cases, the user can store the whole slide as noted above until softening.

    b. For tissues attached to non-charged slides: generally, the user can gently remove tissues with a single edge razor blade (Fisher Scientific 17-989-126) or a brush to store separately.

Step 3. Softening

1. Take off the top cover glass of the gel chamber using a razor blade placed at the edge of the coverslip, sliding the blade along the coverslip side touching the gel surface and then gently using the blade to lift the coverslip off the gel surface.

2. Trim the tissue-containing-gel, keeping away from the tissue but removing excess gel to minimize volume by using a sharp razor blade, and cut a corner in an off-angle fashion to keep track of the orientation of tissue for later steps (e.g., when the gel is

transparent, and orientation is difficult to ascertain). This step will help determine the gel surface and the gel bottom (**Step 3.2**).

Sample Gel Orientation (top view)

Gel   Tissue

Glass Slide
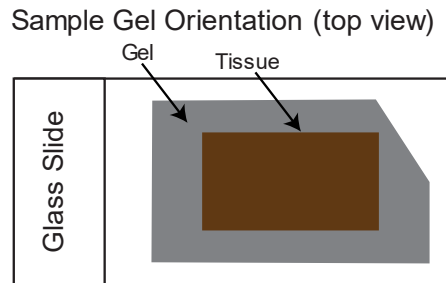
Step 3.2. Gel Trim and Orientation. Gelled tissue is trimmed after removing the gelation chamber. A cut in an off-angle fashion is made to help the user remember the orientation of the original tissue and distinguish the gel bottom from the gel surface.

3. This is particularly useful when using objectives with a short working distance, to ensure the gel surface is facing down towards the objective (**Step 3.3**).

Free Floating Sample Gel (side view)

Gel bottom   Gel surface   Imaging glass
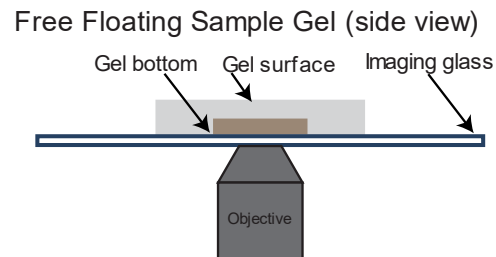
Objective

Step 3.3. Gel surface and bottom orientation. In short distance objectives, it is especially important to remember the gel surface and bottom to be able to adequately image tissue at super-resolution scales.

4. ***This step (4) can be skipped in many brain tissues, including normal brain and mouse tissues. This is particularly useful in tissue with significant amounts of vascular and extra cellular matrix components found in brain pathologies like certain types of vascular brain tumors. Submerge the tissue sample slide into a container ensuring the tissue is fully covered with Collagenase buffer and incubate for 3 hours at 37°C with gentle shaking. Then transfer the slide with gel to a new container containing Softening buffer.
5. Incubate the gelled tissue in Softening buffer at 37°C for 30 min with gentle shaking and then incubate for 1 hr in a steamed autoclave at 121°C (**Step 3.5**).
   *For FFPE tissues in glass slides, add the full tissue slide into a conical tube, as the gelled tissue will separate from the glass slide with the least disruption of the tissue and into the bottom of the tube following softening.
   **For PFA tissues on a non-charged slide and that have been removed from the slide, they can be added as free floating tissue.

Tissue on a slide
50 mL Conical Tube
Glass Slide

Free floating tissue
50 mL Conical Tube
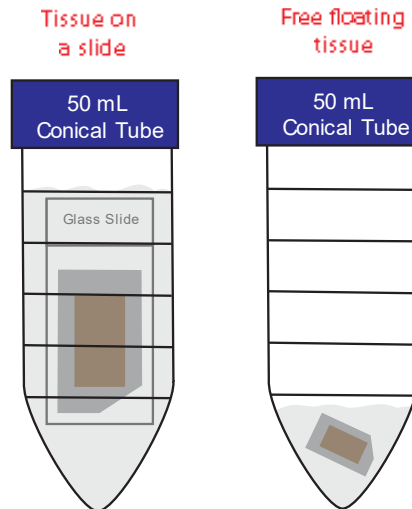
Step 3.5. Softening Buffer Incubation. Two examples of how to perform the softening step on tissues attached to a slide or on free floating tissues

    a. You can submerge the gel, still on the slide (or the free floating gel if it has been separated from slide) meanwhile ensuring tissue is fully covered with freshly made softening buffer (including BME).

    b. Small tissues can be added into an Eppendorf tube; full slides can be added into appropriate containers that ensure sealing like a 50 mL conical tube which would then have the tissue fall off the slide.

6. Normally the sample will detach from the glass slide by itself after softening with gentle shaking. If needed, use a razor blade or brush to gently move the sample off the slide. However,it has been our experience that FFPE tissues will fall off at the end of treatment or during the cool down period with gentle shaking.

    *For 50-100 μm thick PFA fixed mouse brain slices do 48 hours (overnight x2) at 37°C with gentle shaking in Softening buffer (including BME) and then, remove old buffer, add new buffer, and incubate for another 1 hr in a steamed autoclave cycle, cool down, and wash in 1x PBS five (5) times at least 45-60 min each wash, ensuring complete removal of softening buffer.

Step 4. Decrowding
1. After softening, the gelled tissue has detached from the slide and is floating freely in the Softening buffer.
2. Transfer the tissue into a clear polystyrene petri dish plate by slowly decanting the buffer solution which contains the gelled tissue into the plate.
3. Using a pipette, the excess buffer is removed and discarded.
4. Add 1x PBS to the well plate to fully cover the tissue and the petri dish plate is gently shaken at RT to remove excess softening buffer.
5. While the gelled tissue is free floating in 1x PBS use a flat, wide, miniature paintbrush and place underneath the gelled tissue (**Step 4.5**), ensuring that the paint brush is covering most of the gelled tissue undersurface area and transfer into a clear 6-well plate (Clearstar) that contains 1x PBS to completely submerge the tissue
6. Gently shake the well plate at RT for 3 min.

7. Excess 1x PBS is removed using a pipette and new 1x PBS is added to cover the tissue and the well plate and gently shake at RT for 3 min. This process is repeated a total of 5 times, which results in tissues reaching an expansion factor of ~2.3x.
8. While the gelled tissue is free floating in 1x PBS, use a flat, wide mini paintbrush (i.e., a brush with no prior contact with softening buffer) and place underneath the gelled tissue, ensuring that the paint brush is covering most of the gelled tissue undersurface area, and transfer into a new 6-well plate (CellVis) that will be subsequently used for imaging, and which contains 1x PBS.

      *Once the gelled tissue has been washed thoroughly in 1x PBS they can be stored in this state for days to weeks if the PBS does not evaporate, otherwise, a dry environment will dry out the gels and the tissue gel will be unusable.
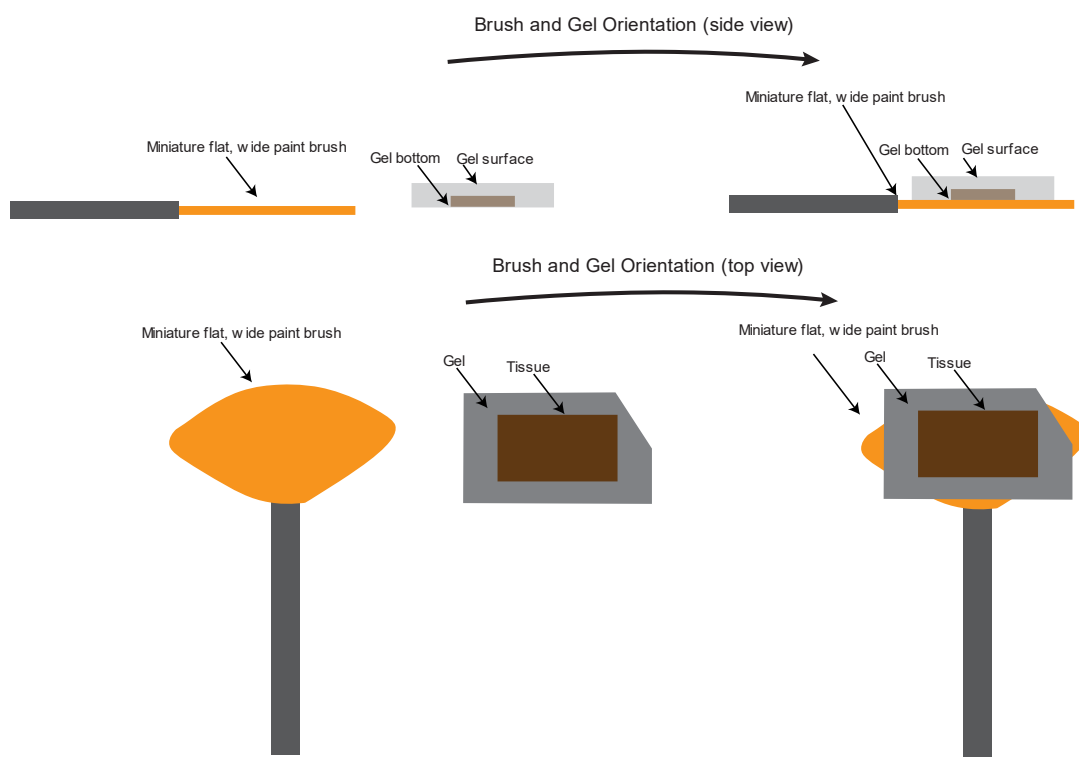
Step 4.5. Gel Transfer. Miniature flat, wide paintbrush (orange) placed underneath the gelled tissue while it is floating in solution. Transfer on and off the pain brush while tissue is in solution to ensure no damage to the gelled tissue.

Step 5. Immunostaining Post-Decrowding
*The following steps are like a typical staining protocol (immunofluorescence (IF)/immunohistochemistry (IHC)) but in this case "on a gelled tissue". The numbers below are for a typical 5x5 mm tissue gel (i.e., the width and length size after the decrowding step) and in which the staining is done on a 6-well plate (CellVis).
**Volumes can be modified if using smaller containers/samples, e.g., a tissue microarray core with an original diameter of 1 mm, after decrowding can be a 2.3x 2.3 mm square and can be used in a 12-well plate (CellVis) with glass bottom or transferred

into 0.5 mL Eppendorf tubes, and volumes can go down to 100-200 µL for working antibody solutions.

***The incubation times here are for FFPE tissues with an original thickness of 5-10 µm. For 50-100 µm thick tissues we recommend at least 24 hours incubation times with both primary and secondary antibody incubations at 4°C.

Primary Antibody Staining

1. Remove excess PBS from the well, add 500 µL of MAXblock™ Blocking Medium and incubate for 1 hour at 37°C.
2. Remove excess MAXblock™ Blocking Medium and wash three (3) times with 1 mL each time using MAXwash™ buffer for 3 min each at RT.
3. Prepare primary antibody solution by diluting primary antibody in MAXbind™ Staining buffer.
4. Perform post-decrowding immunostaining by incubating tissue samples in 500 µL of primary antibody solution at 37°C for 1 hour, at RT for 2.5 hours or at 4°C overnight.
5. Remove excess primary antibody solution and wash three (3) times with 1 mL each time using MAXwash™ buffer for 3 min each at RT.

Secondary Antibody Staining

6. Prepare secondary antibody solutions by diluting secondary antibody in MAXbind™ Staining buffer.
> *If using a nuclear stain (e.g., DAPI), staining can be done by incorporating the nuclear stain into the secondary antibody solution.
7. Incubate the tissue samples in 500 µL of secondary antibody solution using the same conditions applied for primary antibodies.
8. Remove excess secondary antibody solution and wash three (3) times with 1 mL each time using MAXwash™ buffer for 3 min each at RT.
9. At this stage tissues are ready for imaging at the 2.3x expanded state, ready for expansion to ~4x (see below), or for storage in excess 1x PBS.
> *Suggested incubation periods and temperatures are given as a guide only. It is recommended that the user optimize these parameters for use in their own experiment based on antibodies and tissue thickness. It has been our experience that with a large range of commercially available antibodies and in tissues of this thickness, incubation times of 1-2 hours seem sufficient to get adequate staining.
> **Sample needs to be covered with the well plate cover and sealed with Parafilm during the incubation periods to prevent drying out.
> ***Antibody concentrations are antibody specific and will require optimization based on the antibody used. It has been our experience that we start with the recommended concentrations by the vendor and then concentrate or dilute the solution as needed.

Tissue Expansion

10. Immunostained tissues are expanded by washing with deionized water at RT for 3-5 times for 3 min each at RT to achieve an approximate ~4x linear expansion.
> *For expansion, remove the PBS and wash the samples with excess volume of 1/100 1x PBS for 3-5 times, for 10 minutes each time at RT. You can also use deionized water, but in

post-expansion staining we have noticed a small decrease in fluorescence intensity of up to 10% when expanding in deionized water compared to a low salt solution like 1/100 PBS 1x. Gels will reach an expansion factor of ~4x.

**Slice expansion should reach a plateau after about the 3rd or 4th wash.

***Expansion chamber (i.e., well plate) needs to be of adequate size to fit the expanded sample.

***The sample might need to be trimmed prior to expansion using a razor blade into smaller pieces if no chamber of proper size can be obtained. In general, an expanded gel containing a tissue with diameter less than 0.6 cm pre-expansion fits adequately in a glass bottom 6-well plate.

****Please note that fully expanded gels are friable and can easily break if the user tries to lift them up. To transfer gels between containers do so in the ~2.3x state.

Step 6. Imaging

1. Remove any excess solution to ensure that the tissue sample is dry around all the edges using a micropipette to gently suction out any excess liquid as well as Kim wipes without touching and damaging the gelled tissue.

> *Tissue samples can be imaged at super-resolution scales using conventional systems such as a wide field or confocal fluorescence microscope.

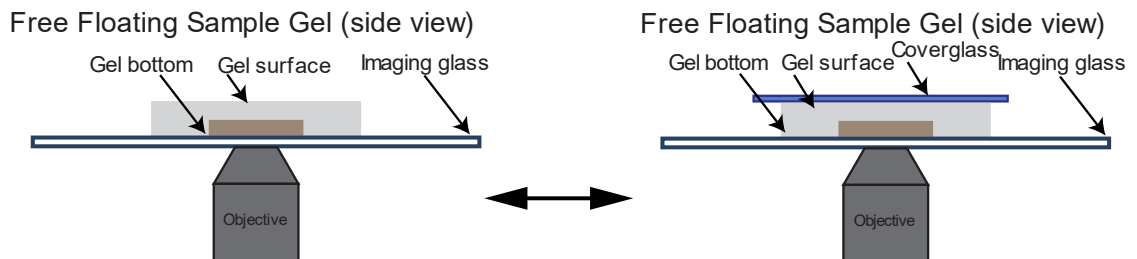2. Make sure the gel bottom is facing down towards the objective (**Step 6.3**).

> *See step 4.2 for details regarding gel orientation.

> **Experienced users can determine which side is the gel surface or gel bottom by the microscope z-settings when focusing on their tissues.

3. Once confirmed that the gel bottom is facing down, the tissue sample can be imaged.

> *We found we can minimize micromovements to obtain high quality images at 10x or 40x magnification by placing a cut piece of cover glass of slightly larger surface area (i.e., larger than the gel) on top of the gel (**Figure 7**).

> *When imaging is completed, the gel can be submerged in excess 1x PBS and the cover glass will separate from the gel without damaging it.

Step 6.3. Imaging of dExPath Gelled Tissues. Imaging with an inverted wide field or confocal fluorescence microscope, with the gel bottom facing down towards the microscope objective, which is especially important when working with short working distance objectives. To ensure no movement of tissue after drying, place a cut cover glass on top of the gelled tissue

Step 7. Antibody Stripping

1. Once tissue samples have been imaged, transfer the sample into a closed container (e.g., 6-well plate, conical tube) and add Softening buffer (with BME) to fully immerse the sample (e.g., 1x1 cm gel, cover with 3-5 ml buffer)

2. Incubate samples for two (2) hours at 70°C with gentle shaking (ensuring samples do not dry out).

3. Once the stripping incubation is finished, samples shrink to a size of approximate ~1.3x expansion factor.
4. Wash samples for five (5) times with 1x PBS for at least five (5) min each time.
    *Times will be longer with thicker tissues.
5. Transfer sample into a 6-well plate and repeat **Step 5. Immunostaining Post-Decrowding** for another round of antibodies and **Step 6. Imaging** for imaging with the new round of antibodies.
    *You can repeat "stripping and staining" as many rounds as needed to test markers of interest.
    **Of note, we recommend keeping one channel constant or as a reference for all rounds. This constant or reference channel can be used for registration between rounds. For example, for FFPE human samples we found that using DAPI or staining with a goat anti-H3 histone antibody as the constant channel yielded excellent results. For example, if you have mouse, rabbit and chicken antibodies, you can do 3x3=9 different targets + 1 for DAPI or nuclear H3 histone, to achieve multiplexed imaging. However, you can choose your constant channel as your experiment dictates, just remembering that you will need a channel with enough similar features to ensure adequate registration between immunostaining rounds.
    ***After each round of stripping and staining, the gels shrink, and prior to imaging they require expanding back to ~4x expansion factor.

Expansion Factor Considerations
If the user wishes to calculate the expansion factor to relate the post-expansion physical units' size to the pre-expansion biological unit's size, they can consider the following two methods:

Pre-expansion DAPI staining
1. Following **Step 1** and prior to **Step 2,** stain the pre-expansion (native) tissues with 2 µg/mL of DAPI in 1x PBS for 30 min at RT.
2. Cover the tissue section with aqueous mounting media and take a pre-expansion image.
3. The expansion factor and thus, the biological units of length can be established later by measuring identical features from the pre-expansion tissue with the post-expansion tissue to calculate the expansion factor.
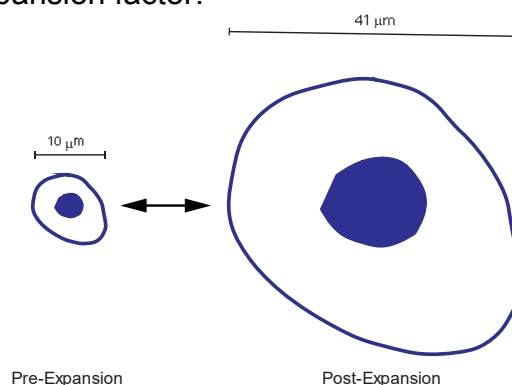
Pre- and Post-Expansion DAPI Staining for Expansion Factor Calculation

Pre-expansion Gel Measurement
1. Obtain pre-expansion measurements using a measurement tool (e.g., a ruler) to measure the gel prior to placing in the softening buffer.
2. Obtain post-expansion measurements using the same measurement tool but this time measure the expanded gel to calculate the expansion factor.

Step 1 Extra. PRE-EXPANSION STAINING
Antigen retrieval
1. After drying at the end of **Step 1**, place the slide in a humidified container and add Softening buffer to ensure the tissue is completely covered by buffer.
2. Incubate for 1 hour at room temperature in Softening buffer inside a humidified container.
      *Here we incubated in Softening buffer for antigen retrieval to then perform pre-expansion staining and thus mimic the chemical conditions that the tissue undergoes following decrowding in the gel format. However, the user can use other methods of antigen retrieval if they so wish (e.g., citric acid with microwave incubation).
3. Remove excess Softening buffer from the slide and wash five (5) times with 1x PBS for 3 min each time.

Pre-expansion antibody staining

Here we proceed with primary and secondary antibody staining using the same conditions, antibodies, concentrations and buffers as in **Step 5**.

Primary Antibody Staining
4. Using a hydrophobic pen, create a layer surrounding the tissue (**Step 1.4 Extra**).
5. In a humidified chamber add 200-500 µL of MAXblock™ Blocking Medium to make sure the tissue is completely covered with Blocking Medium and ensuring Blocking Medium is not overflowing over the hydrophobic layer and incubate for 1 hour at 37°C.
6. Remove excess MAXblock™ Blocking Medium and wash three (3) times with 1 mL each time using MAXwash™ buffer for 3 min each at RT.
7. Prepare primary antibody solution by diluting primary antibody in MAXbind™ Staining buffer.
8. Perform pre-expansion (i.e., pre-decrowding) immunostaining by adding 100-300 µL of primary antibody solution to make sure the tissue is completely covered with antibody staining solution and ensuring antibody staining solution is not overflowing over the hydrophobic layer and incubate tissue samples at 37°C for 1 hour, at RT for 2.5 hours or at 4°C overnight.
9. Remove excess primary antibody solution and wash three (3) times with 1 mL each time using MAXwash™ buffer for 3 min each at RT.

Step 1.4 Extra. Pre-expansion staining hydrophobic layer preparation

Secondary Antibody Staining

10. Prepare secondary antibody solutions by diluting secondary antibody in MAXbind™ Staining buffer.

> *If using a nuclear stain (e.g., DAPI), staining can be done by incorporating nuclear stain into the secondary antibody solution.

11. Incubate the tissue samples in 100-300 µL of secondary antibody solution using the same conditions applied for primary antibodies.

12. Remove excess secondary antibody solution and wash three (3) times with 1 mL each time using MAXwash™ buffer for 3 min each at RT and then transfer into a new container with 1x PBS.

13. Gently air-dry the slide and using Kim wipe, remove excess PBS for less than 1 min

14. Use a blade to scrape off the hydrophobic layer thoroughly.

15. Then add VectaShield (aqueous) mounting medium (2-3 drops) on the tissue and cover tissue with a #1 cover slip making sure there are no air bubbles trapped.

16. Add a drop of nail polish at each end so it covers both the end of the coverslip and a portion of the slide to help keep the coverslip without moving while imaging.

17. At this stage tissues are ready for imaging at the pre-expanded state or storage at 4°C in low light conditions to minimize quenching and drying out of tissues.

> *Suggested incubation periods and temperatures are given as a guide only. It is recommended that the user optimize these parameters for use in their own experiment based on antibodies and tissue thickness. It has been our experience that with a large range of antibodies in tissues of this thickness, incubation times of 1-2 hours seem sufficient to get adequate staining.
>
> **Antibody concentrations are antibody specific and will require optimization based on the antibody. It has been our experience that we start with the recommended concentrations by the vendor and then concentrate the solution as needed.

18. Once imaging has been completed, the user can submerge the tissue slide into a container with 1x PBS for 10 min at RT with gentle shaking.

19. Using a blade, gently remove the cover slip while in the PBS solution and once removed, wash slide in 1x PBS three (3) times for 3 min each.

120. Now tissues are ready to proceed with **Step 2** above.